

Electronic Thesis and Dissertation Repository

8-7-2013 12:00 AM

Imaging Breast Cancer Progression and Lymph Node Metastases in Murine Models Using MRI and Magnetic Nanoparticles

Vasiliki Economopoulos, *The University of Western Ontario*

Supervisor: Dr. Paula Foster, *The University of Western Ontario*

A thesis submitted in partial fulfillment of the requirements for the Doctor of Philosophy degree in Medical Biophysics

© Vasiliki Economopoulos 2013

Follow this and additional works at: <https://ir.lib.uwo.ca/etd>



Part of the [Biophysics Commons](#), and the [Neoplasms Commons](#)

Recommended Citation

Economopoulos, Vasiliki, "Imaging Breast Cancer Progression and Lymph Node Metastases in Murine Models Using MRI and Magnetic Nanoparticles" (2013). *Electronic Thesis and Dissertation Repository*. 1440.

<https://ir.lib.uwo.ca/etd/1440>

This Dissertation/Thesis is brought to you for free and open access by Scholarship@Western. It has been accepted for inclusion in Electronic Thesis and Dissertation Repository by an authorized administrator of Scholarship@Western. For more information, please contact wlsadmin@uwo.ca.

IMAGING BREAST CANCER PROGRESSION AND LYMPH NODE METASTASES
IN MURINE MODELS USING MRI AND MAGNETIC NANOPARTICLES

(Thesis format: Integrated Article)

by

Vasiliki Anastasia Economopoulos

Graduate Program in Medical Biophysics (Molecular Imaging)

A thesis submitted in partial fulfillment
of the requirements for the degree of
Doctor of Philosophy

The School of Graduate and Postdoctoral Studies
The University of Western Ontario
London, Ontario, Canada

© Vasiliki Economopoulos 2013

Abstract

Most breast cancer related deaths are caused by the spread or metastasis of the primary tumor to distant sites in the body. The lymph nodes are one of the first places where metastases can be detected and are frequently examined for macroscopic metastases to help determine course of treatment for patients. However, little is known about the significance of microscopic metastases and disseminated individual cancer cells within the nodes. The goal of this work was to use MRI to monitor the development of primary tumors and lymphatic metastases in models of breast cancer.

In this thesis, we examined the MRI appearance of lymph nodes in several different strains of immune compromised mice (nude, CB -17 SCID, NOD/SCID IL2Rnull) and compared the appearance to immune competent C57/Bl6 strain. We found that immune deficiencies influenced the MRI appearance of nodes and that the nude strain had highly variable lymph node appearance and volume. We also compared orthotopic transplantation models of breast cancer that used both the nude and CB-17 SCID strains using MRI. We found that MRI was most reliable for detecting metastases in the lymph nodes of SCID mice and that the variability of the appearance of nodes in nude mice can lead to their misclassification. We then used the SCID orthotopic breast cancer model to monitor the appearance and retention of iron oxide nanoparticle labeled cancer cells in both the primary tumor and lymph nodes. We found that iron-labeled cells are still detected within the primary tumor after 28 days post-implantation and that these labeled cells almost exclusively migrated to the lymph nodes.

The development of improved methods for monitoring the development of the primary tumor and metastases and the roles that different cells populations have in these processes will allow for more accurate knowledge of how cancer cell heterogeneity impacts disease progression. These tools will allow for more effective monitoring of the treatment effect of new drugs on primary tumors and metastatic dissemination.

Keywords

magnetic resonance imaging, breast cancer, metastasis, tumor heterogeneity, MPIO, iron oxide, bSSFP, mice, dormancy, lymph nodes, cancer cells

Co-Authorship Statement

Material presented in Chapter 2 is from a previously published manuscript. The authors are: V Economopoulos, JC Noad, S Krishnamoorthy, BK Rutt and PJ Foster. In this work, PJF contributed to study design and manuscript preparation, VE performed the majority of data collection, all data analysis and contributed to experiment design and manuscript preparation, JCN and SK assisted with data collection and BKR developed the gradient insert coil and pulse sequence.

In Chapter 3, Y Chen performed animal surgeries and assisted with histologic sample preparation. V Economopoulos cultured cells, performed data collection, sample retrieval and contributed to experiment design and manuscript preparation. PJF contributed to experimental design and manuscript preparation.

Work described in Chapter 4 was previously published. The authors are: V Economopoulos, Y Chen, C McFadden and PJ Foster. V Economopoulos contributed to experiment design, data collection, cell culture, data analysis and manuscript preparation. YC performed animal surgeries and also assisted with histological sample preparation. CM assisted with cell culture. PJF contributed to experimental design and manuscript preparation.

For all work performed, BK Rutt had developed the gradient insert coil and pulse sequence and Francisco M Martinez-Santiestban maintained the hardware and software and Andrew Alejski maintained the hardware. Figures in Chapter 1 were partially prepared by Chelsey Gareau.

Acknowledgments

I would like to thank Jon Snir, Roja Rohani and Beth Dunn for teaching me dissection and laboratory techniques and training me to use the MRI system. I would also like to thank Drs. Amanda Hamilton and Emeline Ribot for helpful conversions and technical assistance. I wish to thank Drs. Francisco Martinez-Santiestban and Andrew Alejski for assistance with the hardware and software for the MRI system.

I want to thank my supervisor, Dr. Paula Foster, for all her support during the last 5 years and helping to guide me along the way during my degree. I also wish to thank my advisor committee, Drs. Alison Allan and Elizabeth Gillies for their guidance and support. I wish to thank my fellow lab-mates over the years who have been there to provide their support.

I also want to thank my family for supporting through this process and have helped me every step of the way. I greatly appreciate all the support and guidance I received from everyone in helping me to achieve my goal.

Table of Contents

Abstract.....	ii
Co-Authorship Statement.....	iv
Acknowledgments.....	v
Table of Contents.....	vi
List of Tables.....	x
List of Figures.....	xii
List of Appendices.....	xviii
List of Abbreviations.....	xix
Chapter 1.....	1
1 General Introduction.....	1
1.1 Cancer.....	1
1.1.1 Breast Cancer.....	2
1.1.2 Metastatic Process.....	4
1.1.3 Tumor Microenvironment and Heterogeneity.....	7
1.1.4 Dormancy.....	9
1.2 Cellular MRI.....	13
1.2.1 Nuclear Magnetic Resonance (NMR).....	13
1.2.2 T1 and T2 Relaxation.....	15
1.2.3 Pulse Sequences.....	18
1.2.4 Principles of Cellular MRI.....	23
1.2.5 Preclinical Applications of Cellular MRI.....	25
1.2.6 Clinical Applications of Cellular MRI.....	27
1.3 Goal and Objectives.....	29
1.4 References.....	30

Chapter 2.....	43
2 Comparison of Lymph Nodes and Spleen in Immune Compromised and Wild-Type Mice	43
2.1 Introduction.....	43
2.2 Materials and Methods.....	45
2.2.1 Mice	45
2.2.2 Magnetic Resonance Imaging.....	46
2.2.3 Image Analysis.....	46
2.2.4 Histopathological Analysis	47
2.3 Results.....	47
2.3.1 Lymph Node Appearance and Volumes	47
2.3.2 Spleen Appearance and Volumes	54
2.3.3 Changes in Lymph Node Volumes Over Time.....	55
2.4 Discussion.....	58
2.5 References.....	62
Chapter 3.....	65
3 Comparing Tumor Growth and Metastasis in Xenograft Models of Breast Cancer using MRI	65
3.1 Introduction.....	65
3.2 Materials and methods	67
3.2.1 Animal Models.....	67
3.2.2 MRI imaging in mice	67
3.2.3 Histology.....	68
3.2.4 Image Analysis.....	68
3.2.5 Statistical Analysis.....	68
3.3 Results.....	69
3.3.1 Differences in Tumor Growth.....	69

3.3.2	Differences in Metastases	74
3.4	Discussion	84
3.5	References	87
Chapter 4	89
4	MRI Detection of Nonproliferative Tumor Cells in Lymph Node Metastases Using Iron Oxide Particles in a Mouse Model of Breast Cancer	89
4.1	Introduction	89
4.2	Methods	90
4.2.1	Cell Culture and In Vitro Experiments	90
4.2.2	Animal Model	91
4.2.3	MRI Methods	92
4.2.4	Microscopy Methods	92
4.2.5	Image Analysis	93
4.3	Results	94
4.3.1	In Vitro Iron Dilution	94
4.3.2	MRI of Primary Tumor	97
4.3.3	Histology of Primary Tumor	100
4.3.4	Detection of Regions of Signal Loss in Lymph Nodes	101
4.4	Discussion	108
4.5	References	111
Chapter 5	114
5	Conclusions and Future Work	114
5.1	Conclusions	114
5.1.1	Chapter 2	114
5.1.2	Chapter 3	115
5.1.3	Chapter 4	116

5.2 Future Work	117
5.2.1 Optimizing the Detection of MPIO Retaining Tumor Cells in MRI	117
5.2.2 Demonstrating Metastasis formation from Disseminated MPIO Labeled Cells	118
5.2.3 Correlating MPIO Retention With Standard Label Retention Techniques and Determining Phenotype of MPIO Retaining Tumor Cells.....	119
5.2.4 Effect of Treatment and Modified Gene Expression on MPIO Retaining Cells	120
5.2.5 Examine Effect of Strain on Metastases to Other Organs and In Different Tumor Types.....	121
5.3 References.....	122
Appendices.....	124
Curriculum Vitae	129

List of Tables

Table 1.1 – Histological breast tumor type and frequency ^{7,8}	2
Table 1.2 - Expression of prognostic markers in different breast cancer subtypes. ¹¹	3
Table 1.3 - Approximate values of relaxation times at 1.5 T ⁷⁷	16
Table 1.4 - Pulse sequence timing parameters and associated image contrasts.....	19
Table 1.5 - TE and flip angle for achieving different contrasts with basic GE sequences ^{75,79}	21
Table 2.1 - Lymph node volumes of C57Bl/6, Nude and CB-17 SCID mice. All volumes listed as mean ± standard deviation.	51
Table 3.1 – Number of animals in each group that formed tumors	69
Table 3.2– Number of Animals injected with MDA-MB-231 cells with Single or Multiple Lesions	80
Table 3.3– Correspondence of lymph node volume and presence of metastases. Nodes were considered ‘enlarged’ if their volume was more than 2 standard deviations away from the volume of the corresponding control lymph node.	81
Table 4.1 – Tumor volume and percent of tumor volume in tumor color map zones. Blue zone is below low intensity cutoff (signal intensity of 255), green zone is between low intensity cutoff and high intensity cutoff (signal intensity of 700), and yellow zone is above high intensity cutoff.	99
Table 4.2 – Analysis of axillary lymph nodes examined with both MRI and either PPB staining or fluorescence microscopy (PPB = Perl’s Prussian Blue, FL = Fluorescence Microscopy)	105

Table 4.3 – Analysis of brachial lymph nodes examined with both MRI and either PPB staining or fluorescence microscopy (PPB = Perl’s Prussian Blue, FL = Fluorescence Microscopy) 107

List of Figures

Figure 1.1 - Steps in the metastatic process. (1) Cells detach from primary tumor. (2) Cells intravasate into vessel. (3) Cells arrest at a distant site. (4) Cells extravasate from vessel at distant site. (5) Cells proliferate, forming a clinically detectable secondary tumor.	4
Figure 1.2 - Schematic of lymph node depicting the location of immune cells and various structures. Adapted from reference 22.....	6
Figure 1.3 – The tumor microenvironment. There are many different types of cells within a tumor, all of which support the growth and survival of cancer cells through cellular interactions. Adapted from reference 26.....	8
Figure 1.4 – Dormancy and inefficiency of metastatic process. Only a small percentage of the tumor cells that arrest at a second site will go on to form micrometastases and macrometastases. The majority of cells will undergo apoptosis or will remain in a dormant state. Less than 2 % of arrested cells will form micrometastases and less than 0.02% of those micrometastases will develop into macrometastases. The question marks in the figure represent quantities that are unknown. The number of cells that will enter a dormant state after arrest is not known as well as the percentage of dormant cells or micrometastases that develop into macrometastases. Adapted from reference 15.	10
Figure 1.5 - Relaxation curves for transverse (MXY, black) and longitudinal (MZ, blue) magnetization. Adapted from reference 76.....	17
Figure 1.6 - Single spin echo sequence timing diagram. Adapted from reference 75.....	19
Figure 1.7 - Timing diagram for basic gradient echo sequence. Adapted from reference 75.	20
Figure 1.8 - Pulse sequence diagram of bSSFP pulse sequence. The net gradient area for each applied gradient is zero. Adapted from reference 80.....	22
Figure 2.1 - (A) Whole mouse body bSSFP image of a C57Bl/6 mouse showing both the brachial and inguinal lymph nodes (arrows) and (B) 3D reconstruction showing the location	

of various lymph nodes within the mouse; 1 – axillary node, 2 – brachial node, 3 – inguinal node, 4 – popliteal node. 48

Figure 2.2 - MR appearance and volumes of lymph nodes various mouse strains. (A) MR appearance of the axillary, brachial, inguinal and popliteal lymph nodes in C57Bl/6, Nude, CB-17 SCID and NOG mice. The brachial, inguinal and popliteal lymph nodes are easiest to visualize due to their location within a fat pad. Lymphatic vessels are also visible in acquired images (arrowhead). Images for the NOG mice are included for completeness although there were no MRI detectable lymph nodes. (B) Volumes of the axillary, brachial, inguinal and popliteal lymph nodes in C57Bl/6, Nude and CB-17 SCID mice. The brachial, inguinal and popliteal lymph nodes in CB-17 SCID mice were found to be significantly smaller than those in both C57Bl/6 and Nude mice (*, $p < 0.0001$ for brachial and inguinal and $p = 0.0128$ for popliteal). The axillary node in Nude mice was significantly larger than those in both CB-17 SCID and C57Bl/6 mice (**, $p < 0.0001$). One way ANOVA test was used. Error bars represent the standard deviation. 49

Figure 2.3 - H&E sections of brachial lymph nodes from C57B/l6, Nude and C.B.-17 SCID mice. Whole nodes are shown at 5x magnification. The T cell rich paracortex (arrowheads) and B cell rich follicles (arrows) can be easily seen in the nodes of C57B/l6 mice, where as in Nude mouse lymph nodes, only the B cell rich follicles can be seen (arrows). In the areas of the paracortex where T cells should be found, vacant areas are detected (arrowheads), helping to explain the hyperintense appearance of many of these nodes in MR images. Nodes in SCID mice lack both the paracortex and follicles, leaving these nodes underdeveloped and significantly smaller in size. 52

Figure 2.4 - MR image of a nude mouse axillary node with hyperintense center (A) with corresponding histology (B). The hyperintense area within the lymph node (arrow) corresponds to a cavity that is visible in the histology. 53

Figure 2.5 - MR images of a nude mouse brachial lymph node acquired with different pulse sequences. (A) bSSFP image of whole mouse body, (B) bSSFP image of lymph node, (C) T1w SE of lymph node (TR = 600 ms, TE = 25 ms), (D) T2w SE of lymph node (TR = 2000 ms, TE = 80 ms). 54

Figure 2.6 - bSSFP images of the spleen in (A) C57Bl/6, (B) nude, (C) CB-17 SCID and (D) NOG. (E) Spleen volume in C57Bl/6, Nude, CB-17 SCID and NOG mice. (*) Spleen volumes were significantly smaller in CB-17 SCID and NOG mice ($p < 0.0001$) compared to C57Bl/6 and nude mice. One way ANOVA test was used. Error bars represent the standard deviation..... 55

Figure 2.7 - Lymph node volumes over time. (A) C57Bl/6 mice. (B) Nude mice. (C) CB-17 SCID mice. Significant differences were found in the inguinal ($p = 0.0071$) nodes of C57Bl/6 mice. Significant differences were also found in the axillary ($p = 0.0104$), inguinal ($p = 0.0155$) and popliteal ($p = 0.0046$) nodes of nude mice. Significant differences were also found in SCID mice in the brachial ($p = 0.0130$) and inguinal nodes ($p = 0.0225$). (*) Significantly different compared to day 7. Repeated measures ANOVA test was used. Error bars represent the standard deviation..... 57

Figure 3.2 - Image of tumor bearing mouse. (A) Whole mouse body. T - tumor, H - heart, L - lungs, G - gut. (B) Image of axillary lymph node (outlined in yellow). (C) Image of brachial lymph node (outlined in yellow)..... 70

Figure 3.2 – Appearance of tumors at both scan time points. Tumors generated from MDA-MB-231 cells (A - nude and C - SCID) are much larger and have regions of heterogeneous signal intensity (arrowheads). Tumors generated from MDA-MB-435 cells (B - nude and D - SCID) are much smaller and have a more homogeneous appearance (arrows). The MRI appearance of tumors for each cell line was similar regardless of the strain..... 71

Figure 3.3 - H&E stained sections of tumors. (A, B) Tumor from nude mouse injected with 231 cells. (C, D) Tumor from nude mouse injected with 435 cells. (E, F) Tumor from SCID mouse injected with 231 cells. (G, H) Tumor from SCID mouse injected with 435 cells. Images A, C, E, and G were taken at 10x magnification. Images B, D, F and H were taken at 40x magnification. The box in images A, C, E and G highlights the area that is shown in the adjacent image in the second column. 72

Figure 3.4 – Tumor volumes over time. For animals injected with MDA-MB-231 cells (231 cells), Scan 1 was at 21 days and Scan 2 was at 28 days. For animals injected with MDA-

MB-435 cells (435 cells), Scan 1 was at 30 days and Scan 2 was at 37 days. ** Significant compared to nude mice. * Significant compared to the 231 cell line. 74

Figure 3.5 – MR appearance of nude mouse lymph nodes. Lymph nodes (outlined in yellow in all images) in mice injected with MDA-MB-231 cells (row 2) were enlarged and had a heterogeneous appearance. Lymph nodes from animals injected with MDA-MB-435 cells (row 3) have a similar appearance to control animals (row 1). 76

Figure 3.6 – MR appearance of SCID mouse lymph nodes. Lymph nodes (outlined in yellow in all images) in mice injected with MDA-MB-231 cells (row 2) were enlarged and had a heterogeneous appearance. Lymph nodes from animals injected with MDA-MB-435 cells (row 3) have a similar appearance to control animals (row 1). 77

Figure 3.7 – Lymph node volumes. (A) Scan 1, (B) Scan 2. The lymph nodes of animals injected with 231 cells were found to be significantly larger than those in control animals and animals injected with 435 cells. * - Significant compared to 435 cells. + - Significant compared to Controls. ‡ - Significant compared to both 435 cells and controls. 79

Figure 3.8 – Hematoxylin and Eosin stained lymph node sections. (A, B) Nude with 231 cells, (C, D) Nude with 435 cells, (E, F) SCID with 231 cells, and (G, H) SCID with 435 cells. Sections (A, C, E, G) are taken at x10 and sections (B, D, F, H) are taken at x40 with black boxes outlining the zoomed sections in the x10 images. In the animals injected with 231 cells, metastases can be found underneath the lymph node capsule in both Nude mice (A, arrowhead) and SCID mice (E, arrowheads), These metastases are shown at a greater magnification in B and F respectively (B and F, arrowheads). Evidence that metastatic lymph nodes are reactive is also seen in A (arrow). No metastases were present in the lymph nodes of animals that received 435 cells, but evidence of reactivity was seen (arrows in C, D, G and F). In the SCID mice specifically, areas with macrophage hyperplasia were frequently found (G and H, arrows) whereas nude mice had regions of plasma cell hyperplasia. 82

Figure 4.1 – Stained cell samples of MPIO labeled MDA-MB-231 cells at 1, 4, 7, 10, and 14 days after labeling. Graph of percentage of iron labeled MDA-MB-231 cells over time. 94

Figure 4.2 – *In vitro* dilution of MPIO particles in MDA-MB-231 cells measured by flow cytometry. (A) Graph of percentage of iron labeled MDA-MB-231 cells over time. (B) Plots

of Flash Red fluorescence intensity (x-axis) vs. side scatter (y-axis) at day 1, 2, 4, 7, 10 and 14 with gates shown for the labeled population (based on unlabeled control sample)..... 96

Figure 4.3 – Appearance of labeled and unlabeled tumors over time and corresponding tumor color maps. (A) The MR image and color map, respectively, of a labeled tumor over time. (B) The MR image and color map, respectively, of an unlabeled tumor. For color maps, Blue – below low intensity cutoff (day 7 – 255, day 14 – 288, day 21 – 301, day 28 – 320), Green – between low intensity cutoff and high intensity cutoff (signal intensities of 700), Yellow – above high intensity cutoff..... 97

Figure 4.4 – PPB stained section of labeled tumor at day 14. (A) PPB stained section of tumor lobe. (B) PPB stained section showing the iron content from 6 consecutive sections (blue areas). (C) MR image of tumor. (D) PPB stained section of tumor from area outlined by box in (A). (E) PPB stained section showing the iron content from 6 consecutive sections (blue areas), from area outlined by box in (B). (F) PPB stained section of tumor from area outlined by box in (D)..... 101

Figure 4.5 – MRI and iron staining of an ipsilateral axillary lymph node 14 days after iron-labeled breast cancer cells were implanted into the thoracic mammary fat pad in CB17 SCID mice. (A) Cropped bSSFP image of thorax region of mouse reveals a region of signal loss in the ipsilateral axillary node (arrow). (B) Section of lymph node stained with Perl’s Prussian Blue for iron detection at x10 magnification shows iron positive cells in the area of the node corresponding to the signal loss in the MR image (arrow). (C) Iron positive area of the node at x40 magnification, where strong staining can be seen (arrow) suggesting that cancer cells have retained iron particles after migrating to the node. 102

Figure 4.6 – MRI and Fluorescence microscopy of a representative SCID mouse ipsilateral axillary lymph node 28 days after tumor cell implantation. CB17 SCID mice were injected with GFP positive MDA-MB-231 cells labeled with red fluorescent iron oxide particles. (A) Cropped bSSFP MRI image of the ipsilateral axillary lymph node shows a region of signal loss within the node (arrowhead). (B) GFP positive cancer cells found within node correspond with (C) red fluorescent MPIO particles. (D) Overlay of GFP fluorescent cells, red fluorescent MPIO and DAPI stain for cell nuclei. Cells that are positive for both GFP and

contain red fluorescent particles can be found within the node, confirming the presence of iron labeled cancer cells..... 103

Figure 4.7 – Confocal microscopy image of MPIO labeled MDA-MB-231 cells in an ipsilateral axillary lymph node 28 days after tumor cell implantation. (A) Image at 60x magnification. Area in white box has been enlarged (B) to show the localization of MPIO particles (red) in the cells (green). 104

List of Appendices

Appendix A: Permission To Reproduce Published Material	124
Appendix B: Animal Use Protocol Approval Letter.....	125
Appendix C: Volumes of Individual Lymph Nodes Over Time From C57Bl/6, Nude and SCID mice	126

List of Abbreviations

γ – Gyromagnetic ratio

ρ – Proton density

ω_0 – Larmor frequency

ALS – Amyotrophic Lateral Sclerosis

ANOVA – Analysis of variance

B_0 – Main magnetic field of MRI imaging system

BrdU – 5-Bromo-2'-deoxyuridine

bSSFP – balanced Steady State Free Precession pulse sequence

CCL – CC chemokine ligand

CFSE – Carbofluorescein succinimidyl ester

CNR – Contrast to Noise Ratio

CSC – Cancer stem cell or tumor initiating cell

CXCL – CXC chemokine ligand

CXCR – CXC chemokine receptor

Cy5.5 – Cyanine fluorescent dye

DAPI – 4',6-diamidino-2-phenylindole

EdU – 5-Ethynyl-2'-deoxyuridine

ER – Estrogen receptor

ESA – Epithelial specific antigen

FL – Fluorescence microscopy

fMRI – Functional magnetic resonance imaging

FOV – Field of view

FSL – Fractional Signal Loss

GE – Gradient echo pulse sequence

GFP – Green fluorescent protein

\hbar – Planck’s constant divided by 2π

H&E – Hematoxylin and eosin stain

HBSS – Hank’s Balance Salt Solution

HER2 – Human epidermal growth factor receptor 2

IL2R γ – Interleukin 2 receptor gamma chain

k – Boltzmann’s constant

M_0 – Net magnetization produced by all protons within a volume

M_{XY} – Transverse magnetization produced by all protons within a volume

M_Z – Longitudinal magnetization produced by all protons within a volume

MHC – Major histocompatibility complex

MPIO – Micron sized iron oxide particle

MRI – Magnetic Resonance Imaging

MS – Multiple Sclerosis

NEX – Number of signal averages

NMR – Nuclear magnetic resonance

NOD – Non-obese diabetic

NOG – NOD/SCID IL2R γ null

OCT – Optimal cutting temperature

PET – Positron Emission Tomography

PPB – Perls' Prussian Blue stain

PR – Progesterone receptor

R1 – Longitudinal relaxivity (affects T1 times)

R2 – Transverse relaxivity (affects T2 times)

RF – Radiofrequency

ROI – Region of interest

SCID – Severe combined immune deficiency

SE – Spin echo pulse sequence

SPF – Specific pathogen free

SPGR – Spoiled Gradient Echo Pulse Sequence

SPIO – Superparamagnetic iron oxide particle

SNR – Signal to Noise Ratio

T – Absolute temperature

T1 – Longitudinal relaxation time constant

T1w – T1 weighted

T2 – Transverse relaxation time constant

T2w – T2 weighted

TE – Echo time

TR – Repetition time

USPIO – Ultra small superparamagnetic iron oxide particle

VEGF – Vascular endothelial growth factor

Chapter 1

1 General Introduction

Cancer is one of the most devastating conditions that a patient can be faced with. Even though tremendous progress in the understanding and treatment of cancer has been made throughout the last few decades, many patients will still suffer severe morbidity and mortality, mostly due to late stage metastatic disease. By improving our understanding of the processes and cell phenotypes involved in metastasis, the prognosis for patients diagnosed with cancer could be dramatically improved. Cellular MRI is a technique that can be used to detect and monitor cells in vivo and may allow the metastatic process and the characteristics of the tumor cells that are involved to be studied in greater detail. This introductory chapter will discuss the concepts of breast cancer, metastasis, tumor heterogeneity and cellular dormancy as well as the techniques used in cellular MRI and how this technology is currently used in research.

1.1 Cancer

Approximately 186,400 people were diagnosed with all types of cancer in Canada in the year 2012 with an estimated 75,700 patient deaths attributable to the disease.¹ Cancer is defined as uncontrolled growth of abnormal cells resulting in life-threatening disease.² Clinically, cancer is considered to be collection of disorders involving unregulated cell growth, combined with invasion into surrounding tissues and spread to other organs.² This clinical definition of cancer, however, does not consider all aspects of tumorigenesis and the cellular processes that become deregulated. The definition includes many generalizations and does not account for differences between tumor types and how these differences impact treatment and outcomes.² In reality, there is great diversity between cancers in different patients, even if these diseases are of the same tumor type.² Cancer is an extremely complex set of diseases that requires the deregulation of normal homeostasis pathways and the acquisition of characteristics – such as resisting cell death, inducing angiogenesis, sustained proliferative signaling, replicative immortality, invasion and metastasis and evading growth suppression – that provide a survival advantage.^{3,4} Hanahan and Weinberg describe these characteristics, or

hallmarks of cancer, and the implications they may have for new therapy development.⁴ They also describe emerging hallmarks that have been identified more recently and are now recognized as necessary for tumor growth and progression.⁴ These emerging hallmarks include: tumor promoting inflammation, deregulated cellular metabolism, genomic instability and evading immune destruction.⁴ More recent studies have also identified the tumor microenvironment as playing a major role in the development and progression of many tumors by supporting the changes that occur to produce these hallmarks and will be further discussed in section 1.1.3.^{5,6}

1.1.1 Breast Cancer

In 2012, breast cancer was estimated to be the most common cancer diagnosed among women in Canada and had the second highest mortality rate, only behind lung cancer.¹ Breast cancer consists of many different diseases. These cancers typically arise in the lobules or ducts of breast tissue and the histological designation indicates the location and structure of the resulting tumor.⁷ Table 1.1 lists different histological types of breast cancer as well as their frequency.⁷

Table 1.1 – Histological breast tumor type and frequency^{7,8}

Tumor Type	Frequency
Invasive Ductal Carcinoma, Not otherwise specified	75 %
Invasive Lobular Carcinoma	10 %
All other types – medullary, neuroendocrine, tubular, apocrine, metaplastic, mucinous (A and B), inflammatory, comedo, adenoid cystic and micropapillary	<10%

Breast cancers can also be classified according to their expression of certain markers such as the estrogen receptor (ER), progesterone receptor (PR) and human epidermal growth factor receptor (HER2).^{8,9} The expression of these markers has been shown to correlate with the histological type.⁸ For example, studies have shown that invasive lobular carcinomas are more likely to be hormone receptor positive compared to ductal carcinomas.^{8,10} Arpino et al. have also shown that lobular carcinomas are more likely to be HER2 negative compared to ductal carcinomas.¹⁰

Breast cancer classification based on marker expression is shown in Table 1.2. This classification is different from the histological typing and attempts to account for the different tumor characteristics observed with the expression of these markers.¹¹ The expression of these markers also affects treatment options and patient prognosis.^{7,9} Patients with triple negative tumors – no ER, PR or HER2 expression – typically have the poorest prognosis of all breast cancer patients, while patients with only ER expression in their tumors typically have the best prognosis.⁷

Table 1.2 - Expression of prognostic markers in different breast cancer subtypes.¹¹

Breast Cancer Subtype	Markers Expressed
Luminal A	ER and/or PR, low proliferation
Luminal B	ER and/or PR, high proliferation
	ER and/or PR, HER2
HER2 Positive	HER2
Triple Negative	No markers expressed

1.1.2 Metastatic Process

Most patients do not die from the primary tumor, but rather the metastases that develop.¹² Metastasis is the process through which cancer cells are able to migrate from the site of the primary tumor to distant sites within the body and develop secondary tumors.¹³ This process can occur through several different routes, including the blood and lymphatic system and even through body spaces.¹⁴ The metastatic process involves 5 steps: (1) detachment from the primary tumor, (2) intravasation into blood or lymphatic vessels, (3) arrest at a distant site, (4) extravasation into the new site and (5) growth within the new site, forming a secondary tumor.¹⁴ Figure 1.1 depicts the steps in metastatic process.

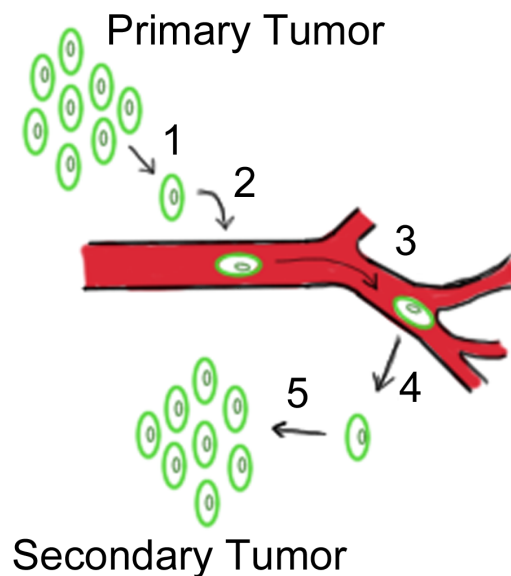


Figure 1.1 - Steps in the metastatic process. (1) Cells detach from primary tumor. (2) Cells intravasate into vessel. (3) Cells arrest at a distant site. (4) Cells extravasate from vessel at distant site. (5) Cells proliferate, forming a clinically detectable secondary tumor.

However, metastasis is an inefficient process.^{12,13,15} The majority of cells that leave the primary tumor are unable to form metastases in a new, distant site.¹³ Once cancer cells arrive at a new site, they can undergo one of three possible fates. They can either die through apoptosis, proliferate to form metastasis or remain in a dormant state.¹⁵

In breast cancer, distant metastases most commonly occur in the liver, lung, brain and bone.¹⁵ The presence of metastases at these sites at diagnosis greatly reduces the likelihood of survival. Metastases to the regional lymph nodes also occurs frequently and the presence of metastases in the sentinel lymph node, which is the first node or set of nodes that drains the region of the primary tumor, has a great prognostic value and is biopsied in the clinic to assess a patient's potential outcome.¹⁶ These sentinel lymph nodes are routinely biopsied in breast cancer and examined for evidence of disseminated cells.¹⁶⁻²⁰ The presence of metastasis in the sentinel lymph node is the best indicator of survival and is independent of tumor volume.²¹

1.1.2.1 Structure and Function of The Lymphatic System

The lymphatic system is an important part of the immune system and also facilitates the return of interstitial fluid to the circulatory system. This system consists of a network of vessels that allow easy access to cells and fluid (or lymph) and lymph nodes that facilitate the immune response. Lymph passes through the nodes where it is monitored for the presence of pathogens. Immune cells can also migrate through this system, such as macrophages, dendritic cells and lymphocytes.

The lymph nodes are secondary lymphoid organs.^{22,23} They contain T cells, which occupy the paracortex, and B cells, which occupy the cortex; specifically the follicles and germinal centers.²³ The medulla, which is near the center of the lymph node, primarily consists of plasma cells and B cells.²² These immune cells are supported by a variety of stromal cells, which include endothelial cells, fibroblastic reticular cells and follicular dendritic cells that produce various chemokines including CCL19, CCL21, CXCL12 and CXCL13, which attract immune cells to the node.²³ The nodes also have a dedicated blood supply where immune cells can also enter the node to participate in the immune response.²²

Afferent lymph enters the node at the outer capsule,^{22,24} where antigens can be presented to T cells by dendritic cells, activating an immune response. Lymph fluid that enters the node then continues to travel towards the center of the node, or medulla, where the efferent vessel allows the lymph to continue on to the next node or the thoracic duct.^{22,24} Figure 1.2 shows the structure of the lymph node and the location of the various immune cells.

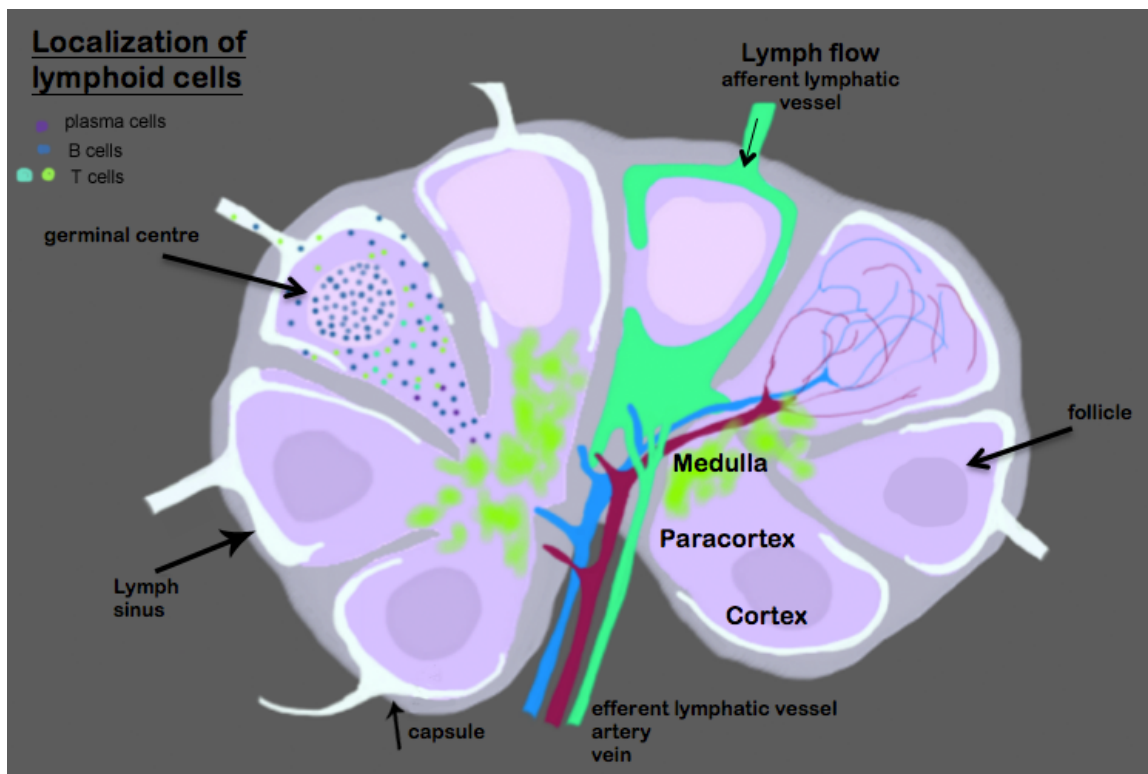


Figure 1.2 - Schematic of lymph node depicting the location of immune cells and various structures. Adapted from reference 22.

1.1.2.2 Role of Lymph Node Metastases in Disease Progression

Metastases from lymphatic vessels will typically occur in the region directly under the lymph node capsule, since this is the first area where disseminated cells will arrest.²⁵ Cells that arrive in the lymph node via the blood can potentially arrest anywhere in the node. The cancer cells can then go on to grow in and engulf the node or metastasize to new sites.

Metastases in the lymph nodes can cause further spread through two different routes, either the lymphatic system or through the lymph node vascular supply.¹⁶ Breast tumor cells are also known to express CXCR4 which is the receptor for CXCL12, which promotes tumor growth and metastases to lymph nodes.^{16,26,27} CXCR4 has also been implicated in the metastasis of hepatocellular carcinoma to the lymph nodes in patients.²⁸

Lymphangiogenesis, the growth of new lymphatic vessels, near the primary tumor and within lymph nodes has also been observed in experimental models and in clinical cases.^{29,30} This process may actually precede the dissemination of tumor cells to the lymph nodes and VEGF-C and VEGF-D have been implicated in this process.^{16,29,31}

There is some controversy about what the significance of micrometastases (lesions between 0.2 and 2 mm) and isolated tumor cells (lesions < 0.2 mm) detected in the sentinel lymph node is on the prognosis of the patient.³² It has been reported that breast cancer patients with micrometastases in the sentinel lymph node have a 5% to 25% incidence of metastases in a non-sentinel lymph nodes, while patients with macroscopic metastases in the sentinel node have an incidence of 40% to 60%.³³

1.1.3 Tumor Microenvironment and Heterogeneity

Tumors do not consist of only cancer cells. There are many different types of host cells that are part of the tumor which form the stroma that supports the survival and growth of the cancer cells. The stroma can include fibroblasts, mesenchymal stem cells, macrophages, various immune cells (eg. T-cells and neutrophils), and even adipocytes.²⁶ These cells interact with the transformed cancer cells through various cytokines and growth factors, creating an environment that supports the growth of the tumor.²⁶ These stromal cells, are also able to regulate the extracellular matrix which creates an environment that promotes altered metabolism, invasiveness and decreased apoptosis.³⁴ All these cancer-stroma interactions contribute to the development of the various hallmarks of cancer and cause tumors to be very complicated systems.³⁵

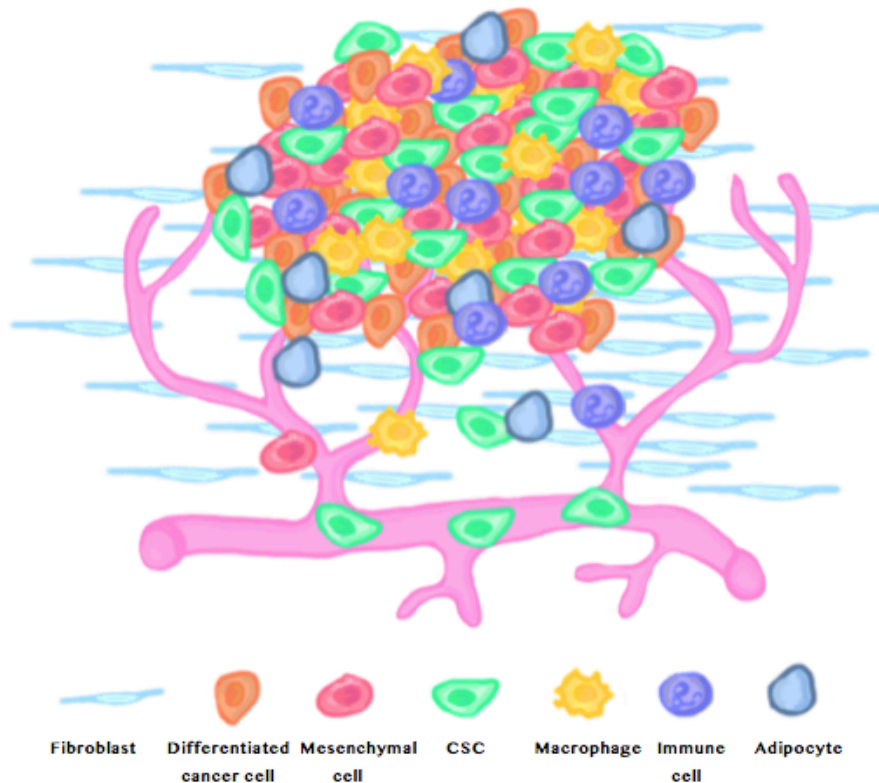


Figure 1.3 – The tumor microenvironment. There are many different types of cells within a tumor, some of which support the growth and survival of cancer cells through cellular interactions. Adapted from reference 26.

Even though there are a wide variety of cells within a tumor, the transformed cancer cells themselves are also heterogeneous in their phenotype and behavior including invasiveness and metastatic potential.³⁶ Some cancer cells will be more proliferative than others and the expression of particular surface markers or enzymes will also vary. For example in breast cancer, tumors can be classified as basal or luminal, but will have populations of cancer cells that have phenotypes from both classes.³⁶

There are two different theories that attempt to explain the heterogeneity observed within populations of tumor cells, one is the clonal evolution model and the other is the hierarchical model.^{37–39} In the clonal evolution model, different subpopulations are generated by random

mutations that occur within the cells, enabling some populations to be more invasive while hindering the survival of others.³⁷⁻³⁹ In the hierarchical model, the diversity within the tumor is due to a stem cell like structure similar to those found in normal tissues.³⁷ At the top of the hierarchy is the cancer stem cell (CSC), or tumor initiating cell, which is capable of self renewal and producing progeny of the cellular subtypes within the tumor cell population.³⁷⁻⁴⁰ CSCs are discussed in section 1.1.5.3. In reality, both of these models of heterogeneity exist within a tumor, with the impact of each varying between tumors types.^{37,38,40} This allows multiple populations to survive within a tumor and can affect the tumor's resistance to certain therapeutics.

The tumor will also evolve over time and have many different subpopulations that will appear and disappear due to acquired mutations that can impact the success of treatment. Studies of cancer cells using dyes such as BrdU and CFSE have revealed that there is heterogeneity in the retention of these labels over time in breast cancer,^{41,42} gastrointestinal cancer⁴³ and head and neck cancers, highlighting the existence of multiple cancer cell populations with different cycling times, which impacts the effectiveness of current therapies.⁴⁴ These studies have shown that there is a difference in how these label-retaining cells respond to chemotherapy; Moore et al. showed a increase in the percentage of label-retaining cells following treatment with oxaliplatin, 5-fluorouracil or combination of the two drugs.⁴¹

1.1.4 Dormancy

Dormancy is defined as a state in where minimal disease, such as single cells or micrometastases exists, and remains clinically undetectable for extended periods of time.⁴⁵ These cells are thought to be able to persist in this dormant state for long periods of time, only to be triggered to proliferated by unknown signals.^{15,46,47} Dormancy is frequently observed in breast cancer as well as many other tumor types.⁴⁸ Patients will be treated successfully for the primary tumor, only to experience recurrence at a much later time, from a few years to over a decade.^{47,49} These dormant cancer cells are much more difficult to treat since many available therapies target actively dividing cells and the outcome tends to be worse for patients who experience recurrence after a period of dormancy.⁵⁰

Dormancy can be divided into cellular and tumor dormancy. Each of these processes can occur during metastasis, with the amount of cells progressing from cellular dormancy to micrometastases, and the number of micrometastases progressing from tumor dormancy to secondary tumors, dramatically decreasing at each stage.^{47,49,51-53} Figure 1.4, which is adapted from work in Dr. Ann Chambers lab, shows the later stages of the metastatic process and the percentage of cells that are predicted to progress from each stage to the next, as well as the percentage that remain dormant at each stage. These processes involve different mechanisms for maintaining as well as escaping from dormancy.

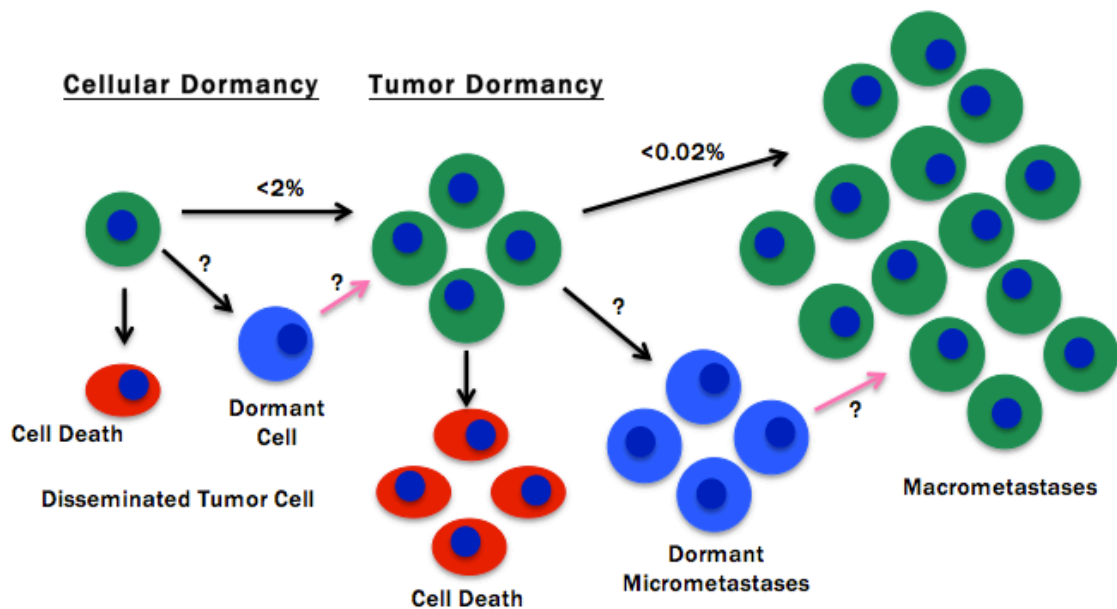


Figure 1.4 – Dormancy and inefficiency of metastatic process. Only a small percentage of the tumor cells that arrest at a second site will go on to form micrometastases and macrometastases. The majority of cells will undergo apoptosis or will remain in a dormant state. Less than 2 % of arrested cells will form micrometastases and less than 0.02% of those micrometastases will develop into macrometastases in experimental metastasis models. The question marks in the figure represent quantities that are unknown. The number of cells that will enter a dormant state after arrest is not known as well as the percentage of dormant cells or micrometastases that develop into macrometastases. Adapted from reference 15.

1.1.4.1 Tumor Dormancy

A primary tumor or a micrometastasis can remain undetectable for a long period of time. This type of dormancy is defined as having near equal amounts of proliferation and cell death occurring within the tumor mass.¹⁵ This balance of proliferation and cell death may be due to the fact the new tumor has not yet been able to escape the limits that are placed on it by the immune system, nutrient supply and microenvironment.^{15,46,50} The number of tumors or metastases that escape dormancy is low, with most remaining clinical undetectable and asymptomatic potentially for decades.^{50,54,55}

1.1.4.2 Dormancy of Single Cancer Cells

Cells that leave the primary tumor and arrest at a new site can remain dormant, die or proliferate. Studies have shown that single disseminated cells in an experimental metastasis model can co-exist with micro- and macro-metastases.^{49,51-53} These single cells have been found to be viable and not actively undergoing cell division (low Ki67 expression).^{49,51,53} Townson et al. and Heyn et al. have used iron oxide nanoparticles to label and track the development of metastatic lesions and the persistence of non-proliferative cancer cells in experimental melanoma and breast cancer metastasis models.^{47,52} Naumov et al. have used fluorescent nanoparticles to track the location of dormant tumor cells in an experimental breast cancer metastasis model.⁴⁹ Using intravital videomicroscopy, they showed that solitary label retaining cancer cells could be detected in the liver in situ that were not actively proliferating or undergoing apoptosis.⁴⁹ Other studies have investigated the mechanism that might be maintaining the dormant population and potentially allowing cells to escape dormancy, and have suggested that signals from the extracellular matrix interacting through integrins may be a factor in regulating both maintenance and escape.^{46,56}

It has been suggested that dormant tumor cells may also be resistant to treatments that target actively dividing cells. Towson et al. demonstrated that chemotherapeutics have little effect on dormant, or label retaining cells.⁵² They found that while treatment with doxorubicin had a significant effect on metastasis volume, it did not impact the number of non-proliferative

cells that could be detected within MR images of the liver.⁵² Ranganathan et al. have also shown that increased p38 signaling induces dormancy and resistance to etoposide and doxorubicin in a human epidermoid carcinoma cell line.⁵⁷

1.1.4.3 Cancer Stem Cells

Cancer stem cells (CSC) or tumor initiating cells are a subset of tumor cells that are able to form tumors and potentially metastases.^{37,39,40,58} These cells possess characteristics similar to normal stem cells, which include slow proliferation, increased resistance to chemotherapeutic drugs, unlimited proliferative potential, the ability to differentiate into all tumor cell subpopulations and use of similar signaling pathways.^{40,58}

Functionally, these cells have been defined through limiting dilution assays conducted in various strains of immune compromised mice.³⁷ In these assays, cells are sorted by flow cytometry into tumorigenic and non-tumorigenic populations. Bonnet and Dick determined that cells that were both CD34 positive and CD38 negative were capable of initiating leukemia in NOD/SCID mice⁵⁹ while Al-Hajj et al. determined that tumor growth could be initiated by cells that were CD44 positive, CD24 negative and ESA positive.⁶⁰ Other markers have been identified for other tumor types, for example, CD133 for colon, prostate and potentially lung cancer⁶¹⁻⁶³ and CD133 and nestin for glioma.^{64,65} High expression of other markers such as aldehyde dehydrogenase (ALDH), integrin alpha 6 (CD49f) and CD133 have also been reported as being markers of breast CSCs.⁶⁶⁻⁶⁸ However, defining these populations based on surface markers may not be the most effective method for identification. These markers may vary between patients and multiple stem-like populations may exist in one tumor.³⁷ Identifying these cells using functional markers, such as the retention of a label or the activation of specific enzymes, may be more effective.

Recent work suggests that CSCs may actually play a role in the dormancy of single cells.¹⁵ The observation of slow progression through the cell cycle, or non-proliferation (extended G₀/G₁), is a feature of normal stem cells that can also be characteristic of certain CSC populations.^{40,69,70} Recently, studies of label retaining cancer cells have shown that these cells may possess stem-like characteristics and are capable of initiating tumor growth.⁴³ Some

studies also show that a specific subset of CSCs may be responsible for metastasis.^{66,71,72} Other work has shown that the Epithelial to Mesenchymal Transition (EMT) may also generate cells with a stem-like phenotype and may be needed for CSCs to metastasize.^{73,74} The role that CSCs play in tumor progression, dormancy and metastasis still needs to be elucidated and only then will the full impact of this population on disease progression be understood.

In order to gain a better understanding of metastasis, cellular dormancy and the role that CSCs or tumor initiating cells and the microenvironment may play in these processes, new techniques need to be developed that allow for these concepts to be studied in vivo over time and therapeutic approaches to be validated. Cellular MRI is a technique that may allow for these processes to be studied non-invasively and help push our knowledge forward on these subjects.

1.2 Cellular MRI

Cellular MRI is an imaging technique that incorporates high resolution MRI and cells labeled with contrast agents to visualize the location and behavior of these cells in vivo. The following sections give a brief description of basic MRI principles, pulse sequences, contrast agents and the principles and applications of cellular MRI.

1.2.1 Nuclear Magnetic Resonance (NMR)

Magnetic resonance imaging can be accomplished due to the intrinsic property of subatomic particles called spin (or the intrinsic angular momentum of the particle).^{75,76} All protons, neutrons and electrons have a non-zero value of spin. For the purpose of this work, protons will be the main particle discussed.

Both the proton and neutron have a spin equal to $\frac{1}{2}$. In nuclei with multiple protons and neutrons, the spin of the entire nucleus will be a sum of the spins from all unpaired protons and neutrons. Nuclei with a non-zero spin will have a magnetic dipole and have a magnetic moment.⁷⁵

When a proton, which has a spin of $\frac{1}{2}$, is exposed to a magnetic field, it will experience a force that will cause it to align with the field. However, the proton will not align completely and will precess about an axis that is parallel with the applied field. The frequency of the proton's precession or the Larmor frequency, ω_0 , in an external magnetic field, B_0 , is given by the following equation⁷⁶:

$$\omega_0 = \gamma B_0$$

Where γ is the gyromagnetic ratio, which is 42.57 MHz/T for a proton.⁷⁶ When an external magnetic field is applied to a volume containing many protons, as is the case in MRI, a net magnetization is produced within the volume that aligns with the magnetic field.^{75,76} In the volume, not all of the protons will precess around a direction that will constructively add to the net magnetization, but will precess in a way that reduces the size of the magnetization available for imaging. This is dependent on both the magnetic field strength and the temperature of the volume. The magnitude of the net magnetization, M_0 , is given by the following equation⁷⁶:

$$M_0 = \frac{\rho \gamma^2 \hbar^2 B_0}{4 kT}$$

Where ρ is the density of protons within the volume, \hbar is Planck's constant divided by 2π , k is Boltzmann's constant and T is absolute temperature. When an MRI image is acquired, an oscillating magnetic field, B_1 , is applied to the volume in addition to B_0 , exciting the protons.⁷⁵ This causes magnetization to tip from the z-axis, which is parallel to B_0 , into the transverse plane perpendicular to B_0 .^{75,76} The magnetization will then gradually return to its original orientation parallel to the z-axis once B_1 has been switched off.⁷⁶ The signal measured by the imaging system during acquisition is the relaxation of the magnetization back to the equilibrium state.^{75,76} During the acquisition process, a series of magnetic field gradients in different spatial directions are applied to encode different frequencies and phases to different areas of the volume, allowing for the location of specific signals to be determined.^{76,77}

The signal is detected due to the precession of the magnetization in the transverse plane. This induces a varying voltage and current in a coil that is placed nearby for detection. The

magnetization as a function of time in the z-axis and transverse plane is given by the following equations.⁷⁶

$$M_Z = M_0(1 - e^{-t/T_1})$$

$$M_{XY} = M_0 e^{-t/T_2}$$

Where T1 and T2 are relaxation time constants that describe how the magnetization within a volume will return to equilibrium. These constants are known as spin-lattice and spin-spin relaxation, respectively, and vary between tissues. These time constants are discussed in sections 1.2.2.

1.2.2 T1 and T2 Relaxation

The process of relaxation involves two different mechanisms: T1 relaxation and T2 relaxation.⁷⁵ These mechanisms are extremely important in determining image contrast and affect the choice of pulse sequence used for imaging. The relaxation constants vary between tissues and will also change in the presence of disease.⁷⁶ Table 1.3 shows the normal T1 and T2 relaxation times for different tissues at 1.5T.

Table 1.3 - Approximate values of relaxation times at 1.5 T ⁷⁷

Tissue	T1 (ms)	T2 (ms)
Grey matter	920	101
White matter	790	92
Cerebrospinal fluid (CSF)	2650	280
Kidney	650	58
Liver	490	43
Skeletal muscle	870	47

T1, or spin-lattice relaxation, refers to the transfer of energy from the excited protons to other elements within the immediate surroundings. These include other molecules and nuclei that possess a magnetic moment.

The longitudinal magnetization, M_z , will recovery as an inverse exponential, becoming asymptotic as it reaches its original pre-excitation value. The T1 relaxation time is defined as the time for the magnetization to return to 63% of the pre-excitation value along the longitudinal or z-axis. ^{75,76} Figure 1.5 shows the recovery of the longitudinal magnetization and decay of the transverse magnetization.

T2, or spin-spin relaxation, refers to the interactions within the pool of protons that is available for imaging. When protons are in close proximity of each other, each proton will induce a slight shift in the main magnetic field that other protons will experience. This causes the protons to precess at frequencies that are slightly above and below the Larmor frequency, inducing dephasing in the transverse plane. During this process, there is no net transfer of

energy outside of the system. Transfer of energy outside of the system only occurs during T1 relaxation.^{76,78}

The transverse magnetization, M_{XY} , will decay exponentially until it reaches a value of 0, as shown in Figure 1.5. The T2 relaxation time is defined as the amount of time for the transverse magnetization to decay to 37% of the original value in the transverse plane.^{75,76} T2 relaxation occurs much more quickly than T1 relaxation, with T2 values typically 10 times shorter than T1 values.

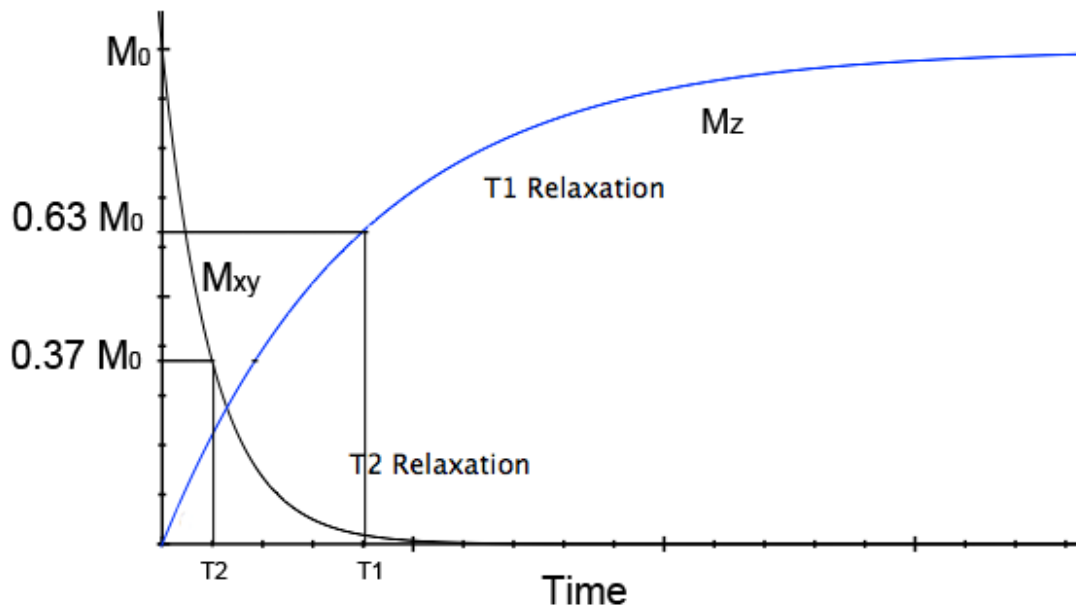


Figure 1.5 - Relaxation curves for transverse (M_{XY} , black) and longitudinal (M_Z , blue) magnetization. Adapted from reference 76.

Both T1 and T2 relaxation times are dependent on the strength of B_0 . All molecules in a tissue will be moving at different frequencies, which can be described by the spectral density function. Exchange can only occur between excited protons and surroundings that are at the same frequency on the spectral density function. As the frequency increases, the amount of protons or other nuclei moving at that frequency decreases. Because of this effect, T1 will increase as B_0 increases since there are fewer protons available in the surroundings for

exchange, requiring more interactions with the surroundings to dissipate the magnetization and therefore more time.⁷⁶

Increasing B_0 has a smaller effect on T2 relaxation times.^{76,78} There is an increase in field inhomogeneities with increasing B_0 that affects the apparent T2 relaxation time ($T2^*$). The $T2^*$ relaxation time accounts for both T2 effects and field inhomogeneities and will shorten as the field strength increases.

1.2.3 Pulse Sequences

Pulse sequences consist of a series of timed applications of spatial field gradients and radiofrequency (RF) pulses that are used to measure the signal produced from excitation. There are two main timing parameters: TR, or the repetition time, and TE, or the echo time. TR represents the amount of time from one RF excitation pulse to the next RF excitation pulse in the next repetition of the pulse sequence. TE is the time from the RF excitation pulse to the echo of the signal. The signal echo can be produced by either an RF pulse or gradient pulse, allowing sequences to be classified as spin echo or gradient echo type, depending on which of these methods is used.⁷⁶

1.2.3.1 Spin Echo Sequences

Spin echo (SE) sequences consist of a 90° RF pulse followed by a 180° RF pulse at time $TE/2$. The 180° RF pulse refocuses the spins, which are dephasing prior to the pulse. A timing diagram of a basic SE sequence is shown in Figure 1.6.

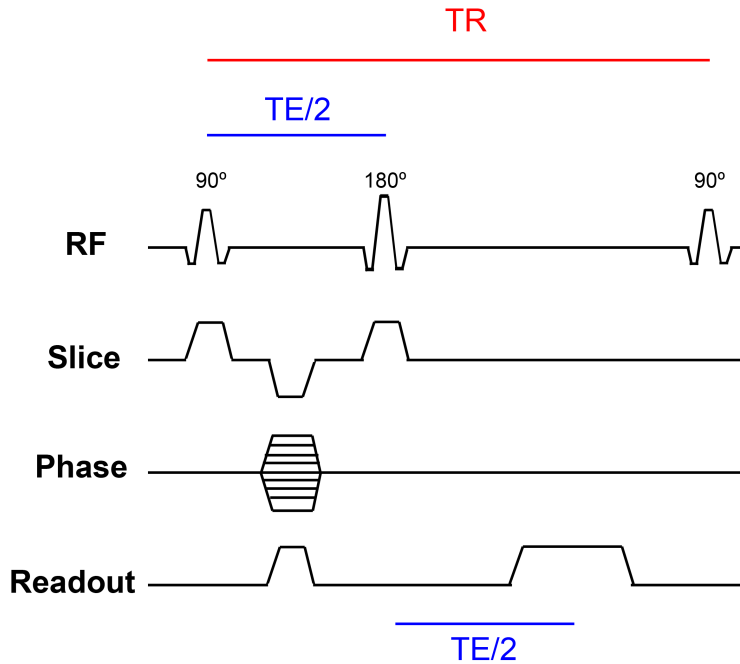


Figure 1.6 - Single spin echo sequence timing diagram. Adapted from reference 75.

By adjusting TR and TE, different contrasts can be generated with a SE sequence, including T1 weighted, T2 weighted and proton density weighted. Table 1.4 shows how these parameters can be adjusted to generate these contrasts. Some common SE sequences include: Single spin echo, Turbo spin echo (TSE) and Half Fourier acquisition turbo spin echo (HASTE).

Table 1.4 - Pulse sequence timing parameters and associated image contrasts

	Long TE	Short TE
Long TR	T2 Weighted	Proton Density Weighted
Short TR	Not Used	T1 Weighted

1.2.3.2 Gradient Echo Sequences

Gradient echo (GE) sequences use the gradients to refocus the spins after dephasing. These sequences begin with an RF excitation pulse with a flip angle that is smaller than 90° , allowing for faster imaging. After the excitation pulse, a negative gradient is applied to bring individual spins back into phase. This technique does not account for dephasing due to field inhomogeneities, making these sequences sensitive to $T2^*$ effects. Figure 1.7 shows the timing diagram for a simple GE sequence.

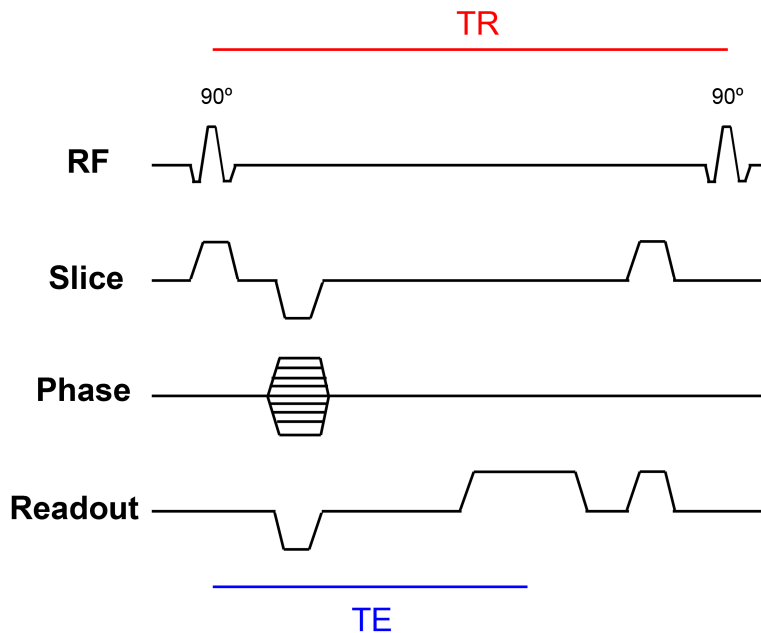


Figure 1.7 - Timing diagram for basic gradient echo sequence. Adapted from reference 75.

The contrast in GE sequences is dependent on the flip angle of the RF pulse, TR and TE. In basic GE sequences, the TR time is relatively long (500 ms) while in basic fast GE sequences, the TR time is very short (100 – 150 ms).⁷⁵ TR times in GE sequences are much shorter than those in SE sequences because the smaller flip angles used in GE allows for part of the longitudinal magnetization to remain intact, shortening the time required to return to equilibrium.⁷⁵ Table 1.5 shows how the flip angle and TE can be varied to achieve different contrasts with basic GE sequences.

Table 1.5 - TE and flip angle for achieving different contrasts with basic GE sequences^{75,79}

	Short TE (<10 ms)	Long TE (25 – 30 ms)
Small Flip Angle (15° – 20°)	Proton Density Weighted	T2* Weighted
Intermediate Flip Angle (40° – 50°)	T1 Weighted	
Large Flip Angle (>80°)	Strong T1 Weighted	

In fast GE sequences, the TR is less than the T2 time, causing the relationship between image contrast and imaging parameters to become more complex.⁷⁹ Most imaging in the clinical setting uses the fast GE sequences, since the longer TR times lead to increased acquisition times.⁷⁹ Some commonly used GE sequences are: Fast low-angle shot (FLASH) which produces T1 weighted contrast and balanced steady state free precession (bSSFP) which produces T2/T1 weighted contrast.^{79,80}

Work in the following chapters has primarily used the bSSFP pulse sequence to acquire images. The following section describes this sequence and its usual applications.

1.2.3.3 balanced Steady State Free Precession (bSSFP)

The balanced steady state free precession (bSSFP) sequence is similar to other fast GE sequences, except in bSSFP the application of the gradients are balanced. All applications of each gradient in the positive direction are balanced with application in the opposite direction,

causing the net gradient area to be zero.⁷⁹⁻⁸¹ This leads to the refocusing of the magnetization before the next RF pulse, conserving as much signal as possible and generating a high signal to noise ratio.⁷⁹ However, this technique is very sensitive to field inhomogeneities since these cause dephasing of the magnetization leading to a decrease in signal.⁸⁰ The timing diagram for this pulse sequence is shown in Figure 1.8.

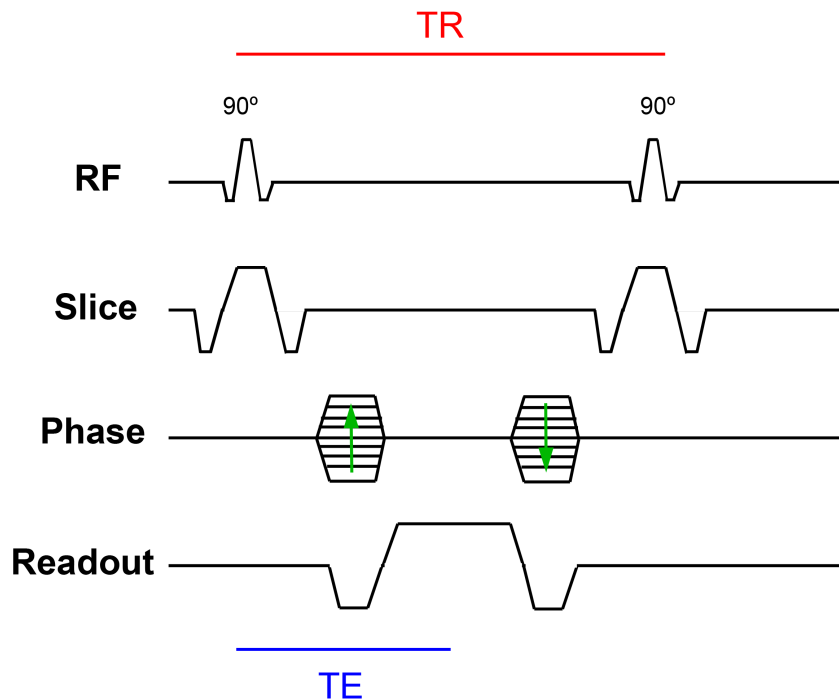


Figure 1.8 - Pulse sequence diagram of bSSFP pulse sequence. The net gradient area for each applied gradient is zero. Adapted from reference 80.

The on-resonance signal intensity in bSSFP is given by the following equation, assuming that $TR \ll T1$ and $T2$:⁸⁰

$$M_{SS} = M_0 \frac{\sin \alpha}{1 + \cos \alpha + (1 - \cos \alpha) \left(\frac{T1}{T2} \right)}$$

The optimal flip angle for achieving the greatest signal intensity possible is given by the following equation and is dependent on the T1 and T2 of the tissue:⁸⁰

$$\cos \alpha = \frac{\frac{T1}{T2} - 1}{\frac{T1}{T2} + 1}$$

At the optimal flip angle, the on-resonance signal intensity simplifies to:⁸⁰

$$M_{SS} = \frac{1}{2} M_0 \sqrt{\frac{T2}{T1}}$$

When T1 and T2 values for a tissue are similar, for example: fat and fluids, the signal intensity approaches half of the initial magnetization. These contrast characteristics and the speed at which this pulse sequence can be run make it ideal for cardiac and vascular imaging.^{79,80} bSSFP is also used in body imaging in oncology due to its increased SNR and lower susceptibility to motion artifacts.⁸² bSSFP has also recently been used in fMRI, but not to a great extent.⁸¹

1.2.4 Principles of Cellular MRI

Cellular MRI utilizes high resolution MRI and cell labeling to study the fate of cells in vivo. In most studies cells are labeled with iron oxide nanoparticles. Intracellular iron results in shortening of the T2 relaxation time locally,⁸³ causing a region of signal loss, typically much larger than the actual area occupied by the nanoparticles. This occurs because the large magnetic susceptibility of these agents produce a large local change in the magnetic field inhomogeneity, which changes the magnitude of the local field enough that the Larmor frequency of the protons within the vicinity is altered. This change in Larmor frequency causes dephasing of protons and prevents them contributing to the generation of MR signal.⁸⁴

Iron oxide nanoparticles are usually classified by their size, as either (i) ultra small iron oxide particles (USPIO), (ii) standard superparamagnetic iron oxide particles (SPIO) or (iii) micron-sized iron oxide particles (MPIO).^{83,84} The USPIO particles are 10-20 nm in diameter while SPIO particles are usually 50-100 nm. Particles in the MPIO category are

approximately 1 μm in diameter.⁸³ USPIO and SPIO particles are typically coated with a biodegradable dextran; examples are Combidex® and Feridex®. MPIO particles, such as Bangs Beads, consist of iron oxides coated with silica, or other polymers such as polystyrene, or of iron oxides embedded within a polymer matrix. MPIOs contain much more iron per particle compared to USPIO and SPIO. For example, a single 0.9 micron Bangs beads contains approximately the same amount of iron as 4.3×10^6 USPIO or 1.5×10^6 SPIO particles.⁸⁵ Magnitsky et al. have shown that cells labeled with 45 $\mu\text{g Fe/mL}$ MPIO contain approximately twice as much iron per cell compared to cells labeled with 100 $\mu\text{g Fe/mL}$ SPIO and approximately 6 times as much iron as cells labeled with 100 $\mu\text{g Fe/mL}$ USPIO.⁸⁶ Because MPIO are non-biodegradable these particles have only been used for preclinical research.

Most types of cells can be labeled with iron particles by simple co-incubation. Iron particles are taken up by endocytosis and compartmentalized within endosomes in the cell cytoplasm. To enhance iron uptake or to facilitate the labeling of non-endocytic cell types (ie. T cells) transfection agents can be used; mixing transfection agents with iron particles prior to labeling forms complexes, which shuttle the iron into the cells.^{84,87}

To improve cell detection by MRI the goal is to have cells take up as much iron as possible without impacting on the normal cell viability, phenotype or function. Most studies report no detrimental effects of iron particles on the cell at the typical labeling concentrations used for MRI. Very high levels of labeling, however, can lead to signs of toxicity including decreased proliferation, production of free radicals and cell death.⁸⁴

Most cellular MRI studies use high field strengths to achieve high-resolution imaging, but clinical systems with specialized hardware have also been used. Each of these systems have their own advantages and disadvantages, with high field systems allowing faster acquisitions but at the cost of increased magnetic field inhomogeneity, while low field systems tend to be more homogenous but also have increased acquisition times due to a lower intrinsic signal.

Currently, there are no iron agents approved for clinical use in North America. In the past Feridex was approved for clinical use in the U.S.A and Canada and was widely used in the MRI clinic for visualization of liver tumors. For this application Feridex was administered intravenously (iv) and normal liver macrophages engulfed the iron particles causing normal

tissue to appear with very low signal intensity, and therefore, abnormal liver tissue (tumors) to appear bright. Feridex was taken off-market in 2008 for financial reasons. In Europe and Asia, some USPIO remain approved for clinical use and are mostly administered iv to detect inflammation in diseases such as atherosclerosis and multiple sclerosis (MS).^{88,89}

1.2.5 Preclinical Applications of Cellular MRI

Cellular MRI has been used to track the fate of various types of cells in preclinical disease models. Many of these studies have been focused on tracking the fate of stem cells in a range of small animal models of injury and disease.⁹⁰⁻⁹⁷ The goal is to use in vivo longitudinal imaging to identify the location of the cells after their transplantation and to monitor their migration within the host tissue, or to other sites.

Some examples of stem cell tracking have included the tracking of stem cells after their intracardiac transplantation in rat and pig models of myocardial infarction,^{94,95} the survival and migration of multipotent stromal cells and embryonic stem cells in spinal cord injury models, as well as the engraftment and migration of neural stem cells in animal models of stroke and multiple sclerosis.^{91,93,96,97}

Cellular MRI has also been used to monitor the survival of transplanted pancreatic islets. Herynek et al. used a dual contrast approach to monitor SPIO labeled islet transplanted into the liver of rats.⁹⁸ Jung et al. have used heparin conjugated SPIO to labeled islets prior to transplantation and monitored the grafts for 30 days in nude mice.⁹⁹ Isogenic and allogenic islets have also been imaged after transplantation into the live of mice, where function of the grafts was monitored by measuring blood glycemia¹⁰⁰ and more recently by using automated detection on MRI.¹⁰¹ Work by Medarova et al. have demonstrated the feasibility of tracking Feridex labeled islets in baboons, showing safety and long term function of the islets.¹⁰²

Monitoring immune cells is another growing application of cellular MRI. Baeten et al. have tracked the migration of myelin reactive, SPIO labeled T cells injected intravenously in both naïve and EAE induced rats, finding differences in the cells' migration patterns between the groups.¹⁰³ Ahrens et al. have demonstrated that dendritic cells can be effectively labeled with anti-CD11c SPIO in vitro and that these cells could be detected in vivo following

transplantation into quadriceps of mice.¹⁰⁴ Dekaban et al. and Zhang et al. were able to monitor and to quantify both mouse and human dendritic cell migration to lymph nodes in mice after injection into the hind footpad.^{105,106} Work by Baumjohann et al. has tracked the migration of dendritic cells to lymph nodes after injection into the hind footpad, both correlating MRI signal loss with cell number and showing migration of labeled dendritic cells into T cell rich areas of lymph nodes.¹⁰⁷ Joo et al. have examined the effect of prostaglandin E2 on the migration of SPIO labeled mouse dendritic cells in vivo, demonstrating increased migration in prostaglandin treated groups.¹⁰⁸ Ferguson et al. have monitored the effectiveness of immunotherapy with SPIO labeled dendritic cells in a mouse model of thymoma.¹⁰⁹ They showed that dendritic cells primed with an antigen expressed on the thymoma cells produced greater tumor free survival rates than compared to naïve cells and cell primed with a different antigen.¹⁰⁹

One of the limitations of cell tracking with iron oxide nanoparticles is the challenge of quantifying cell number. In vitro studies have demonstrated that the amount of signal loss that is generated from iron oxide nanoparticles, or the R2 value, is dependent on the concentration of iron within a voxel as well as the voxel volume, pulse sequence and the field strength used for imaging.^{84,110,111} The relationship between iron concentration and signal loss is linear (within a range of low iron concentrations), but this relationship changes when the image resolution is increased.^{110,112} Increasing the field strength will also increase the sensitivity to iron, allowing for lower iron concentrations to be detected. Quantification of the number of cells in a voxel in vivo using R2 values is more challenging. These values will be dependent on the tissue and can change over time if cells are monitored in longitudinal studies.¹¹²

Another limitation of cell tracking with iron and MRI is that the iron label will be diluted in proliferating cells. Eventually, the iron content of the cells will fall below the detection limit with MRI. Because of this relatively few studies have used cellular MRI techniques to track cancer cells.^{31,47,52,69,86,113,114} However, we and others have shown that the retention of iron particles in nonproliferative, or slowly cycling, cancer cells can be exploited to detect particular cancer cell populations. Heyn et al. were the first to demonstrate that nonproliferative cancer cells could be tracked by virtue of their retention of iron particles. In this study metastatic breast cancer cells were iron-labeled and injected into the left ventricle

of the heart for delivery to the brain. Once arrested they appeared as discrete signal voids by MRI. Over time most of these voids disappeared as they died and were cleared, a small percentage of the voids developed into brain metastases and a small percentage of the voids remained for one month, throughout the experiment.⁴⁷ Townson et al. injected iron-labeled metastatic melanoma cells into the mouse liver and used MRI to show that cytotoxic chemotherapy with doxorubicin reduced liver tumor burden but did not affect the number of nonproliferative cancer cells.⁵²

Magnitsky et al., showed that USPIO, SPIO and MPIO could be used to track slowly-cycling cells in human melanoma tumors grafted subcutaneously in mice for up to 6 weeks.⁸⁶ Gazdzinski et al. were able to map the distribution of MPIO-labeled cancer cells in a mouse glioma models as tumors developed over time and found that iron-retaining cells were distributed differently in different tumor types with retention of the label in the center of the tumor being a feature of the more invasive tumors.⁶⁹ Wu et al. have examined the retention of SPIO particles in human pancreatic cancer xenografts in nude mice for up to 3 weeks while comparing a variety of pulse sequences, and also demonstrated retention of iron labeled cells in the center of tumors.¹¹³

Other work has shown that iron-labeled cancer cells can be visualized within the lymph nodes of mice.^{31,114,115} Foster et al. demonstrated that as few as 1,000 MPIO labeled B16F10 cells could be detected in the inguinal lymph node after direct intranodal injection.¹¹⁵ Kosaka et al. have shown that breast cancer cells that were labeled with SPIO and quantum dots and then injected in the foot pad of mice can be detected migrating to the draining lymph nodes with both MRI and optical imaging.¹¹⁴ Liu et al. have also been able to visualize SPIO labeled colon carcinoma cells injected into the foot pad migrating to the draining lymph nodes.³¹

1.2.6 Clinical Applications of Cellular MRI

At present, there have been only a few clinical trials that have utilized iron oxide nanoparticles and MRI in patients. Importantly, all of these trials have been conducted outside of North America because of the lack of agents approved for patients.^{116,117}

Several of these studies have focused on tracking the fate of transplanted stem cells. For example, Zhu et al. (China) implanted Feridex labeled neural stem cells directly into the brain in patients with traumatic brain injury and demonstrated engraftment and migration to the site of injury.¹¹⁸ Callera and De Mello (Brazil) labeled autologous bone marrow derived CD34+ cells with magnetic beads targeted to CD34 and implanted these cells directly into the spinal cord of patients with spinal cord injury, observing migration of the cells from the injection site to the injury.¹¹⁹ The transplantation of Feridex labeled mesenchymal stem cells in amyotrophic lateral sclerosis (ALS) and MS has also been monitored using MRI by Karussis et al (Israel).¹²⁰

There is also interest in the utility of cellular MRI for monitoring the fate of pancreatic islets transplanted for treating diabetes. Saudek et al. (Czech Republic) were the first to demonstrate that Resovist-labeled islets could be safely labeled and that their survival in the liver could be monitored in type I diabetes patients.¹²¹ Toso et al. performed a similar study (Switzerland) where pancreatic islets were labeled with SPIO particles prior to transplantation into patient livers and have shown a therapeutic effect for up to 2 years in one patient.¹²²

Cellular MRI has also been used in immunotherapy studies to track SPIO-labeled dendritic cells after intranodal injection in melanoma patients (Netherlands).¹²³ One of the major findings of this study was that the rate of successful injections was lower than expected, at approximately 40%, which was unknown prior to this study.¹²³ This study demonstrated the utility of cellular MRI in determining if the initial transplantation and delivery of cells was successful.

The USPIO, ferumoxytol (Feraheme®), has recently been used for human MRI studies. This particle is approved for use as an intravenous iron supplement in patients with iron deficiency anemia and chronic kidney disease.¹²⁴ Current research has shown that this particle can be used for angiography as well as cell tracking.¹²⁵⁻¹²⁷ A clinical trial investigating the use of ferumoxytol for the detection of lymph node metastases for pre-operative staging is currently ongoing with completion expected in October 2013 (clinicaltrial.gov identifier: NCT00920023).

1.3 Goal and Objectives

The overall goal of this thesis was to use MRI to study the development of tumors in models of breast cancer with an emphasis on the detection of metastasis to lymph nodes. To accomplish this we had three main objectives:

1. To assess the normal MRI appearance and volume of the lymph nodes and spleen in immune-compromised mouse strains typically used in cancer research.
2. To use longitudinal MRI to characterize tumor growth and metastasis in four different murine models of breast cancer.
3. To use the concept of iron-label retention in cells to detect and track the subpopulation of slowly-cycling (or nonproliferative) cancer cells within mammary fat pad tumors and the lymph nodes in a mouse model of metastatic breast cancer.

The work described in Chapter 2 examines the normal MRI appearance and the volume of the lymph nodes and spleen in three different immune-compromised mouse strains, and investigates how exposure outside the pathogen free housing and repeated imaging sessions affect these. The work presented in this chapter has been published in *PLoS One* 2011; 6(11): e27508.

In Chapter 3 we used high resolution MRI to study cancer progression in four different orthotopic breast cancer models, which consisted of two immune compromised mouse strains implanted with two different human breast cancer cell lines. MRI was used to measure the volume of primary tumors and the frequency of metastases to draining lymph nodes from the implanted tumor. We compared MRI with traditional histology based methods for analysis.

In Chapter 4 we used cellular MRI to examine the behavior of MPIO retaining cancer cells in vivo and evaluated the usefulness of cellular MRI for tracking non-proliferative cancer cells. We monitored the evolution of signal loss over time in the primary tumor as well as observed migration of the label retaining cells to draining lymph nodes. This work has been published in *Translational Oncology* 2013; 6(3): 347-354.

1.4 References

1. Canadian Cancer Society, Statistics Canada, Provincial/Territorial Cancer Registries & Public Health Agency of Canada *Canadian Cancer Statistics 2012*. (2012).
2. King, R. J. B. *Cancer Biology*. (Pearson Education Limited: Harlow, England, 2000).
3. Hanahan, D., Weinberg, R. A. & Francisco, S. The Hallmarks of Cancer. *Cell* **100**, 57–70 (2000).
4. Hanahan, D. & Weinberg, R. a Hallmarks of cancer: the next generation. *Cell* **144**, 646–74 (2011).
5. Pietras, K. & Ostman, A. Hallmarks of cancer: interactions with the tumor stroma. *Experimental Cell Research* **316**, 1324–31 (2010).
6. Cavallo, F., De Giovanni, C., Nanni, P., Forni, G. & Lollini, P.-L. 2011: the Immune Hallmarks of Cancer. *Cancer Immunology, Immunotherapy : CII* **60**, 319–26 (2011).
7. Bertos, N. R. & Park, M. Breast cancer — one term, many entities? *J Clin Invest* **121**, 3789–3796 (2011).
8. Li, C. I., Uribe, D. J. & Daling, J. R. Clinical characteristics of different histologic types of breast cancer. *British Journal of Cancer* **93**, 1046–52 (2005).
9. Masuda, S. Breast cancer pathology: the impact of molecular taxonomy on morphological taxonomy. *Pathology International* **62**, 295–302 (2012).
10. Arpino, G., Bardou, V. J., Clark, G. M. & Elledge, R. M. Infiltrating lobular carcinoma of the breast: tumor characteristics and clinical outcome. *Breast Cancer Res* **6**, R149–56 (2004).
11. Goldhirsch, a *et al*. Strategies for subtypes--dealing with the diversity of breast cancer: highlights of the St. Gallen International Expert Consensus on the Primary Therapy of Early Breast Cancer 2011. *Annals of Oncology* **22**, 1736–47 (2011).

12. Townson, J. L. & Chambers, A. F. Dormancy of solitary metastatic cells. *Cell Cycle* **5**, 1744–50 (2006).
13. Chambers, A. F., Groom, A. C. & Macdonald, I. C. Dissemination and growth of cancer cells in metastatic sites. *Nat Rev Cancer* **2**, 563–572 (2002).
14. Oppenheimer, S. B. Cellular basis of cancer metastasis : A review of fundamentals and new advances. *Acta Histochemica* **108**, 327–334 (2006).
15. Allan, A. L., Vantyghem, S. A., Tuck, A. B. & Chambers, A. F. Tumor Dormancy and Cancer Stem Cells: Implications for the Biology and Treatment of Breast Cancer Metastasis. *Breast Dis* **26**, 87–98
16. Achen, M. G. & Stacker, S. A. Molecular control of lymphatic metastasis. *Annals-New York Academy of Sciences* **1131**, 225–234 (2008).
17. Eldweny, H. *et al.* Predictors of non-sentinel lymph node metastasis in breast cancer patients with positive sentinel lymph node (Pilot study). *Journal of the Egyptian National Cancer Institute* **24**, 23–30 (2012).
18. Lee, J. *et al.* The usefulness and accuracy of sentiel lymph node biopsy using single photon emission computed tomography/computed tomography with 99mTc phytate to detect locoregional lymph node metastases in patients with papillary thyroid carcinoma. *J Korean Surg Soc* **84**, 195–201 (2013).
19. Pytowski, B. Lymphatic System in the Pathology of Cancer. *Cancer Drug Discovery and Development Antiangiogenic Agents in Cancer Therapy* 225–241 (2008). <<http://www.springerlink.com/index/G423052Q625P3224.pdf>>
20. Rashid, O. M. & Takabe, K. Sentinel Lymph Node Biopsy for Breast Cancer: Our Technique and Future Directions in Lymph Node Staging. *J Nucl Med Radiat Ther* **2012**, (2013).
21. Proulx, S. T. & Detmar, M. Molecular mechanisms and imaging of lymphatic metastasis. *Experimental Cell Research* 1–7 (2013).doi:10.1016/j.yexcr.2013.03.009

22. Blum, K. S. & Pabst, R. Keystones in lymph node development. *Journal of Anatomy* **209**, 585–95 (2006).
23. Katakai, T. *et al.* A novel reticular stromal structure in lymph node cortex: an immuno-platform for interactions among dendritic cells, T cells and B cells. *International Immunology* **16**, 1133–42 (2004).
24. Clement, O. & Luciani, A. Imaging the lymphatic system possibilities and clinical applications. *Eur Radiol* **14**, 1498–1507 (2004).
25. Vantuyghem, S. A. *et al.* A new model for lymphatic metastasis: Development of a variant of the MDA-MB-468 human breast cancer cell line that aggressively metastasizes to lymph nodes. *Clin Exp Metastasis* **22**, 351–361 (2005).
26. Korkaya, H., Liu, S. & Wicha, M. S. Breast cancer stem cells, cytokine networks, and the tumor microenvironment. *J Clin Invest* **121**, 3804–3809 (2011).
27. Orimo, A. *et al.* Stromal fibroblasts present in invasive human breast carcinomas promote tumor growth and angiogenesis through elevated SDF-1/CXCL12 secretion. *Cell* **121**, 335–48 (2005).
28. Schimanski, C. C. *et al.* Dissemination of hepatocellular carcinoma is mediated via chemokine receptor CXCR4. *British Journal of Cancer* **95**, 210–7 (2006).
29. Liersch, R., Hirakawa, S., Berdel, W. E., Mesters, R. M. & Detmar, M. Induced lymphatic sinus hyperplasia in sentinel lymph nodes by VEGF-C as the earliest premetastatic indicator. *International Journal of Oncology* **41**, 2073–8 (2012).
30. Van den Eynden, G. G. *et al.* Induction of lymphangiogenesis in and around axillary lymph node metastases of patients with breast cancer. *British Journal of Cancer* **95**, 1362–6 (2006).
31. Liu, T. *et al.* Tracking Tumor Cells in Lymphatics in a Mice Xenograft. *Mol Imaging* **11**, 451–460 (2012).

32. Jafferbhoy, S. & McWilliams, B. Clinical significance and management of sentinel node micrometastasis in invasive breast cancer. *Clinical Breast Cancer* **12**, 308–12 (2012).
33. Espinosa-Bravo, M. *et al.* Prediction of non-sentinel lymph node metastasis in early breast cancer by assessing total tumoral load in the sentinel lymph node by molecular assay. *European Journal of Surgical Oncology* 4–11 (2013). doi:10.1016/j.ejso.2013.03.011
34. Fiaschi, T. & Chiarugi, P. Oxidative stress, tumor microenvironment, and metabolic reprogramming: a diabolic liaison. *International Journal of Cell Biology* **2012**, 762825 (2012).
35. Hanahan, D. & Coussens, L. M. Accessories to the crime: functions of cells recruited to the tumor microenvironment. *Cancer Cell* **21**, 309–22 (2012).
36. Polyak, K. Heterogeneity in breast cancer. *J Clin Invest* **121**, 3786–3788 (2011).
37. Nguyen, L. V, Vanner, R., Dirks, P. & Eaves, C. J. Cancer stem cells: an evolving concept. *Nat Rev Cancer* **12**, 133–43 (2012).
38. Campbell, L. L. & Polyak, K. Breast Tumor Heterogeneity. *Cell Cycle* **6**, 2332–2338 (2007).
39. Visvader, J. E. & Lindeman, G. J. Cancer stem cells in solid tumours: accumulating evidence and unresolved questions. *Nat Rev Cancer* **8**, 755–68 (2008).
40. Reya, T., Morrison, S. J., Clarke, M. F. & Weissman, I. L. Stem cells, cancer, and cancer stem cells. *Nature* **414**, 105–111 (2001).
41. Moore, N., Houghton, J. & Lyle, S. Slow-cycling therapy-resistant cancer cells. *Stem Cells and Development* **21**, 1822–30 (2012).
42. Fillmore, C. M. & Kuperwasser, C. Human breast cancer cell lines contain stem-like cells that self-renew, give rise to phenotypically diverse progeny and survive chemotherapy. *Breast Cancer Res* **10**, R25 (2008).

43. Xin, H.-W. *et al.* Tumor-Initiating Label-Retaining Cancer Cells in Human Gastrointestinal Cancers Undergo Asymmetric Cell Division. *Stem Cells* **30**, 591–598 (2012).
44. Bragado, P. *et al.* Analysis of marker-defined HNSCC subpopulations reveals a dynamic regulation of tumor initiating properties. *PloS one* **7**, e29974 (2012).
45. Holmgren, L., O'Reilly, M. & Folkman, J. Dormancy of micrometastases: Balanced proliferation and apoptosis in the presence of angiogenesis suppression. *Nature medicine* **1**, 149–153 (1995).
46. Klein, C. a Framework models of tumor dormancy from patient-derived observations. *Current Opinion in Genetics & Development* **21**, 42–9 (2011).
47. Heyn, C. *et al.* In vivo MRI of cancer cell fate at the single-cell level in a mouse model of breast cancer metastasis to the brain. *Magn Reson Med* **56**, 1001–10 (2006).
48. Goss, P. E. & Chambers, A. F. Does tumour dormancy offer a therapeutic target? *Nat Rev Cancer* **10**, 871–7 (2010).
49. Naumov, G. N. *et al.* Persistence of Solitary Mammary Carcinoma Cells in a Secondary Site: A Possible Contributor to Dormancy. *Cancer Res* **62**, 2162–2168 (2002).
50. Almog, N. Molecular mechanisms underlying tumor dormancy. *Cancer Letters* **294**, 139–46 (2010).
51. Luzzi, K. J. *et al.* Multistep nature of metastatic inefficiency: dormancy of solitary cells after successful extravasation and limited survival of early micrometastases. *Am J Pathol* **153**, 865–73 (1998).
52. Townson, J. L. *et al.* Three-dimensional imaging and quantification of both solitary cells and metastases in whole mouse liver by magnetic resonance imaging. *Cancer Res* **69**, 8326–31 (2009).

53. Cameron, M. D. *et al.* Temporal Progression of Metastasis in Lung: Cell Survival, Dormancy, and Location Dependence of Metastatic Inefficiency. *Cancer Res* **60**, 2541–2546 (2000).
54. Uhr, J. W. & Pantel, K. Controversies in clinical cancer dormancy. *Proc Natl Acad Sci U S A* **108**, 12396–12400 (2011).
55. Folkman, J. & Kalluri, R. Cancer without disease. *Nature* **427**, 787 (2004).
56. Barkan, D. *et al.* Metastatic Growth from Dormant Cells Induced by a Col-I Enriched Fibrotic Environment. *Cancer Res* **70**, 5706–5716 (2010).
57. Ranganathan, A. C., Zhang, L., Adam, A. P. & Aguirre-ghiso, J. A. Functional Coupling of p38-Induced Up-regulation of BiP and Activation of RNA-Dependent Protein Kinase-Like Endoplasmic Reticulum Kinase to Drug Resistance of Dormant Carcinoma Cells. *Cancer Res* **66**, 1702–1711 (2006).
58. Moore, N. & Lyle, S. Quiescent, slow-cycling stem cell populations in cancer: a review of the evidence and discussion of significance. *Journal of Oncology* **2011**, (2011).
59. Bonnet, D. & Dick, J. E. Human acute myeloid leukemia is organized as a hierarchy that originates from a primitive hematopoietic cell. *Nature Medicine* **3**, 730–737 (1997).
60. Al-Hajj, M., Wicha, M. S., Benito-Hernandez, A., Morrison, S. J. & Clarke, M. F. Prospective identification of tumorigenic breast cancer cells. *Proc Natl Acad Sci U S A* **100**, 3983–8 (2003).
61. Fang, D. D. *et al.* Expansion of CD133(+) colon cancer cultures retaining stem cell properties to enable cancer stem cell target discovery. *British Journal of Cancer* **102**, 1265–75 (2010).
62. Tirino, V. *et al.* The role of CD133 in the identification and characterisation of tumour-initiating cells in non-small-cell lung cancer. *European Journal of Cardio-thoracic Surgery* **36**, 446–53 (2009).

63. Reyes, E. E., Kunovac, S. K., Duggan, R., Kregel, S. & Griend, D. J. Vander Growth kinetics of CD133-positive prostate cancer cells. *The Prostate* (2012). doi:10.1002/pros.22616
64. Zhou, X.-D. *et al.* Detection of cancer stem cells from the C6 glioma cell line. *The Journal of International Medical Research* **37**, 503–10 (2009).
65. Oka, N., Soeda, A., Noda, S. & Iwama, T. Brain tumor stem cells from an adenoid glioblastoma multiforme. *Neurologia Medico-chirurgica* **49**, 146–50; discussion 150–1 (2009).
66. Croker, A. K. *et al.* High aldehyde dehydrogenase and expression of cancer stem cell markers selects for breast cancer cells with enhanced malignant and metastatic ability. *Journal of Cellular and Molecular Medicine* **13**, 2236–52 (2009).
67. Cariati, M. *et al.* Alpha-6 integrin is necessary for the tumourigenicity of a stem cell-like subpopulation within the MCF7 breast cancer cell line. *International Journal of Cancer* **122**, 298–304 (2008).
68. Meyer, M. J. *et al.* CD44posCD49fhiCD133/2hi defines xenograft-initiating cells in estrogen receptor-negative breast cancer. *Cancer Res* **70**, 4624–33 (2010).
69. Gazdzinski, L. M. & Nieman, B. J. Cellular imaging and texture analysis distinguish differences in cellular dynamics in mouse brain tumors. *Magn Reson Med* (2013). doi:10.1002/mrm.24790
70. Rajasekhar, V. K. V. Analytical methods for cancer stem cells. *Methods in Molecular Biology (Clifton, N.J.)* **407**, 83–95 (2007).
71. Chen, K., Huang, Y.-H. & Chen, J.-L. Understanding and targeting cancer stem cells: therapeutic implications and challenges. *Acta Pharmacologica Sinica* **34**, 732–740 (2013).
72. Hiraga, T., Ito, S. & Nakamura, H. Cancer Stem-like Cell Marker CD44 Promotes Bone Metastases by Enhancing Tumorigenicity, Cell Motility and Hyaluronan Production. *Cancer Res* (2013). doi:10.1158/0008-5472.CAN-12-3801

73. Mani, S. a *et al.* The epithelial-mesenchymal transition generates cells with properties of stem cells. *Cell* **133**, 704–15 (2008).
74. Monteiro, J. & Fodde, R. Cancer stemness and metastasis: therapeutic consequences and perspectives. *European Journal of Cancer* **46**, 1198–203 (2010).
75. Brown, M. A. & Semelka, R. C. *MRI: Basic Principles and Applications*. (John Wiley & Sons: Hoboken, 2003).
76. McRobbie, D. W., Moore, E. A., Graves, M. J. & Prince, M. R. *MRI: From Picture to Proton*. (Cambridge University Press: New York, 2007).
77. Kuperman, V. *Magnetic Resonance Imaging: Physical Principles and Applications*. (Academic Press: San Diego, 2000).
78. Nitz, W. R. & Reimer, P. Contrast mechanisms in MR imaging. **9**, 1032–1046 (1999).
79. Markl, M. & Leupold, J. Gradient echo imaging. *J Magn Reson Imaging* **35**, 1274–89 (2012).
80. Scheffler, K. & Lehnhardt, S. Principles and applications of balanced SSFP techniques. *European Radiology* **13**, 2409–18 (2003).
81. Miller, K. L. FMRI using balanced steady-state free precession (SSFP). *NeuroImage* **62**, 713–9 (2012).
82. Bhosale, P., Ma, J. & Choi, H. Utility of the FIESTA pulse sequence in body oncologic imaging: review. *AJR* **192**, S83–93 (Quiz S94–7) (2009).
83. Modo, M., Hoehn, M. & Bulte, J. W. M. Cellular MR Imaging. *Mol Imaging* **04**, 143–164 (2005).
84. Bulte, J. W. M. & Kraitchman, D. L. Iron oxide MR contrast agents for molecular and cellular imaging. *NMR Biomed.* **17**, 484–499 (2004).

85. Shapiro, E. M. & Koretsky, A. P. Micro-Sized Iron Oxide Particles (MPIOs) for Cellular Imaging: More Bang for the Buck. *Nanoparticles in Biomedical Imaging: Emerging Technologies and Applications* 141–161 (2008).
86. Magnitsky, S., Roesch, A., Herlyn, M. & Glickson, J. D. In vivo and ex vivo MR imaging of slowly cycling melanoma cells. *Magn Reson Med* **66**, 1362-1373 (2011).
87. Arbab, A. S. *et al.* Labeling of cells with ferumoxides-protamine sulfate complexes does not inhibit function or differentiation capacity of hematopoietic or mesenchymal stem cells. *NMR Biomed* **18**, 553–9 (2005).
88. Tang, T. Y. *et al.* The ATHEROMA (Atorvastatin Therapy: Effects on Reduction of Macrophage Activity) Study. Evaluation using ultrasmall superparamagnetic iron oxide-enhanced magnetic resonance imaging in carotid disease. *Journal of the American College of Cardiology* **53**, 2039–50 (2009).
89. Tourdias, T. *et al.* Assessment of Disease Activity in Multiple Sclerosis Phenotypes with Combined Gadolinium-and Superparamagnetic Iron Oxide-enhanced MR Imaging. *Radiology* **264**, 225–233 (2012).
90. Henning, T. D. *et al.* Magnetic Resonance Imaging of Ferumoxide-labeled Mesenchymal Stem Cells in Cartilage Defects: In Vitro and In Vivo Investigations. *Mol Imaging* **11**, 1–8 (2013).
91. Kim, H., Walczak, P., Muja, N., Campanelli, J. T. & Bulte, J. W. M. ICV-transplanted human glial precursor cells are short-lived yet exert immunomodulatory effects in mice with EAE. *Glia* **60**, 1117–29 (2012).
92. Chaumeil, M. M. *et al.* Longitudinal evaluation of MPIO-labeled stem cell biodistribution in glioblastoma using high resolution and contrast-enhanced MR imaging at 14.1 tesla. *Neuro-oncology* **14**, 1050–61 (2012).
93. Gonzalez-Lara, L. E. *et al.* The use of cellular magnetic resonance imaging to track the fate of iron-labeled multipotent stromal cells after direct transplantation in a mouse model of spinal cord injury. *Mol Imaging Biol* **13**, 702–11 (2011).

94. Chapon, C. *et al.* An in vivo multimodal imaging study using MRI and PET of stem cell transplantation after myocardial infarction in rats. *Mol Imaging Biol* **11**, 31–8 (2009).
95. Yang, K. *et al.* Magnetic resonance evaluation of transplanted mesenchymal stem cells after myocardial infarction in swine. *Can J Cardiol* **27**, 818–25 (2011).
96. Daadi, M. M. *et al.* Molecular and magnetic resonance imaging of human embryonic stem cell-derived neural stem cell grafts in ischemic rat brain. *Mol Ther* **17**, 1282–91 (2009).
97. Jendelová, P. *et al.* Magnetic resonance tracking of transplanted bone marrow and embryonic stem cells labeled by iron oxide nanoparticles in rat brain and spinal cord. *J Neurosci Res* **76**, 232–43 (2004).
98. Herynek, V. *et al.* Improved detection of pancreatic islets in vivo using double contrast. *Contrast Media Mol Imaging* **6**, 308–13 (2011).
99. Jung, M. J. *et al.* MRI of transplanted surface-labeled pancreatic islets with heparinized superparamagnetic iron oxide nanoparticles. *Biomaterials* **32**, 9391–400 (2011).
100. Kriz, J., Jirak, D., White, D. & Foster, P. Magnetic Resonance Imaging of Pancreatic Islets Transplanted Into the Right Liver Lobes of Diabetic Mice. *Transplantation Proceedings* **40**, 444–448 (2008).
101. Jirak, D. *et al.* Monitoring the survival of islet transplants by MRI using a novel technique for their automated detection and quantification. *Magma* **22**, 257–65 (2009).
102. Medarova, Z. *et al.* In vivo imaging of autologous islet grafts in the liver and under the kidney capsule in non-human primates. *Transplantation* **87**, 1659–1666 (2009).
103. Baeten, K. *et al.* Tracking of myelin-reactive T cells in experimental autoimmune encephalomyelitis (EAE) animals using small particles of iron oxide and MRI. *NMR Biomed* **23**, 601–9 (2010).

104. Ahrens, E. T., Feili-Hariri, M., Xu, H., Genove, G. & Morel, P. a Receptor-mediated endocytosis of iron-oxide particles provides efficient labeling of dendritic cells for in vivo MR imaging. *Magn Reson Med* **49**, 1006–13 (2003).
105. Dekaban, G. A. *et al.* Semiquantitation of Mouse Dendritic Cell Migration In Vivo Using Cellular MRI. *J Immunother* **32**, 240–251 (2009).
106. Zhang, X. *et al.* Cellular magnetic resonance imaging of monocyte-derived dendritic cell migration from healthy donors and cancer patients as assessed in a scid mouse model. *Cytotherapy* **13**, 1234–1248 (2011).
107. Baumjohann, D. *et al.* In vivo magnetic resonance imaging of dendritic cell migration into the draining lymph nodes of mice. *European Journal of Immunology* **36**, 2544–55 (2006).
108. Joo, H. J. *et al.* Detection of prostaglandin E2-induced dendritic cell migration into the lymph nodes of mice using a 1.5 T clinical MR scanner. *NMR Biomed* **25**, 570–9 (2012).
109. Ferguson, P. M., Slocombe, A., Tilley, R. D. & Hermans, I. F. Using magnetic resonance imaging to evaluate dendritic cell-based vaccination. *PloS one* **8**, e65318 (2013).
110. Heyn, C., Bowen, C. V, Rutt, B. K. & Foster, P. J. Detection Threshold of Single SPIO-Labeled Cells With FIESTA. *Magn Reson Med* **53**, 312–320 (2005).
111. Rad, A. M., Arbab, A. S., Iskander, a S. M., Jiang, Q. & Soltanian-Zadeh, H. Quantification of superparamagnetic iron oxide (SPIO)-labeled cells using MRI. *J Magn Reson Imaging* **26**, 366–74 (2007).
112. Liu, W. & Frank, J. A. Detection and quantification of magnetically labeled cells by cellular MRI. *European Journal of Radiology* **70**, 258–64 (2009).
113. Wu, C. Y. *et al.* MR imaging of human pancreatic cancer xenograft labeled with superparamagnetic iron oxide in nude mice. *Contrast Media Mol Imaging* **7**, 51–8 (2012).

114. Kosaka, N., Bernardo, M., Mitsunaga, M., Choyke, P. L. & Kobayashi, H. MR and optical imaging of early micrometastases in lymph nodes: triple labeling with nano-sized agents yielding distinct signals. *Contrast Media Mol Imaging* **7**, 247–53 (2012).
115. Foster, P., Dunn, E., Karl, K., Snir, J. & CM Cellular magnetic resonance imaging: in vivo imaging of melanoma cells in lymph nodes of mice. *Neoplasia* **10**, 207–216 (2008).
116. Bulte, J. W. M. In Vivo MRI Cell Tracking: Clinical Studies. *American Journal of Radiology* **193**, 314–325 (2009).
117. McColgan, P., Sharma, P. & Bentley, P. Stem cell tracking in human trials: a meta-regression. *Stem Cell Reviews* **7**, 1031–40 (2011).
118. Zhu, J., Zhou, L. & XingWu, F. Tracking neural stem cells in patients with brain trauma. *The New England Journal of Medicine* **355**, 2376–8 (2006).
119. Callera, F. & De Melo, C. M. T. P. Magnetic resonance tracking of magnetically labeled autologous bone marrow CD34+ cells transplanted into the spinal cord via lumbar puncture technique in patients with chronic spinal cord injury: CD34+ cells' migration into the injured site. *Stem Cells and Development* **16**, 461–6 (2007).
120. Karussis, D. *et al.* Safety and Immunological Effects of Mesenchymal Stem Cell Transplantation in Patients With Multiple Sclerosis and Amyotrophic Lateral Sclerosis. *Arch Neurol* **67**, 1187–1194 (2010).
121. Saudek, F. *et al.* Magnetic Resonance Imaging of Pancreatic Islets Transplanted Into the Liver in Humans. *Transplantation* **90**, 1602–1606 (2010).
122. Toso, C. *et al.* Clinical magnetic resonance imaging of pancreatic islet grafts after iron nanoparticle labeling. *American Journal of Transplantation* **8**, 701–6 (2008).
123. De Vries, I. *et al.* Magnetic resonance tracking of dendritic cells in melanoma patients for monitoring of cellular therapy. *Nat biotechnol* **23**, 1407–1413 (2005).
124. Faraheme - Prescribing Information. 1–4 (2011).

125. Bashir, M. R., Jaffe, T. a, Brennan, T. V, Patel, U. D. & Ellis, M. J. Renal Transplant Imaging Using Magnetic Resonance Angiography With a Nonnephrotoxic Contrast Agent. *Transplantation* **96**, 1–6 (2013).
126. Khurana, A. *et al.* Ferumoxytol: a new, clinically applicable label for stem-cell tracking in arthritic joints with MRI. *Nanomedicine* (2012). doi:10.2217/NNM.12.198
127. Varallyay, C. G. *et al.* High-resolution steady-state cerebral blood volume maps in patients with central nervous system neoplasms using ferumoxytol, a superparamagnetic iron oxide nanoparticle. *Journal of Cerebral Blood Flow and Metabolism* **33**, 780–6 (2013).

Chapter 2

2 Comparison of Lymph Nodes and Spleen in Immune Compromised and Wild-Type Mice*

2.1 Introduction

Immuno-deficient mice are routinely used in research. These mice have a limited capacity for rejecting foreign tissue, which makes them excellent recipients for xenografts of human cells and tissues.¹ A variety of genetic mutations are known that impair immune function in mice. Genetic loci affecting immune responses include nu (nude), SCID (severe combined immunodeficiency), beige, and xid (X-linked immunodeficiency).² The various mouse mutants have differing immunological properties. The extent to which some of these mutations interfere with immune function can also vary with the genetic background.

Some commonly used strains of immuno-deficient mice include the nude mouse, the severe combined immune deficiency (SCID) mouse and the NOD/SCID mouse (non-obese diabetic/SCID). The murine recessive nude mutation on chromosome 11 arose spontaneously.² Homozygotes (nu/nu) are hairless from birth and completely lack a thymus due to a failure of development of the thymic cells at the embryonic stage.^{2,3} The lack of the thymus leads to many defects of the immune system, including a greatly reduced population of T lymphocytes.

The murine recessive SCID mutation on chromosome 16 arose in the CB-17 inbred strain (BALB/c.C57BL/Ka-Igh-1b). Homozygotes lack both B and T cells but have normal numbers of natural killer (NK) cells, the main effectors of non-MHC restricted immunity.² In 1995, Shultz et al. described a new immuno-deficient mouse model, the NOD/SCID, obtained by crossing the SCID and NOD mouse strains.⁴ The NOD strain is characterized by

* This work has been previously published and is reproduced here under a Creative Commons Attribution 3.0 Unported License. Paper is published as Economopoulos V, Noad JC, Krishnamoorthy S, Rutt BK, Foster PJ (2011) *Comparing the MRI Appearance of the Lymph Nodes and Spleen in Wild-Type and Immuno-Deficient Mouse Strains*. PLoS ONE 6(11): e27508.

functional deficits in NK cells, an absence of circulating complement and defects in the differentiation and function of antigen-presenting cells.⁵ The NOD/SCID model combines multiple functional defects of adaptive and innate immunity. They are very suitable for xenografts of human cell lines.

The NOD/SCID IL2R γ null (NOG) mouse is a relatively new immuno-deficient mouse established in an attempt to generate a more appropriate recipient for xenotransplantation. NOG mice are NOD/SCID mice that have an additional mutation in the common gamma chain of the IL2 receptor (IL2R γ).⁶ In addition to lacking functional T and B lymphocytes, the IL2R γ deficiency blocks the development of NK cells. The NOG mice have no 'leakiness' with age, meaning that NK cells are not ever produced. The NOG mouse accepts heterologous cells much more easily compared with any other type of immuno-deficient mouse. Thus, the NOG mouse is currently viewed as the most sensitive mouse model to allow human cells to engraft, proliferate, and/or differentiate.⁷

The nude mouse has been widely studied in cancer research.^{8,9} Xenografts of many different established human cancer cell lines have been successfully grown in nude mice after their implantation in subcutaneous or orthotopic sites.^{10,11} However, the engraftment and growth rates, and the incidence of metastases, are often enhanced in the other more immuno-deficient mouse strains.^{1,2,12-14} A comparative study of tumor growth in various cancer cell lines in different mouse strains (nude, C.B.-17 SCID (SCID) and NOD/SCID mice) has shown a better growth rate in the NOD/SCID mouse.¹ Taghian et al. compared the transplantability of six human cancer cell lines in nude and SCID mice. For 6/6 cell lines, the number of cells required to establish a tumor was significantly lower for SCID mice compared to nude mice.¹⁵ Xie et al. showed that nude and SCID mice were equally suitable for growing three different human cancer cell lines (bladder, breast and melanoma), but that the metastatic capacity of the cells was much better expressed in the SCID mice.¹⁴

Magnetic resonance imaging (MRI) is becoming increasingly common as a tool for the noninvasive monitoring of disease in a wide range of murine models. Therefore, it is important to understand the baseline MRI appearance of the lymph nodes and spleen in experimental mice. Three strains of immune-compromised mice were chosen (nude, SCID and NOG) because of their frequent use as experimental models in research. Because of the

altered structure and function in the lymphoid organs (spleen, lymph nodes) in immuno-deficient mice we hypothesized that there would be noteworthy differences in the normal MRI appearance of the lymph nodes and spleen in immuno-deficient mice compared to immuno-competent mice. In the current study we use MRI to characterize the lymph nodes and spleen in three different immuno-deficient mice (nude, SCID and NOG) and the immune-competent mouse strain C57Bl/6.

2.2 Materials and Methods

All animal experiments were approved by the Animal Use Subcommittee of the University Council on Animal Care at The University of Western Ontario following the guidelines of the Canadian Council on Animal Care (protocol # 2010-210).

2.2.1 Mice

Mice used included the wild-type C57Bl/6J mice (Jackson Laboratories, age 7 to 9 weeks at arrival) and immuno-deficient nude (nu/nu) mice (Charles River Canada, age 6 to 8 weeks at arrival), CB-17 SCID (CB17/Icr-Prkdc^{scid}/IcrIcoCr1) mice (Charles River Canada, age 6 to 8 weeks at arrival) and NOG mice (Jackson Laboratories, age 8 to 11 weeks at arrival). In the first experiment 4 mice per strain were imaged once, within a week of arrival, to compare the MRI appearance of the lymphoid organs. In the second experiment 4 mice per strain (excluding the NOG mice, which the first experiment revealed had no MR visible nodes) were imaged on days 7, 14 and 28 after arrival to assess changes in the appearance of the nodes and spleens over time. The immuno-deficient mice used in this longitudinal imaging experiment left the barrier proper for the first scanning session and returned to an external barrier where they were housed in safe conditions within ventilated cages for the remainder of the study. All animals were sacrificed after the final imaging time point and the tissues of interest were weighed and prepared for histology.

2.2.2 Magnetic Resonance Imaging

All imaging was performed on a 1.5T CV/I MRI scanner (General Electric Medical Systems, Milwaukee, WI) using a custom built gradient coil insert (inner diameter = 17.5cm, maximum gradient strength = 500 mT/m, and peak slew rate = 3000 T/m/sec) and a custom built solenoid mouse body radio-frequency (RF) coil (4cm in length and 3cm in diameter). All mice were imaged with a 3D balanced steady state free precession (bSSFP) pulse sequence. The bSSFP sequence was chosen because it provides very high SNR efficiency, allowing for high resolution image acquisitions of the whole mouse body in reasonable scan times, and because it produces very good soft tissue contrast, related to T2/T1. The scan parameters for bSSFP were as follows: repetition time = 6.7 ms, echo time = 3.3 ms, flip angle = 40°, bandwidth = +/- 31.25 kHz, matrix = 300x300, field of view (FOV) = 6 cm, 0.2 mm slice thickness, 200 μ m isotropic spatial resolution, 4 signal averages (NEX), 4 RF phase cycles and scan time of 34 minutes.

Since both fat and fluid appear with high signal intensity in bSSFP images, spin echo (SE) images were acquired with T1- and T2-weighting in some nude mice. These additional image contrasts helped with the interpretation of the hyperintense regions within some lymph nodes on bSSFP images. The SE parameters were as follows: repetition time = 2000 ms for T2w and 600ms for T1w, echo time = 80ms for T2w and 25ms for T1w, matrix = 256x256, FOV = 6 cm FOV, in-plane spatial resolution = 234 microns, slice thickness = 500 microns, 12 NEX, scan time = ~ 15 minutes for T1w and ~ 51 minutes for T2w images.

2.2.3 Image Analysis

The volume of the spleen and the left and right axillary, brachial, inguinal and popliteal lymph nodes were measured by manual segmentation from all of the acquired images. The axillary, brachial, inguinal and popliteal lymph nodes were chosen for comparison since they are easily visualized and are commonly investigated in metastasis and immunotherapy experiments. The Osirix image analysis software¹⁶ was used to make all measurements from images acquired in this study. Each organ of interest was segmented individually on every image slice to create a series of regions of interest (ROI). One ROI from the organ's ROI

series was selected and the volume was calculated by using the ROI volume calculation tool available within the software package. This procedure was repeated to calculate the volume for all organs in each image. All volume data were compared statistically using Graph Pad Prism analysis software (GraphPad Software, La Jolla, CA).

2.2.4 Histopathological Analysis

All animals were euthanized using a carbon dioxide gas chamber. Lymph nodes were then removed and placed in 3.75 % formalin. The fixed lymph nodes were imbedded into paraffin blocks and sectioned. Four 5- μ m sections were cut from each block, followed by a 1- μ m gap and an additional four 5- μ m sections. The sections were then stained with Hematoxylin and Eosin (H&E).

2.3 Results

2.3.1 Lymph Node Appearance and Volumes

In the first set of studies, C57Bl/6, SCID, nude and NOG mice were imaged once. Figure 2.1 shows coronal views of the whole mouse body and the locations of the axillary, brachial, inguinal and popliteal lymph nodes in bSSFP images of a C57Bl/6 mouse. The images of lymph nodes in the C57Bl/6 mice appear with uniform signal intensity and have good contrast with the surrounding tissue for the brachial, inguinal and popliteal lymph nodes, which are located in fat pads.

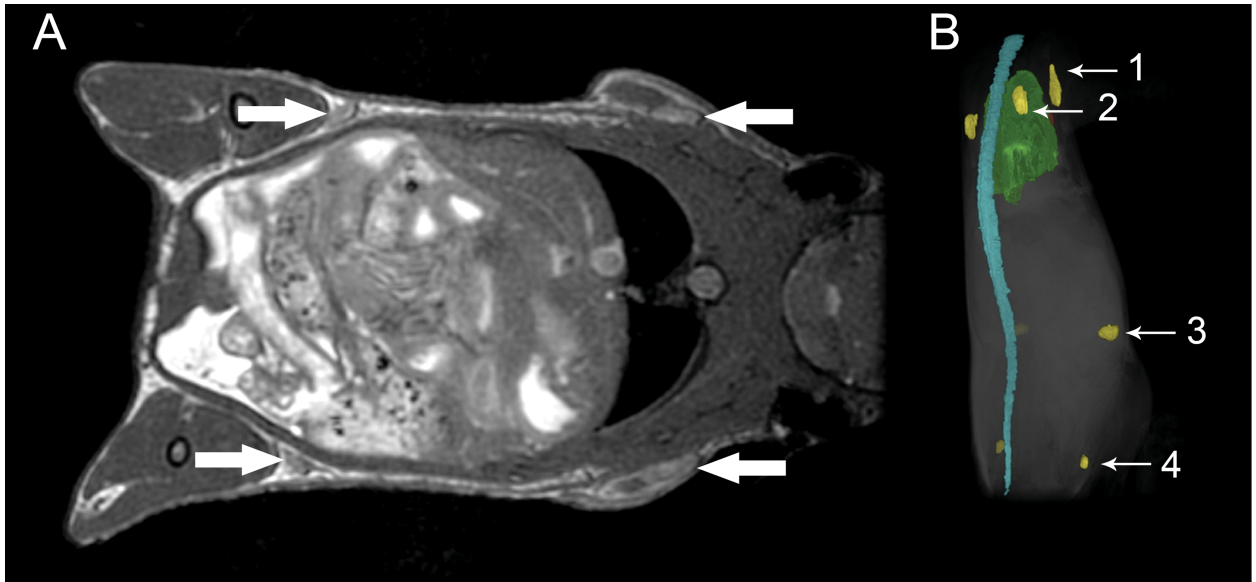


Figure 2.1 - (A) Whole mouse body bSSFP image of a C57Bl/6 mouse showing both the brachial and inguinal lymph nodes (arrows) and (B) 3D reconstruction showing the location of various lymph nodes within the mouse; 1 – axillary node, 2 – brachial node, 3 – inguinal node, 4 – popliteal node.

Representative images of these nodes in the different mouse strains are shown in Figure 2.2A. There were some notable differences in the MRI appearance of the lymph nodes in the immune compromised mice. First, in images of some of the lymph nodes in the nude mice a large hyperintense region was visible within the node. This was observed in the axillary (5/8 nodes), brachial (8/8 nodes) and inguinal nodes (6/8 nodes). While the brachial nodes most frequently exhibited these hyperintense areas, these areas were anatomically the most obvious in the axillary nodes. This pattern of hyperintensity was also present in some nodes in SCID mice, but at a lower frequency; in the brachial (3/8 nodes), inguinal (1/8 nodes) and popliteal (2/8 nodes) nodes. Bright spots were never observed in C57Bl/6 mice. No lymph nodes were visible in the images of the NOG mice.

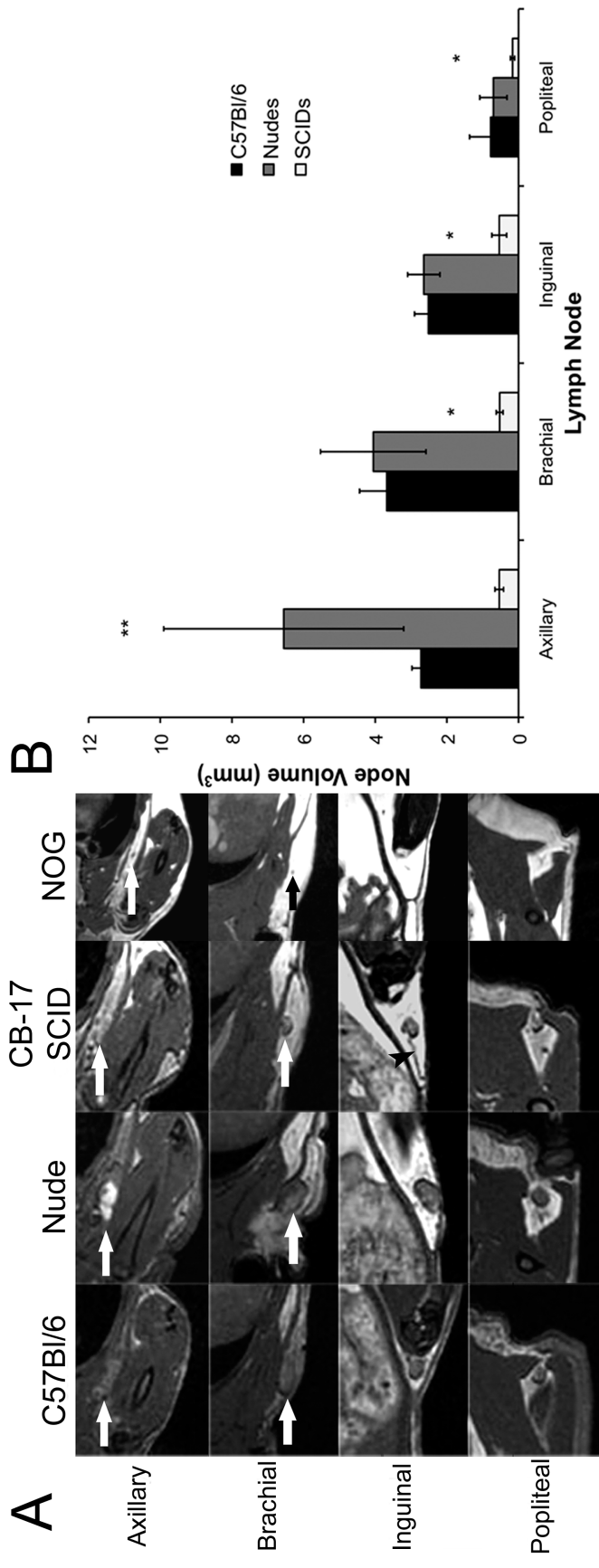


Figure 2.2 (previous page) - MR appearance and volumes of lymph nodes various mouse strains. (A) MR appearance of the axillary, brachial, inguinal and popliteal lymph nodes in C57Bl/6, Nude, CB-17 SCID and NOG mice. The brachial, inguinal and popliteal lymph nodes are easiest to visualize due to their location within a fat pad. Lymphatic vessels are also visible in acquired images (arrowhead). Images for the NOG mice are included for completeness although there were no MRI detectable lymph nodes. (B) Volumes of the axillary, brachial, inguinal and popliteal lymph nodes in C57Bl/6, Nude and CB-17 SCID mice. The brachial, inguinal and popliteal lymph nodes in CB-17 SCID mice were found to be significantly smaller than those in both C57Bl/6 and Nude mice (*, $p < 0.0001$ for brachial and inguinal and $p = 0.0128$ for popliteal). The axillary node in Nude mice was significantly larger than those in both CB-17 SCID and C57Bl/6 mice (, $p < 0.0001$). One way ANOVA test was used. Error bars represent the standard deviation.**

Measuring the lymph node volumes from the 3D MR images also revealed differences between mouse strains (Figure 2.2B). The mean lymph node volumes measured from images acquired in the first experiment are listed in Table 2.1. All volumes are listed as the mean +/- standard deviation of the mean. The mean values were compared using a one way Analysis of Variance (ANOVA) test with a Tukey multiple comparison posttest. The brachial, inguinal and popliteal nodes in SCID mice were significantly smaller than those in both nude mice and C57Bl/6 mice ($p < 0.0001$ for brachial and inguinal and $p = 0.0128$ for popliteal). The axillary nodes in nude mice were significantly larger than those in C57Bl/6 mice ($p < 0.0001$), while the brachial, inguinal and popliteal node volumes were comparable between these two strains. The size of all lymph nodes was most variable in the nude mouse.

Table 2.1 - Lymph node volumes of C57Bl/6, Nude and CB-17 SCID mice. All volumes listed as mean \pm standard deviation.

Lymph Node	C57Bl/6J	Nude	CB-17 SCID
Axillary Node Volume (mm ³)	2.73 \pm 0.25	6.55 \pm 3.35	0.54 \pm 0.12
Brachial Node Volume (mm ³)	3.68 \pm 0.76	4.06 \pm 1.47	0.53 \pm 0.09
Inguinal Node Volume (mm ³)	2.52 \pm 0.39	2.65 \pm 0.45	0.54 \pm 0.21
Popliteal Node Volume (mm ³)	0.78 \pm 0.59	0.70 \pm 0.38	0.17 \pm 0.06

Examination of the H&E staining revealed clear differences in the morphology of nodes from the different mouse strains (Figure 2.3). In the immune competent C57Bl/6 mice, the nodes contain all the major structures including the cortex, paracortex and medulla. Areas rich in T and B cells are present and fully formed in this strain. Lymph nodes from nude mice have a similar structure; the B cell follicles can easily be distinguished from other structures in the node. However, T cells are lacking in these animals, leaving vacant areas within the paracortex. SCID mouse lymph nodes do not contain any defined structures. The cortex, paracortex and medulla cannot easily be distinguished.

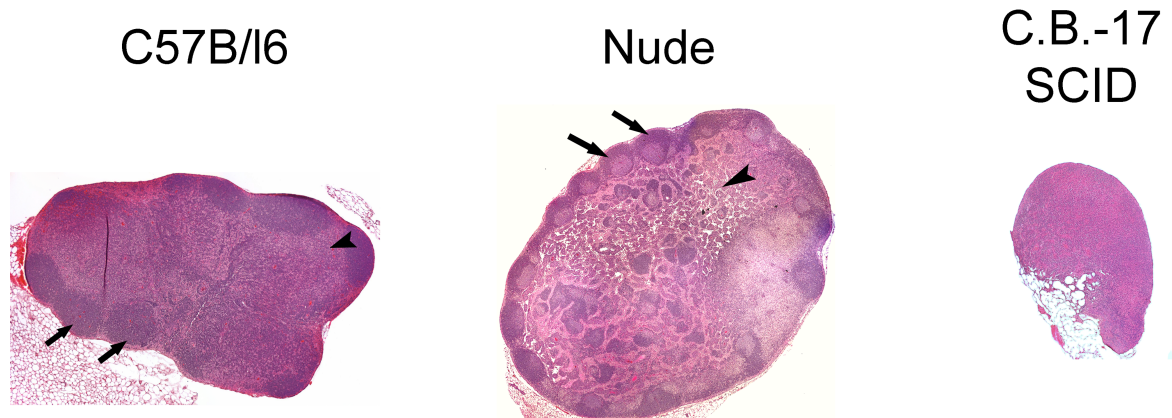


Figure 2.3 - H&E sections of brachial lymph nodes from C57B/16, Nude and C.B.-17 SCID mice. Whole nodes are shown at 5x magnification. The T-cell rich paracortex (arrowheads) and B-cell rich follicles (arrows) can be easily seen in the nodes of C57B/16 mice, where as in Nude mouse lymph nodes, only the B-cell rich follicles can be seen (arrows). In the areas of the paracortex where T cells should be found, vacant areas are detected (arrowheads), helping to explain the hyperintense appearance of many of these nodes in MR images. Nodes in SCID mice lack both the paracortex and follicles, leaving these nodes underdeveloped and significantly smaller in size.

In some nodes the cavities in the lymph nodes were pronounced. In Figure 2.4 an H&E stained section of a representative axillary node from a nude mouse is shown along with the corresponding bSSFP image that shows a large region of bright signal within the node. In the T1w images, the central portion of the lymph node had low signal intensity while in the corresponding T2w image the central portion of the node was hyperintense, as in the bSSFP image (Figure 2.5). Lymph node tissue in NOG mice could not be found upon dissection.



Figure 2.4 - MR image (bSSFP) of a nude mouse axillary node with hyperintense center (A) with corresponding histology (B). The hyperintense area within the lymph node (arrow) corresponds to a cavity that is visible in the histology. The section in (B) is rotated relative to the image in (A).

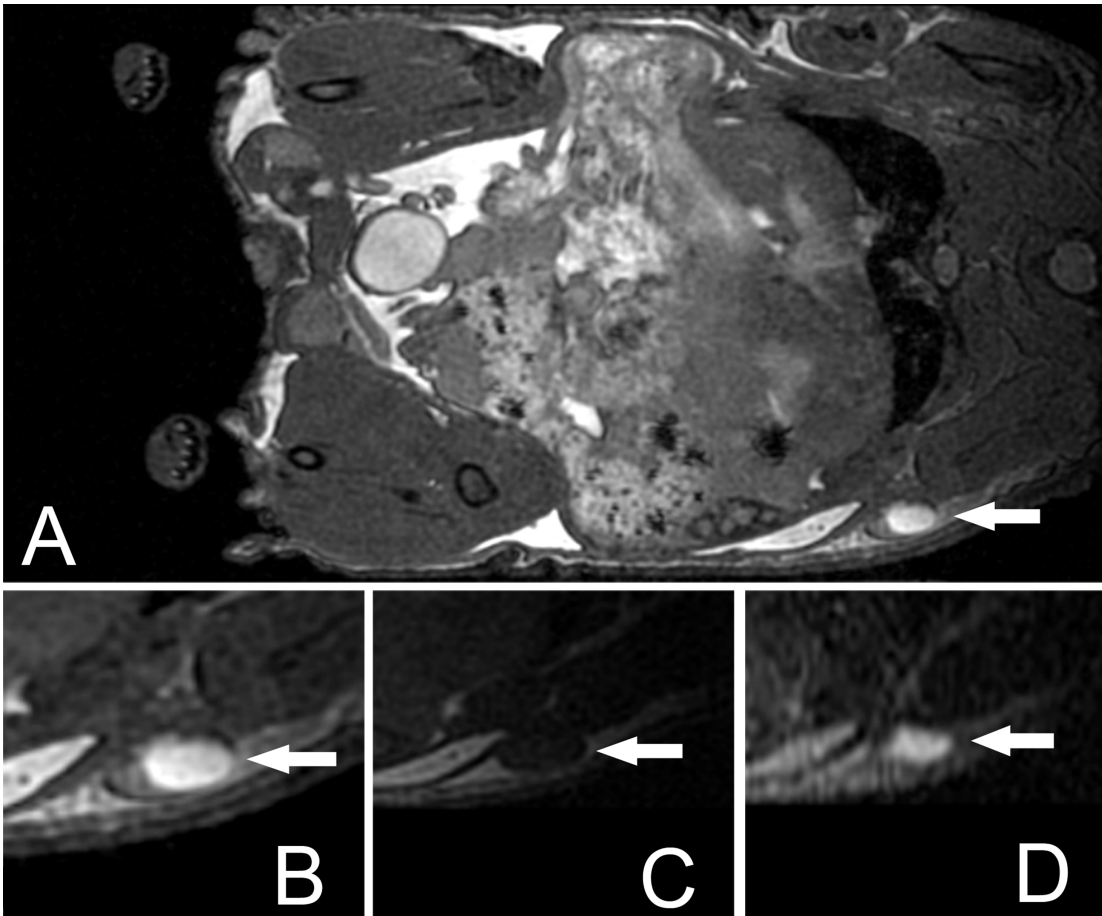


Figure 2.5 - MR images of a nude mouse brachial lymph node acquired with different pulse sequences. (A) bSSFP image of whole mouse body, (B) bSSFP image of lymph node, (C) T1w SE of lymph node (TR = 600 ms, TE = 25 ms), (D) T2w SE of lymph node (TR = 2000 ms, TE = 80 ms)

2.3.2 Spleen Appearance and Volumes

Differences in the MR appearance of the spleen were also observed. The images of the spleen in the C57Bl/6 and nude mice were similar in appearance with a heterogeneous pattern of signal intensities giving it a mottled appearance (Figure 2.6). The images of the spleen in SCID and NOG mice were visually different. The spleens in SCID mice had a higher signal intensity, which was uniform throughout (Figure 2.6C). The spleens in NOG mice appeared with very low signal intensity, appearing black (Figure 2.6D). The spleen volumes were compared using a one way ANOVA with a Tukey multiple comparison posttest and the

average volume of the spleen was found to be significantly smaller ($p < 0.0001$) in both SCID ($23.2 \pm 3.6 \text{ mm}^3$) and NOG ($15.5 \pm 1.3 \text{ mm}^3$) mice compared to the both nude ($72.9 \pm 1.4 \text{ mm}^3$) and C57Bl/6 ($71.1 \pm 1.6 \text{ mm}^3$) strains (Figure 2.6E).

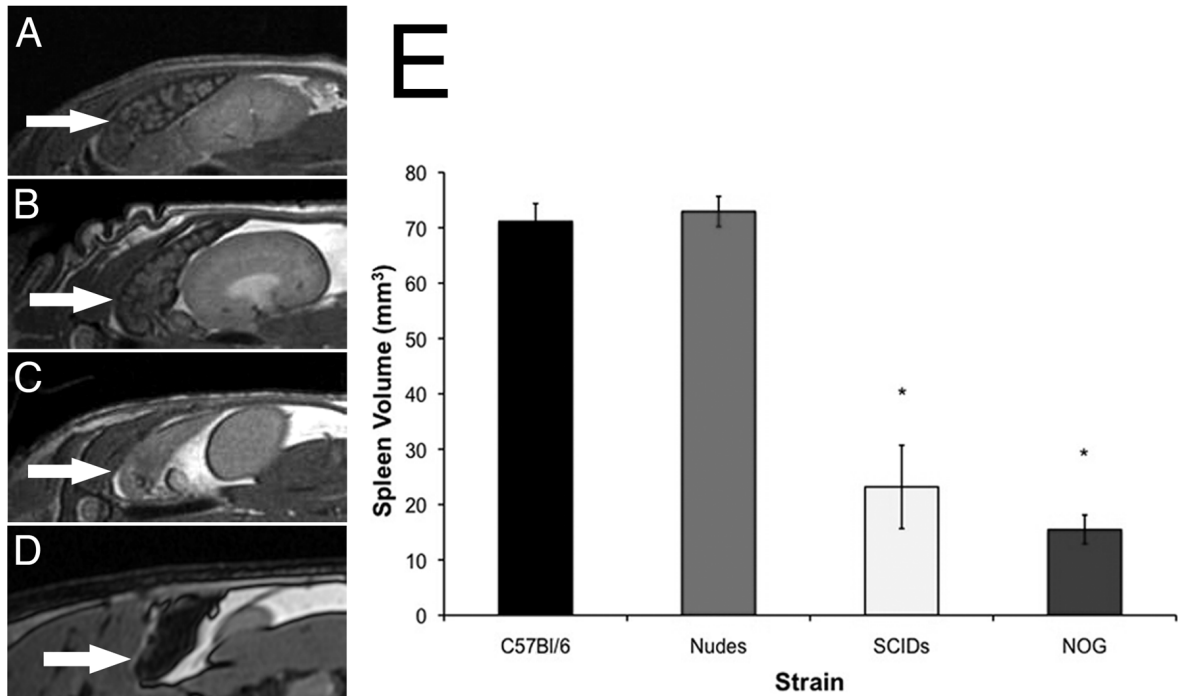


Figure 2.6 - bSSFP images of the spleen in (A) C57Bl/6, (B) nude, (C) CB-17 SCID and (D) NOG. (E) Spleen volume in C57Bl/6, Nude, CB-17 SCID and NOG mice. (*) Spleen volumes were significantly smaller in CB-17 SCID and NOG mice ($p < 0.0001$) compared to C57Bl/6 and nude mice. One way ANOVA test was used. Error bars represent the standard deviation.

2.3.3 Changes in Lymph Node Volumes Over Time

We next wanted to determine whether there were changes in the MR appearance of lymph nodes over time. C57Bl/6, nude and SCID mice were imaged on days 7, 14 and 28 after arrival. The lymph node volumes were measured from images acquired at each time point (Figure 2.7). The lymph node volumes were compared over time using a repeated measures

ANOVA test with a Tukey multiple comparison posttest. In all mice there were changes in the lymph node volumes over time. In the C57Bl/6 mice the inguinal node decreased in volume significantly between day 7 and day 28 ($p = 0.0071$) (Figure 2.7A). In nude mice the axillary, inguinal and popliteal nodes increased in volume over time; the axillary ($p = 0.010$) and inguinal nodes ($p = 0.016$) were significantly larger at day 28 compared to day 7 and the popliteal node was significantly larger at day 14 compared to day 7 ($p = 0.0046$) (Figure 2.7B). In SCID mice, the volumes of the brachial and inguinal nodes decreased significantly over time. The brachial ($p = 0.013$) and inguinal nodes ($p = 0.023$) were significantly smaller at day 14 compared to day 7. There were no significant differences in the volumes of the axillary and popliteal lymph nodes over time (Figure 2.7C).

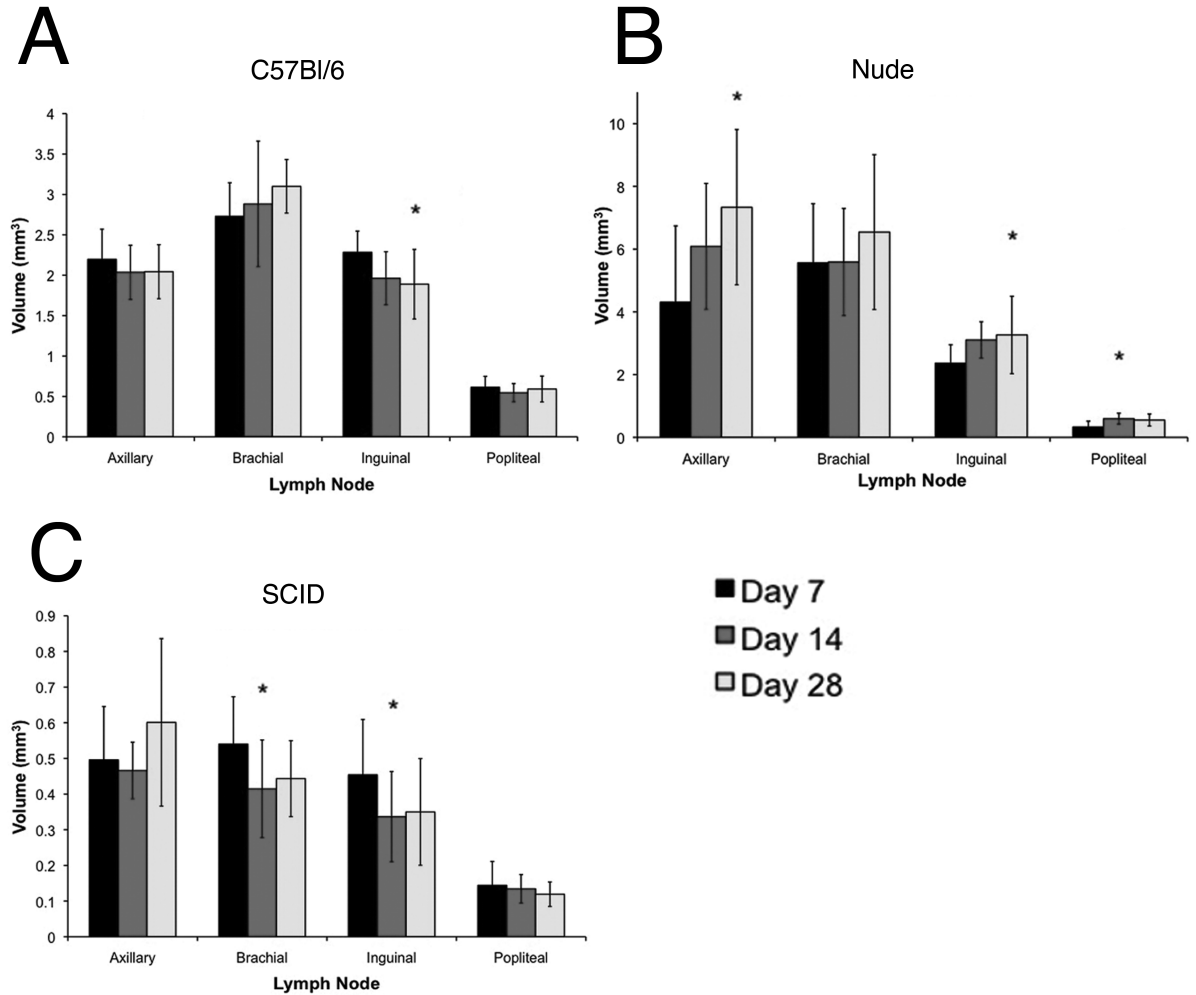


Figure 2.7 - Lymph node volumes over time. (A) C57Bl/6 mice. (B) Nude mice. (C) CB-17 SCID mice. Significant differences were found in the inguinal ($p = 0.0071$) nodes of C57Bl/6 mice. Significant differences were also found in the axillary ($p = 0.0104$), inguinal ($p = 0.0155$) and popliteal ($p = 0.0046$) nodes of nude mice. Significant differences were also found in SCID mice in the brachial ($p = 0.0130$) and inguinal nodes ($p = 0.0225$). (*) Significantly different compared to day 7. Repeated measures ANOVA test was used. Error bars represent the standard deviation.

2.4 Discussion

This is the first study to use MRI to assess the appearance of the lymph nodes and spleen in various immuno-deficient and wild-type mouse strains. Given the substantial differences in the cellular composition of the immune systems in these mice, and reports from a small number of pathological studies which noted differences in lymph node morphology between different mouse strains, we hypothesized that the MRI appearance of the lymphoid tissues would also be disparate in the immuno-deficient and wild-type mouse strains we examined. MRI revealed some considerable differences in the appearance of lymph nodes in the different mice. Most notably, some lymph nodes in nude and SCID mice appeared with a region of signal hyperintensity in bSSFP images. By comparing the bSSFP images with T1- and T2-weighted SE images we were able to determine that the high signal intensity in the bSSFP images is most likely due to the presence of fluid within the node. Fluids have long T1 and T2 relaxation times. In T1-weighted images tissues with long T1 relaxation times appear dark, while in T2-weighted images tissues with long T2 relaxation times appear bright. Contrast in bSSFP images is related to T2/T1 and tissues with similar T1 and T2 values, like fluids (and fat), will have T2/T1 close to 1, which results in high signal intensity. It is also worth noting that when nude mice were followed over time with MRI, those nodes that appeared with a region of signal hyperintensity did not change in appearance during the imaging experiment.

There are relatively few papers that describe the anatomical or cellular features of normal lymph nodes in immune-deficient mice. In a paper by Sainte-Marie and Peng,¹⁷ 8 types of lymph nodes, in 7 nude and 4 C57Bl/10 mice, were carefully assessed by histopathology. They showed that in nude mice the absence of the thymus greatly inhibits the development of the lymphocyte population in the cortex, creating a small cavity. In addition, in some mice a cyst of variable size was found in the axillary or brachial nodes, often near the hilus.¹⁷ These findings are similar to our observations in nude mice by MRI, where fluid filled cavities were observed in the axillary, brachial and inguinal nodes.

A histological examination of the immune organs in SCID mice, by Ge et al., showed that the lymph nodes had no clear cortex and appeared to be totally devoid of lymphocytes.¹⁸ These modifications of lymph node anatomy could also be expected to result in features such as

cavities or cysts. Our histology demonstrated that nodes which appeared with a region of high signal intensity in MR images, had a cavity within them, supporting the notion of a fluid-filled node.

Exposure of immuno-deficient mice to potentially pathogenic organisms must be restricted. Specific pathogen free (SPF) housing systems, often referred to as barrier facilities, are commonly used to house immuno-deficient mice and employ sterilization of feed, bedding, water, and cages along with the use of filter-top or individually ventilated caging systems and strict adherence to aseptic techniques for animal handling. Lymph nodes may enlarge when immune cells react to pathogen, such as virus or bacteria, due to proliferation of lymphocytes. Swollen glands, common to many illnesses, are an example of nodes enlarging in response to a pathogen. The immuno-deficient mice used in our longitudinal imaging studies leave the barrier facility for the first scanning session (day 7 after arrival) and thereafter were housed within an external barrier in ventilated cages. They were transported to/from the external barrier and the MRI facility for the next two scans (days 14 and 28). We hypothesized that the transfer between barriers and time spent outside of the barrier in the MRI facility, would result in changes in the size of the lymph nodes. To test this we imaged wild-type, nude and SCID mice at three time-points and measured the lymph node volumes. Changes in the lymph node volumes were measured for all mice. The largest changes were observed in the nude mice, however, the node volume in nude mice was found to be the most variable for all scans. In SCID mice the node volume was actually observed to decrease over time. However, there was no trend for increasing node size with number of times imaged (or number of transfers out of the barrier).

Even though the lymph nodes in these immuno-deficient mice are underdeveloped, or rudimentary, many studies show that the lymph nodes are a frequent site of cancer metastases.^{11,19,20} In fact several studies suggest that lymph node metastases are more common in the mice with the more severe immunodeficiencies.^{12,13} Dewan et al. have reported that the rate of metastasis of human breast cancer cells (MDA-MB-231) is much higher in NOG mice, compared to NOD/SCID mice inoculated in the same way.¹² This included metastasis to the regional lymph nodes. It is interesting that, even though lymph nodes in NOG mice are not obvious at dissection, and not visible in MR images, the rudimentary node tissue still provides a suitable microenvironment for metastatic growth.

When lymph nodes are abnormal they increase in size.²¹ Enlarged lymph nodes are readily visible in MRI. In fact, traditionally, MRI of the lymphatic system has been focused on conventional anatomical imaging whereby enlargement of lymph nodes is considered the primary diagnostic criterion for disease. Secondary architectural and pathological changes are also often apparent on MRI. It is therefore important to recognize that, in the different mouse strains we imaged, the size and appearance of the lymph nodes is quite variable in healthy animals and the lymph node volumes change over time in both wildtype and immuno-deficient mouse strains. A change in the lymph node size, as measured by MRI, in these mice should not be considered evidence of disease without additional validation.

In diseased lymph nodes the tissue is sometimes homogenized so that the cortical and medullary areas are no longer differentiated.²² Necrosis may lead to accumulation of fluid (pus) within nodes, and can cause a fluid filled cavity. It is therefore very important to recognize that some diseased nodes can appear hyperintense in bSSFP and T2-weighted images (or with low signal in a T1-weighted image) and that this has the potential to be confused with normal lymph nodes in non-tumor bearing immuno-deficient mice.

The MRI appearance of the spleen in the different mouse strains was also notable. The spleens of wild-type and nude mice were quite similar in size and MRI appearance; a distinct architectural pattern is observed in MR images of the spleen in wild-type and nude mice. In SCID and NOG mice, the images show a smaller spleen (3-5x smaller in volume) devoid of pattern and in the case of the NOG mouse acellular. These differences in the MRI appearance likely reflect the impaired development of the spleen in these mice.

The normal spleen is composed of what is known as (non-lymphoid) red pulp and (lymphoid) white pulp. Red pulp consists of connective tissue and many splenic sinuses that are engorged with blood, giving it a red appearance. It functions to filter the blood and is a storage site for red blood cells.²³ It is also a reserve site for monocytes, which upon injury or disease leave the spleen and migrate to tissues for repair.²³ The high blood content causes it to appear with very low signal intensity in bSSFP images. White pulp consists of lymph nodules (germinal centers), composed of follicles, and periarteriolar lymphoid sheaths. White pulp is rich in lymphocytes.²³

SCID mice contain a defect preventing the functional development of T- and B-lymphocytes.^{24,25} Ge et al. have shown by histology that SCID mice have relatively empty splenic follicles.¹⁸ It is because of these deficits the spleen in SCID mice is rudimentary in appearance and function. By MRI it appears to have no tissue contrast within it, suggesting minimal structural features. The NOG mouse is a SCID mouse strain that has multi-functional defects in NK activity, macrophage function, complement activity and dendritic cell function, in addition to lacking T- and B-cells. In all NOG mice examined by MRI the spleen appeared black reflecting an absence of signal likely due to an absence of cellularity.

In summary, this paper investigates an important technical aspect of mouse body imaging, namely the differential appearance of lymph nodes and spleens in 4 commonly used strains of experimental mice (C57Bl/6, nu/nu, CB-17 SCID, and NOG). These strains of mice are widely used for cancer research, and imaging is often used to identify metastasis to lymph nodes and distant organs. The use of these mice is not standardized; different laboratories use certain mice for a variety of reasons, and differences in the appearance of the lymph nodes across the strains can be a source of confusion in data interpretation. We have shown that there are particular features within the nodes of some mice that can mimic the appearance of pathology. We have found that changes in the size of nodes, in healthy mice, that occur with repeated imaging fall within the typical range of node sizes, which show variability. By presenting knowledge of the normal MRI appearance of the lymphoid organs in healthy, immuno-deficient and immuno-competent mice we provide information that will help to avoid data misinterpretation and to advance the field.

2.5 References

1. Hudson, W., Li, Q., Le, C. & Kersey, J. Xenotransplantation of human lymphoid malignancies is optimized in mice with multiple immunologic defects. *Leukemia* **12**, 2029–2033 (1998).
2. Clarke, R. Human breast cancer cell line xenografts as models of breast cancer. The immunobiologies of recipient mice and the characteristics of several tumorigenic cell lines. *Breast Cancer Res Treat* **39**, 69–86 (1996).
3. Croy, B., Linder, K. & Yager, J. Primer for Non-immunologists on Immune-Deficient Mice and Their Applications in Research. *Comparative Medicine* **51**, 300 (2001).
4. Shultz, L. D. *et al.* Multiple Defects in Innate and Adaptive Immunologic Function in NOD/LtSz-scid Mice. *J Immuno* **154**, 180–191 (1995).
5. Greiner, D. L. *et al.* Improved Engraftment of Human Spleen Cells in NOD/LtSz-scid/scid Mice as Compared with C.B-17-scid/scid Mice. *Am J Pathol* **146**, 888–902 (1995).
6. Ito, M. *et al.* NOD/SCID/gamma null c mouse: an excellent recipient mouse model for engraftment of human cells. *Blood* **100**, 3175–3182 (2002).
7. Ito, M., Kobayashi, K. & Nakahata, T. NOD/Shi-scid IL2r(gamma)null (NOG) Mice More Appropriate for Humanized Mouse Models. *Cur Top Microbiol Immunol* 53–76 (2008). at <<http://www.springerlink.com/index/X5810886622434K5.pdf>>
8. Brüner, N., Boysen, B., Romer, J. & Spang-Thomsen, M. The nude mouse and an in vivo model for human breast cancer invasion and metastasis. *Breast Cancer Res Treat* **24**, 257–264 (1993).
9. Troiani, T. *et al.* The use of xenograft models for the selection of cancer treatments with the EGFR as an example. *Critical Reviews in Oncology/Hematology* **65**, 200–211 (2008).

10. Mukhopadhyay, R., Theriault, R. L. & Price, J. E. Increased levels of $\alpha 6$ integrins are associated with the metastatic phenotype of human breast cancer cells. *Clinical & Experimental Metastasis* **17**, 325–332 (1999).
11. Price, J. E., Polyzos, A., Zhang, R. D. & Daniels, L. M. Tumorigenicity and Metastasis of Human Breast Carcinoma Cell Lines in Nude Mice. *Cancer Research* **50**, 717–721 (1990).
12. Dewan, M. Z. *et al.* Natural killer cells in breast cancer cell growth and metastasis in SCID mice. *Biomedicine & Pharmacotherapy* **59**, S375–S379 (2005).
13. Mikhailov, A. D., Malakhov, A. A., Revazova, E. S., Valyakina, T. I. & Yudicheva, T. V Metastasizing of Human Melanoma on Immunodeficient Mice. Comparison of Cell Lines with Different Metastasizing Activity. *B Exp Biol Med* **119**, 206–208 (1995).
14. Xie, X. *et al.* Comparative studies between nude and scid mice on the growth and metastatic behavior of xenografted human tumors. *Clin Exp Metastasis* **10**, 201–210 (1992).
15. Taghian, a *et al.* Quantitative comparison between the transplantability of human and murine tumors into the subcutaneous tissue of NCr/Sed-nu/nu nude and severe combined immunodeficient mice. *Cancer Res* **53**, 5012–7 (1993).
16. Rosset, A., Spadola, L. & Ratib, O. OsiriX: an open-source software for navigating in multidimensional DICOM images. *J Digit Imaging* **17**, 205–16 (2004).
17. Sainte-Marie, G. & Peng, F. Structural and cell population changes in the lymph nodes of the athymic nude mouse. *Laboratory Investigation* **49**, 420–429 (1983).
18. Ge, W. *et al.* Observation on husbandry and reproduction of mice with severe combined immunodeficiency and histological examination of their immune organs. *Chinese Journal of Cancer Research* **3**, 6–13 (1991).
19. Matsui, J. *et al.* Multi-Kinase Inhibitor E7080 Suppresses Lymph Node and Lung Metastases of Human Mammary Breast Tumor MDA-MB-231 via Inhibition of

- Vascular Endothelial Growth Factor-Receptor (VEGF-R) 2 and VEGF-R3 Kinase. *Clinical Cancer Research* **14**, 5459–5465 (2008).
20. Dadiani, M. *et al.* Real-time imaging of lymphogenic metastasis in orthotopic human breast cancer. *Cancer Res* **66**, 8037 (2006).
 21. Barrett, T., Choyke, P. L. & Kobayashi, H. Imaging of the lymphatic system : new horizons. *Contrast Med Mol Imaging* **1**, 230–245 (2006).
 22. Hutter, R. Pathological parameters useful in predicting prognosis for patients with breast cancer. *Monogr Pathol* **25**, 175–185 (1984).
 23. Cesta, M. F. Normal structure, function, and histology of the spleen. *Toxicologic Pathology* **34**, 455–65 (2006).
 24. Sculer, W. & Bosma, M. J. Nature of the scid defect: a defective VDJ recombinase system. *Cur Top Microbiol Immunol* **152**, 55–62 (1989).
 25. Bosma, G. C., Custer, R. P. & Bosma, M. J. A severe combined immune immunodeficiency mutation in the mouse. *Nature* **301**, 527–530 (1983).

Chapter 3

3 Comparing Tumor Growth and Metastasis in Xenograft Models of Breast Cancer using MRI

3.1 Introduction

Metastasis from a primary tumor is the main cause of most cancer related deaths.^{1,2} A common method for studying metastasis and tumor progression involves conducting histology-based studies, which use tissue samples collected at multiple timepoints and require large groups of animals. These studies only provide a snapshot of how a particular tumor is progressing over time. These studies also do not allow for the occurrence of specific events, such as metastases, to be studied in detail to determine their time course of development.

With the development of powerful preclinical imaging technologies, such as high resolution MRI, many of the issues with the current methods for studying tumor metastases, such as only being able to examine portion of an organ and potentially missing metastatic foci for analysis, can be avoided.³ High resolution MRI allows for whole mouse body imaging. This gives more information about the progression of the tumor and where additional metastatic disease may be located. Imaging also allows the same animals to be monitored over time, allowing the sequence of events from tumor development to the formation of obvious metastases to be determined for each animal. These longitudinal studies require fewer animals compared to traditional histological studies.

A wide variety of models are currently used to study cancer metastases.⁴ Some of these models consist of transgenic animals that will spontaneously form tumors while others are transplant models that use either syngenic, allogenic or xenogenic grafts of cancer cells.^{2,4} Xenogenic models are frequently used since these models allow human cancers to be studied in vivo, but require animals with significant immune deficiencies for proper engraftment. These immune deficient models pose a different problem, as the immune system is known to play a role in the development of tumors, potentially altering their growth characteristics and metastases.²

Hudson et al. examined the effect of these mutations on tumor growth and formation and found that animals with more pronounced immune deficiencies produced larger tumors and had a slightly higher percentage of tumors form.⁵

Carreno et al. observed similar results when comparing the ability of human melanoma cells derived from cell lines to form metastases in the lungs of SCID, NOD/SCID, NOD/SCID B2null and NOD/SCID IL2Rnull mice when injected intravenously.⁶ The ability of MDA-MB-435 breast cancer cells implanted into the mammary fat pad of nude, SCID and NIH-3 mice to metastasize to the lung has been studied by Price et al. who found the highest incidence of metastases and the most metastatic foci in the lungs of SCID mice.⁷ In the same study, they also demonstrated a difference in tumorigenicity in different breast cancer cell lines and how the tumorigenicity can be affected by implanting cells under different conditions, such as with matrigel, fibroblasts and even normal breast epithelial cells.⁷

Xie et al. compared the formation of spontaneous lung metastases from various cancer cell lines in nude and SCID strains. They found that more metastases formed in SCID mice compared to nude mice in most of the cell lines that were examined and that the MDA-MB-435 cell line formed the highest number of metastases in both of the strains examined.⁸

Although many investigators have studied the effect of the various immune deficiency mutations on tumor growth and spontaneous metastases to the lungs and other major organs, there is little data available on the effects of immune deficiency on the development of metastases in regional lymph nodes. The lymph nodes are very small in some immune-compromised mouse strains; for example most nodes in NOD/SCID IL2Rnull mice are absent or rudimentary and difficult to locate by dissection or high resolution MRI.⁹

In this study, our goal was to compare tumor formation and lymph node metastasis in nude and SCID mice using high resolution MRI. We compared MRI to basic histology to evaluate the utility of MRI for monitoring the development of the primary tumor and quantifying metastases.

3.2 Materials and methods

3.2.1 Animal Models

Female nude (nu/nu) and C.B.-17 SCID mice (CB17/Icr-Prkdc^{scid}/IcrIcoCr1), 6 to 8 weeks old, were injected into the thoracic mammary fat pad with 1×10^6 MDA-MB-231 or MDA-MB-435 cells, resulting in a total of four groups ($n = 8$ per group). The MDA-MB-435 cell line has recently been reclassified as a melanoma from a ductal carcinoma. More information about this cell line is provided in the discussion.

For the cell injection, the animals were anesthetized using isoflurane (3% for induction and 1% for maintenance) in oxygen and an incision was made between the centre of the chest and the right forelimb, just below shoulder level and the mammary fat pad was exposed. Cells suspended in HBSS were injected into the fat pad in a volume of $50 \mu\text{L}$. The incision was then closed with Vet Bond surgical glue (3M, London, Ontario, Canada) and the mouse was weighed and allowed to recover.

3.2.2 MRI imaging in mice

All mice received two MRI scans one week apart. The first MRI scan was conducted when the tumor diameter had reached approximately 1 to 1.5 cm. Mice that had received 231 cells were scanned on days 21 and 28 while mice that received 435 cells were scanned on days 30 and 37; since the growth rates of the two cell lines was known to be different (slower for 435).

All imaging was performed on a 1.5 T GE Scanner using custom-built hardware, including a gradient insert coil and mouse body radiofrequency coil. A 3D balanced steady state free precession (bSSFP) pulse sequence was used to acquire full body images of each animal. The imaging parameters were a flip angle of 40° , a receiver bandwidth of 31.25 kHz, a TR of 6.7 ms, a TE of 3.3 ms, 4 phase cycles, 4 averages, half phase field of view and 200-micrometer

isotropic resolution. Animals were anesthetized during imaging using the same procedures as those used for performing the mammary fat pad injections.

3.2.3 Histology

Mice were sacrificed following their final scan and the primary tumor, left and right axillary and brachial lymph nodes were removed. Tissues were fixed in formalin and embedded in paraffin for sectioning. Five μm thick tissue sections were cut and stained with Hemotoxilyn and Eosin (H&E).

3.2.4 Image Analysis

The Osirix image analysis software¹⁰ was used to make all measurements from images acquired in this study. The volume of the primary tumor and of the left and right axillary and brachial lymph nodes were measured by manual segmentation from all of the acquired images. Each tumor or lymph node of interest was segmented individually on every image slice to create a series of regions of interest (ROI). One ROI from the organ's ROI series was selected and the volume was calculated by using the ROI volume calculation tool available within the software package. This procedure was repeated to calculate the volume for all organs of interest in each image.

3.2.5 Statistical Analysis

All volume data were compared statistically using Graph Pad Prism analysis software (GraphPad Software, La Jolla, CA). Tumor volumes were compared using a two-way Analysis of Variance test. Lymph node volumes were compared using a Kruskal-Wallis test.

A Fisher's Exact test was used to compare the number of animals in each group that developed metastases and to determine which factors had a significant effect.

3.3 Results

3.3.1 Differences in Tumor Growth

3.3.1.1 MRI Appearance of Primary Tumors and Histology

With the 3D MRI techniques used in this study, we were able to visualize the entire mouse body, the primary tumor in the mammary fat pad and the lymph nodes (Figure 3.1). The number of animals that formed tumors was similar between strains and cell lines (Table 3.1).

Tumors in all groups displayed signal heterogeneity (Figure 3.2), however this was more pronounced in the groups that received 231 cells, which also produced larger tumors (Figure 3.2A and C). The MRI appearance of tumors from the same cell line was similar, regardless of the strain.

Table 3.1 – Number of animals in each group that formed tumors

	MBA-MB-231	MDA-MB-435
Nude	7/8	8/8
SCID	8/8	8/8

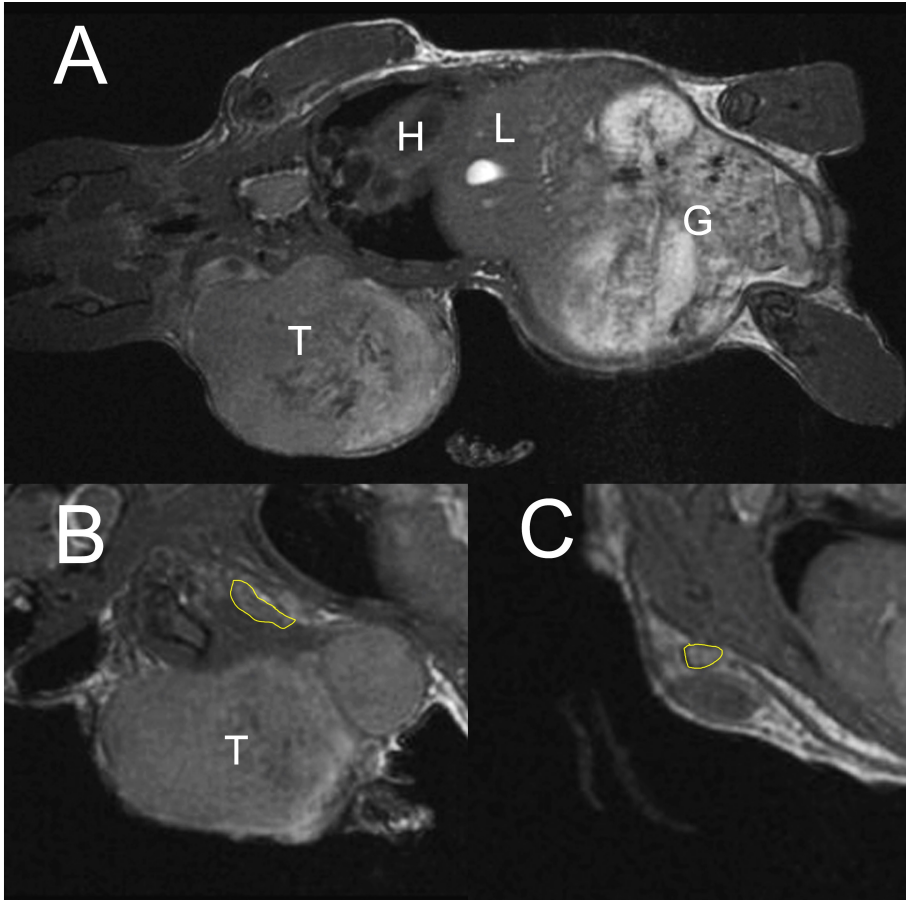


Figure 3.1 - Image of tumor bearing mouse. (A) Whole mouse body. T - tumor, H - heart, L - lungs, G - gut. (B) Image of axillary lymph node (outlined in yellow). (C) Image of brachial lymph node (outlined in yellow).

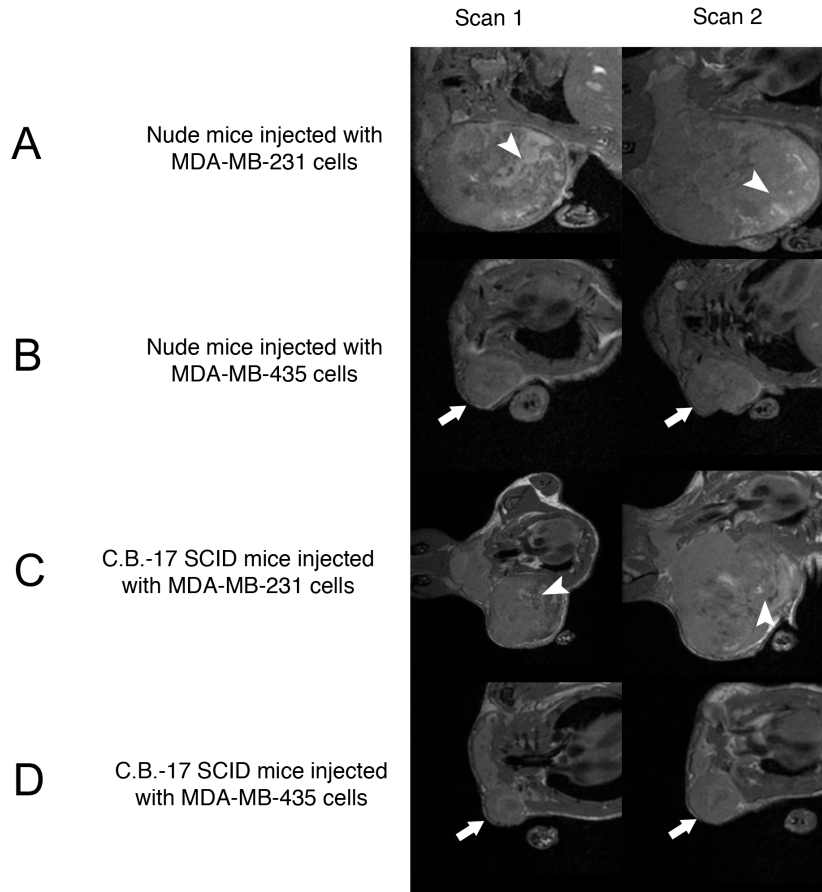


Figure 3.2 – Appearance of tumors at both scan time points. Tumors generated from MDA-MB-231 cells (A - nude and C - SCID) are much larger and have regions of heterogeneous signal intensity (arrowheads). Tumors generated from MDA-MB-435 cells (B - nude and D - SCID) are much smaller and have a more homogeneous appearance (arrows). The MRI appearance of tumors for each cell line was similar regardless of the strain. Scan 1 – day 21 for groups with 231 cells, day 30 for groups with 435 cells; Scan 2 – day 28 for groups with 231 cells, day 37 for groups with 435 cells.

Tumors generated from the same cell line had a similar histological appearance, regardless of the strain. Figure 3.3 shows H&E stained sections of tumors from all groups. Examination of the tumors revealed that they frequently contained regions of fluid accumulation. This is consistent with the heterogeneous appearance in MR images; signal hyperintensity in bSSFP images represents the presence of fluid or fat accumulation. These tumors also had tracks of

stromal cells that were not very well defined from the tumor cells. We also noticed that some tumors had areas of decreased cellularity and areas that appeared similar to lipid vacuoles.

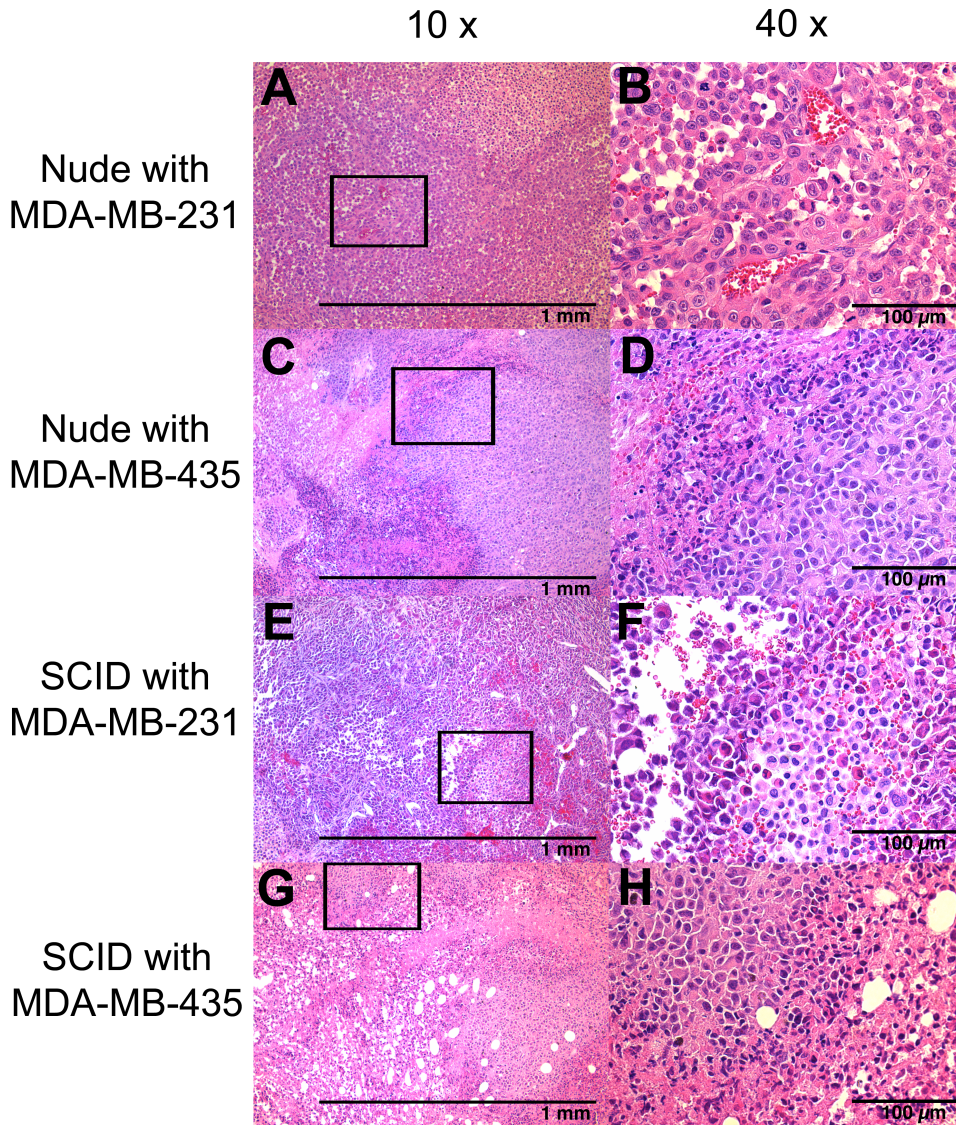


Figure 3.3 - H&E stained sections of tumors. (A, B) Tumor from nude mouse injected with 231 cells. (C, D) Tumor from nude mouse injected with 435 cells. (E, F) Tumor from SCID mouse injected with 231 cells. (G, H) Tumor from SCID mouse injected with 435 cells. Images A, C, E, and G were taken at 10x magnification. Images B, D, F and H were taken at 40x magnification. The box in images A, C, E and G highlights the area that is shown in the adjacent image in the second column.

3.3.1.2 Tumor Volume

Because all images were acquired in 3D tumor volume can be measured (Figure 3.4). At scan 1, both strain and cell line had a significant effect on the tumor volume. Tumors produced from the 231 cell line were much larger and tumors produced in the nude strain were also larger. At the second scan time point, the effect of the strain on tumor volume is not significant, but the effect of the cell line is. Tumors produced from the 231 cell line were much larger than those produced from the 435 line. The 231 tumors reached a diameter of 1 to 1.5 cm quicker than those produced from the 435 cells. Animals that bore the 231 tumors were initially imaged on day 21 whereas animals with 435 tumors were imaged for the first time on day 30, regardless of the strain. On average, tumors from nude mice with 231 cells were approximately 17 and 19 times larger than those from nude mice with 435 cells at the first and second scan time points respectively. In SCID mice with 231 cells, tumors were approximately 24 and 29 times larger than those from SCID mice with 435 cells at the first and second scan time points respectively.

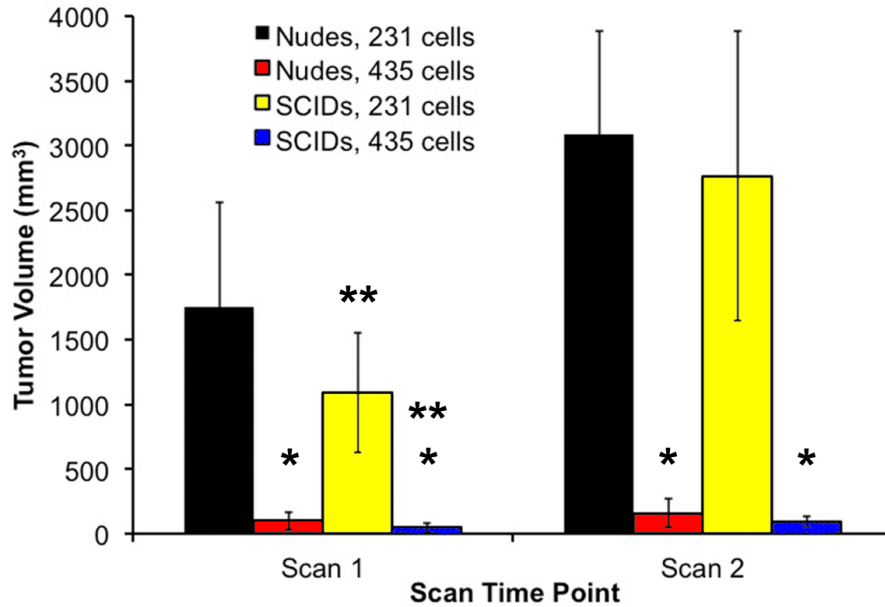


Figure 3.4 – Tumor volumes over time. For animals injected with MDA-MB-231 cells (231 cells), Scan 1 was at 21 days and Scan 2 was at 28 days. For animals injected with MDA-MB-435 cells (435 cells), Scan 1 was at 30 days and Scan 2 was at 37 days. ** Significant compared to nude mice. * Significant compared to the 231 cell line.

3.3.2 Differences in Metastases

The thoracic mammary fat pad, where cells were injected, is drained by both the axillary and brachial lymph nodes. From our 3D MR images, we were able to determine the volume of both these lymph nodes, as well as examine these nodes for an abnormal MRI appearance, which may be evidence of metastatic disease, before a post mortem exam.

Image data from lymph nodes in tumor bearing mice was compared to data from healthy control mice that are presented in Chapter 2. The data from the day 28-time point in the longitudinal experiment in Chapter 2 was used specifically to match the number of times that animals had been removed from pathogen free housing conditions.

All axillary and brachial lymph nodes were sectioned and examined by H&E staining for evidence of metastasis and were compared with the image data.

3.3.2.1 Lymph Node Appearance

Lymph nodes had a variable appearance in the MRI images at both scan time points. In nude mice injected with 231 cells, the lymph nodes were typically enlarged and had a heterogeneous appearance (Figure 3.5, row 2), which may be indicative of a pathological process within the node. Differences were seen between cell lines, with very few of the nodes in animals injected with 435 cells displaying the altered appearance that was frequently seen in the 231 group. Lymph nodes in animals that received the 435 cells had a similar appearance to those of non-tumor bearing control animals, which is also shown (Figure 3.5, rows 3 (435 tumors) and rows 1 (control)). Similar results were also observed in SCID mice. The lymph nodes of SCID mice injected with 231 cells had a similar appearance with areas of signal heterogeneity and enlargement (Figure 3.6, row 2).

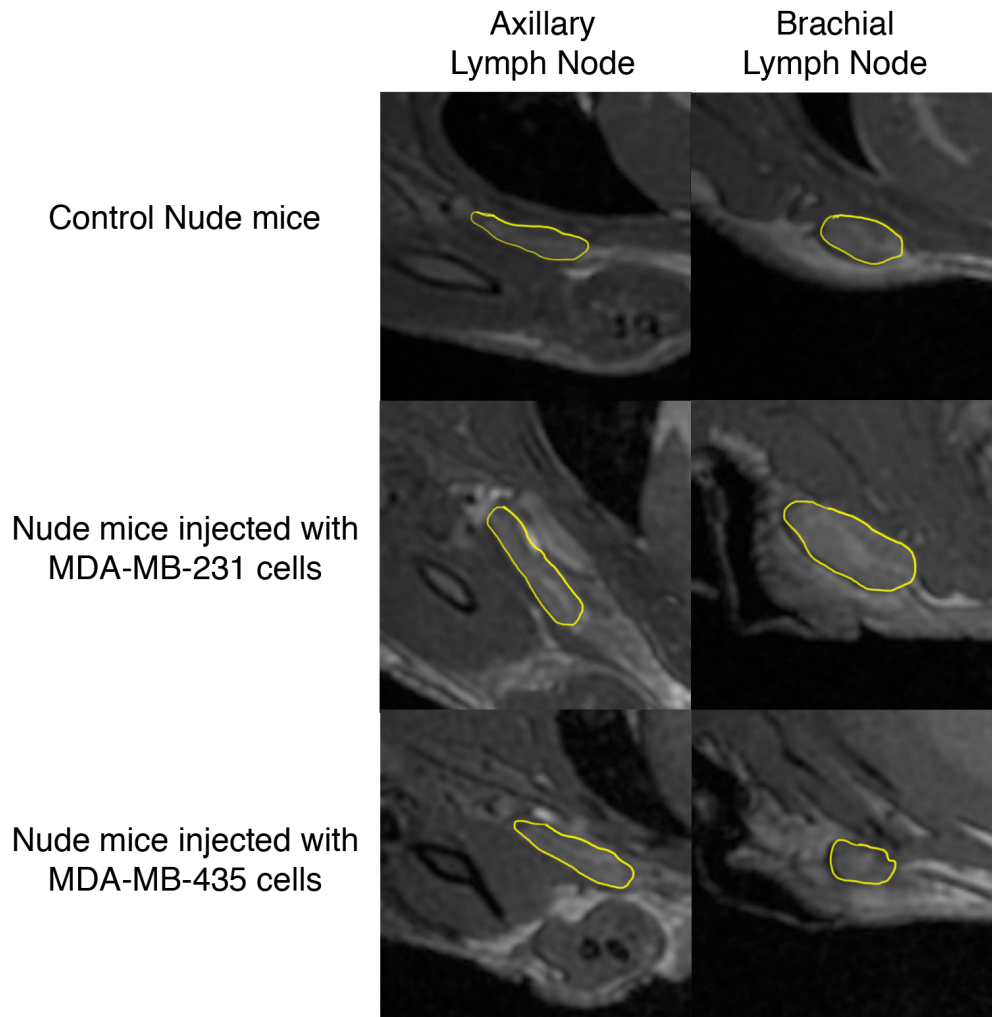


Figure 3.5 – MR appearance of nude mouse lymph nodes. Lymph nodes (outlined in yellow in all images) in mice injected with MDA-MB-231 cells (row 2) were enlarged and had a heterogeneous appearance. Lymph nodes from animals injected with MDA-MB-435 cells (row 3) have a similar appearance to control animals (row 1).

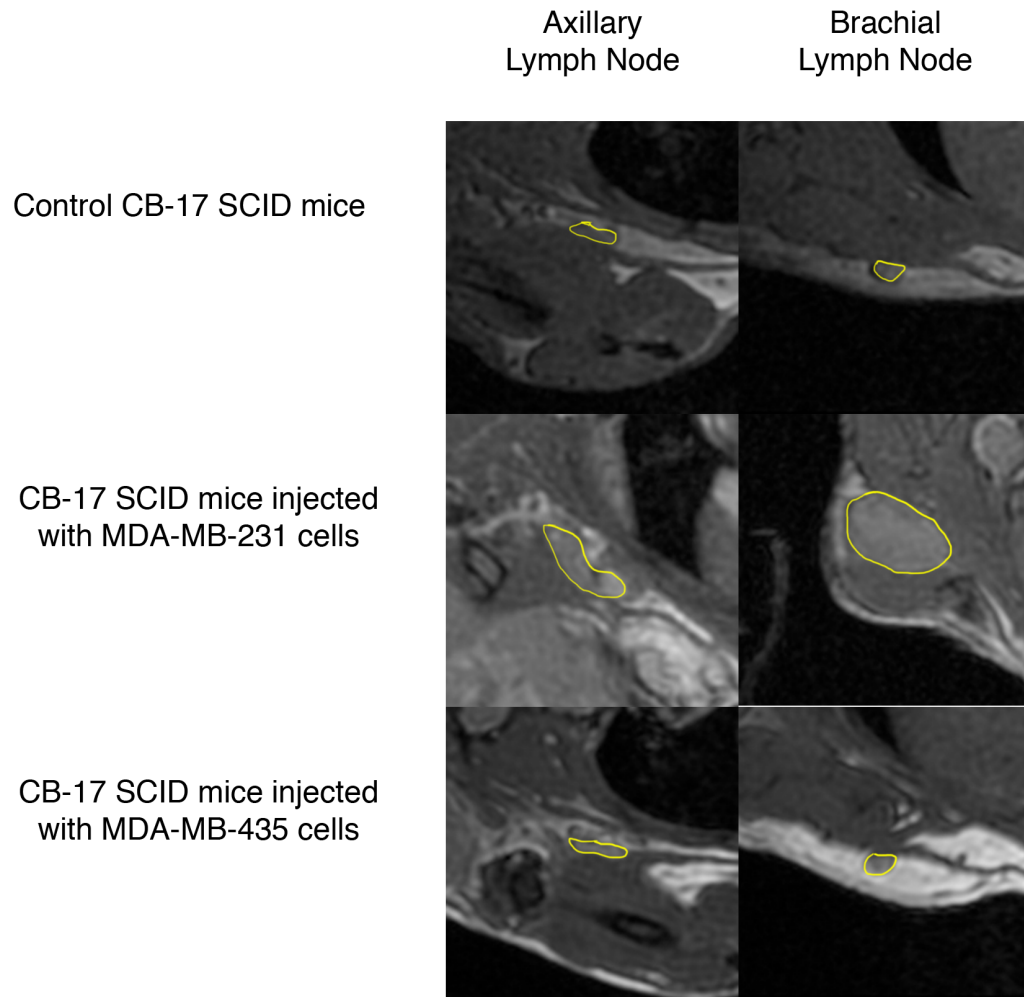


Figure 3.6 – MR appearance of SCID mouse lymph nodes. Lymph nodes (outlined in yellow in all images) in mice injected with MDA-MB-231 cells (row 2) were enlarged and had a heterogeneous appearance. Lymph nodes from animals injected with MDA-MB-435 cells (row 3) have a similar appearance to control animals (row 1).

3.3.2.2 Lymph Node Volume and Histology

We compared the lymph node volumes using a Kruskal-Wallis test. At the first scan time point, the volume of the brachial nodes from nude mice injected with 231 cells were significantly larger compared to those injected with 435 cells ($p = 0.0012$), while no significant difference was observed in the axillary nodes of nude mice ($p = 0.0677$) (Figure 3.7A). In SCID mice, the axillary nodes from animals that received 231 cells were significantly larger than control and 435 groups ($p = 0.0012$), while the brachial nodes of animals with 231 cells were significantly larger than controls ($p = 0.0186$).

At the second scan time point, a significant difference was observed in both the axillary and brachial lymph nodes from both nude and SCID strains. In the nude strain, the axillary nodes of mice with 231 cells were significantly larger than controls ($p = 0.0126$), the brachial nodes of mice with 231 cells were significantly larger than those with 435 cells ($p = 0.0164$). In the SCID strain, the axillary and brachial nodes of mice with 231 cells were larger than those that received 435 cells and controls ($p = 0.0001$ for both nodes).

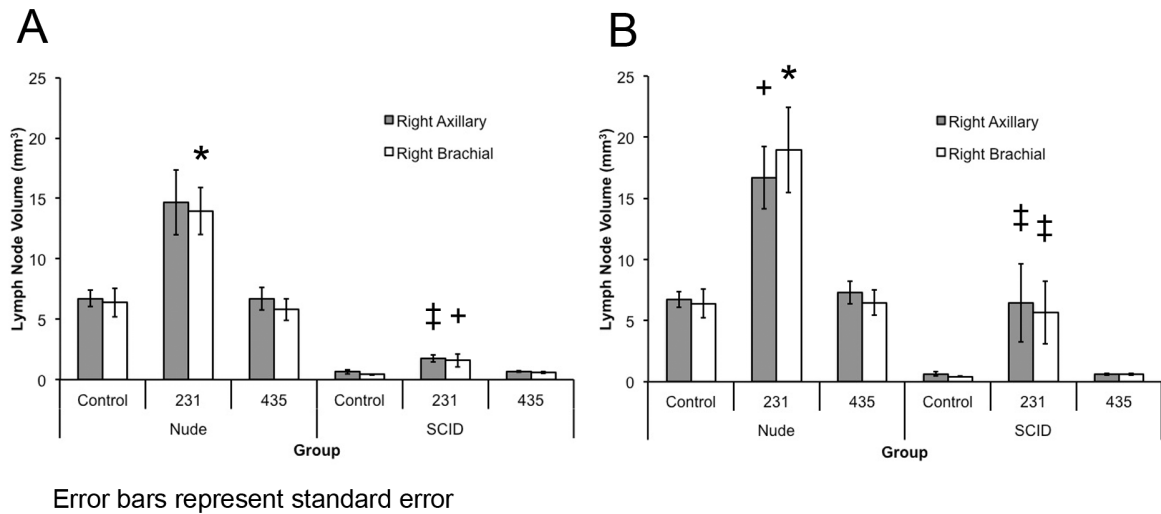


Figure 3.7 – Lymph node volumes. (A) Scan 1, (B) Scan 2. The lymph nodes of animals injected with 231 cells were found to be significantly larger than those in control animals and animals injected with 435 cells. * - Significant compared to 435 cells. + - Significant compared to Controls. ‡ - Significant compared to both 435 cells and controls.

We next examined H&E stained lymph node sections for evidence of metastases. With the assistance of a pathologist (Dr. Alan Tuck), we looked for cells under the capsule of the lymph nodes that had large, abnormal nuclei and a high nucleus to cytoplasm ratio. We found no lymph node metastases in mice injected with 435 cells. In groups that received 231 cells, of the animals that were examined, we found that 6 of 7 nude mice and 4 of 5 SCID mice had lymph node metastases. No significant difference was found between strains in the incidence of metastases to lymph nodes, however, 2/5 SCID mice had multiple metastatic lymph nodes (Table 3.2).

Table 3.2 – Number of Animals injected with MDA-MB-231 cells with Single or Multiple Lesions

	No Metastases	Single Lesion	Multiple Lesions
Nude	1/7	6/7	0/7
SCID	1/5	2/5	2/5

A lymph node from a 231 tumor-bearing group was considered enlarged if its volume measured by MRI was more than 2 standard deviations from the control node volume in the same strain. An enlarged node in MRI did not always correspond with a node that had evidence of metastasis by histology. Table 3.3 shows the rates of true and false positives and negatives in the groups that received 231 cells. In nude mice with 231 tumors 11/13 mice had enlarged lymph nodes on MRI, however, 5 of these 11 mice had metastasis determined by histology and 6 did not. There was also one node in this group that had a normal volume, although a metastasis was detected by histological examination. In SCID mice with 231 tumors 7/7 mice had enlarged nodes on MRI and 6/7 of these had evidence of metastasis in the node histology. There was one false positive node. In groups that received 435 cells, all nodes in nude mice were of a normal volume and did not contain metastases, while 3/13 nodes in SCID mice were enlarged with no metastases.

The lymph nodes that were enlarged, but non-metastatic had evidence of cellular reactivity; macrophage hyperplasia in the SCID mouse and plasma cell hyperplasia in nude mice. Reactivity was found in metastatic nodes as well as nodes that were normal in volume (Figure 3.8). The reactivity could reflect an immune response to the implanted tumor.

Table 3.3– Correspondence of lymph node volume and presence of metastases. Nodes were considered ‘enlarged’ if their volume was more than 2 standard deviations away from the volume of the corresponding control lymph node. Positive – Metastasis present, Negative – No metastasis.

	True Positive	False Positive	False Negative	True Negative	Total number of nodes analyzed
Nude, 231 cells	5	6	1	1	13
SCID, 231 cells	6	1	0	0	7

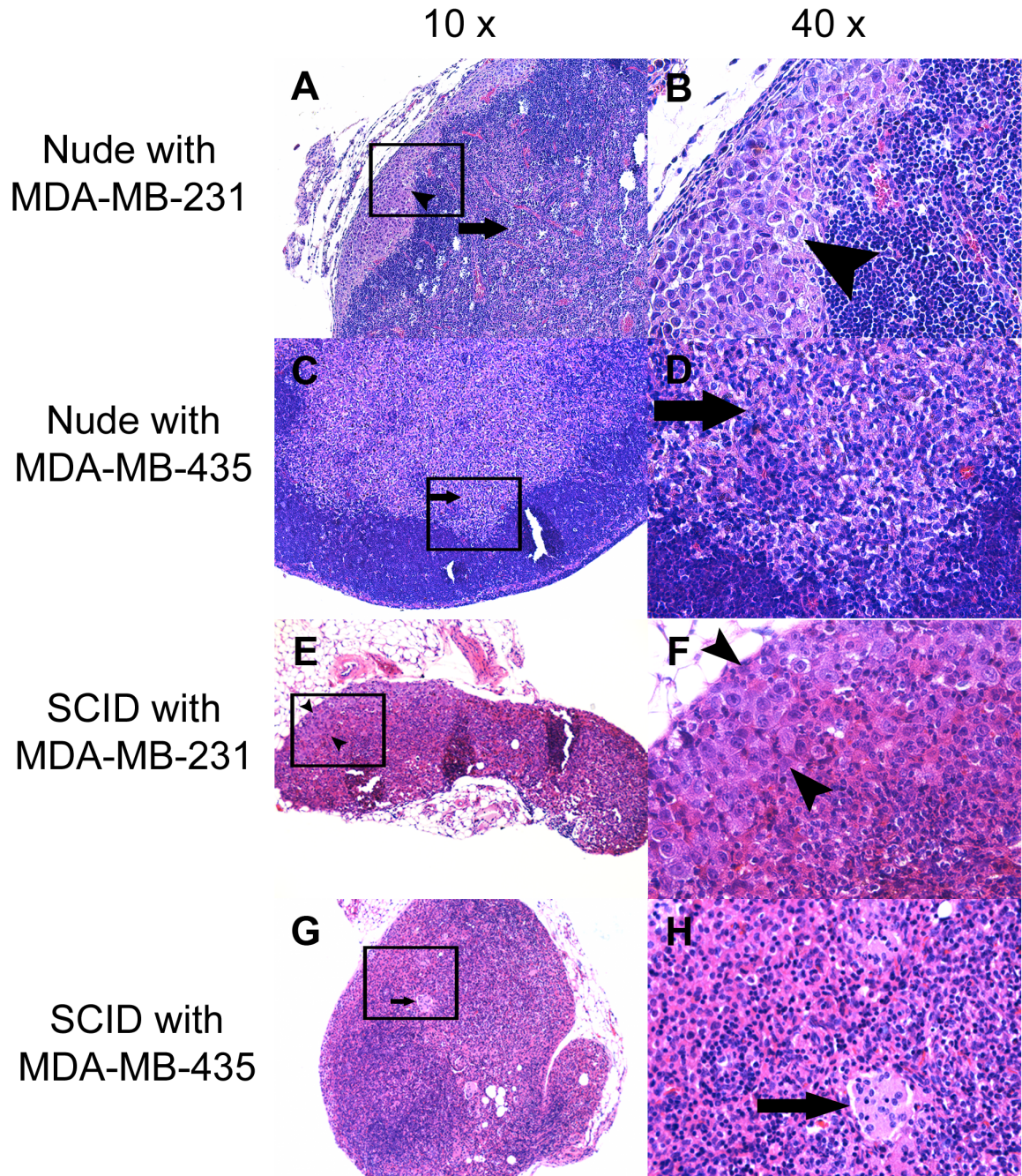


Figure 3.8 – Hematoxylin and Eosin stained lymph node sections. (A, B) Nude with 231 cells, (C, D) Nude with 435 cells, (E, F) SCID with 231 cells, and (G, H) SCID with 435 cells. Sections (A, C, E, G) are taken at x10 and sections (B, D, F, H) are taken at x40 with black boxes outlining the zoomed sections in the x10 images. In the animals injected with 231 cells, metastases can be found underneath the lymph node capsule in both Nude mice (A, arrowhead) and SCID mice (E, arrowheads), These metastases are shown at a greater magnification in B and F respectively (B and F, arrowheads).

Evidence that metastatic lymph nodes are reactive is also seen in A (arrow). No metastases were present in the lymph nodes of animals that received 435 cells, but evidence of reactivity was seen (arrows in C, D, G and F). In the SCID mice specifically, areas with macrophage hyperplasia were frequently found (G and H, arrows) whereas nude mice had regions of plasma cell hyperplasia.

3.4 Discussion

In this study, we have compared the growth and metastasis of two cell lines in two different strains of immune-compromised mice using high resolution MRI. We observed differences in the volume of tumors that formed and in the volume of regional lymph nodes.

The tumor volume was affected significantly by the strain used at the first scan time point, but it was not significant at the second scan time point. This difference in volume may be due to differing microenvironments between the strains used in this study, but this does not have a lasting effect on the volume as the tumors continue to progress. At both scan time points, the cell line used had a significant effect on the tumor volume. There is a clear difference in the growth rate between these cell lines with the 231 cells producing much larger tumors in the short period of time that was used in this study.

We also observed that the volume of draining lymph nodes in the animals that received 231 cells were significantly larger than those that received 435 cells and/or controls. These measurements are in agreement with our histology observations, which only found metastases in the nodes of animals with 231 tumors. When comparing the MRI volume data directly to our histological findings for individual nodes, we found that the volume of the node did not always indicate the presence of a metastasis. The rate of false positives from our volume data was highest in nude mice that received 231 cells. This result is most likely a consequence of the high variability of lymph nodes in this strain, which was observed in chapter 2.⁹ The reactivity of nodes in this strain from attempting to mount an immune response may also contribute to the increased detection of false positives, but to a lesser extent. We frequently observed macrophage and plasma cell hyperplasia in both metastatic and non-metastatic lymph nodes. Plasma cell hyperplasia is a common occurrence in rodents.¹¹ Depending on the strength of the response the hyperplasia may cause the volume of a non-metastatic lymph node to increase enough to be classified incorrectly by MRI as a metastatic node. These results demonstrate that high resolution MRI is more successful at detecting changes in lymph node volumes, in animals with greater immune deficiencies and less variability in the lymph nodes, such as the SCID strain.

We did not observe any lymph node metastases in animals that received the 435 cells, while metastases to regional lymph nodes were frequently seen with the 231 cells. Other studies have compared these cell lines and have found that the 435 cell line is more aggressive, having a higher incidence of metastasis.¹² This is contrary to what we have seen in this current study. One possible explanation may be that amount of time used for these studies was different. In our current study, no animals were examined after 37 days or just over 5 weeks. In the study mentioned above, the animals were examined for metastases for as long as 16 weeks post tumor implantation.¹² Other studies using the 435 cell line have examined animals for as long as 54 days⁸ and even 6 weeks post resection of 1.5 cm tumors.⁷ This difference in time may be main reason for the difference in metastasis formation.

The growth differences between the cell lines used in this study may be related to the fact that 435 cells may be melanoma cells rather than breast cancer cells. There is a controversy surrounding the identity of this cell line. Originally, this cell line was described as a human breast ductal carcinoma. Sellappan et al. demonstrated that the 435 cell line has a protein expression profile similar to that of four other melanoma cell lines.¹³ In 2005 Garraway et al., noted the similarity of the SNP profile of MDA-MB-435 cells to that of the melanoma line M14.¹⁴ Rae et al. have since demonstrated that the 435 and M14 cell cultures are of common origin and suggest that the 435 cell line may have been contaminated with the M14 melanoma cell line¹⁵, which has led to the reclassification of the 435 cell line to melanoma by some investigators. The controversy over the origin of MDA-MB-435 cells has persisted, in part, due to conflicting reports on their cancer-like properties. This cell line has been reported to express both epithelial markers as well as expressing proteins consistent with originating from melanoma.^{13,16} As demonstrated in this work, the 435 cell line is also capable of generating tumors when implanted into the mammary fat pad. There have been reports that breast tumors can undergo lineage infidelity.¹⁶ As early as 1999, Nobukawa et al. described a case of primary breast cancer differentiating into a malignant melanoma.¹⁷ If the 435 cell line is in fact a melanoma, then this may explain the differences in growth that were observed in this study. Implanting melanoma cells into the mammary fat pad may not allow for the full growth potential of the cell line to be realized.

Even though there were differences observed between the cell lines used in this study, the behavior of each cell line was consistent between strains. The incidence of metastases was

similar between both nude and SCID strains injected with 231 cells. Some SCID mice injected with 231 cells developed metastases in multiple lymph nodes, which may be due to the increased immune deficiency of the SCID strain compared to the nude strain.^{8,18}

Both the nude and SCID strains lack T cells while the SCID strain also lacks B cells.^{18,19} These animals retain NK cells function and possess all other components of the immune system.^{18,19} Both T cells and NK cells are involved in the immune response to cancer and NK cells can impact metastasis formation in animal models.²⁰ Even though the nude strain possesses B cells, these cells are typically activated through T cell dependent pathways, leaving some deficits in B cell function in these mice.²¹ These similarities between the nude and SCID strains may explain the similarities in tumor growth and metastases.

Studies have been conducted using animals with greater immune deficiencies, such as NOD/SCID IL2R gamma null mice which have deficits in T and B cells and NK cells. These models may allow for higher numbers of metastases, but these animals may not be the best choice if high resolution MRI is used to monitor the lymph nodes as these animals have underdeveloped nodes that are not detectable using MRI.⁹ The current work presented suggests that a mammary fat pad xenograft model using 231 cells implanted into SCID mice is the most appropriate for studying lymphatic metastases using high resolution MRI, due to the low false positive and false negative rate for metastases detection based on MRI data. Even though this combination of strain and cell line was most effectively studied using MRI, the addition of contrast enhancement, either of the implanted cells or of the lymph nodes prior to imaging may further enhance the detection of metastatic lymph nodes.

3.5 References

1. Allan, A. L., Vantyghem, S. A., Tuck, A. B. & Chambers, A. F. Tumor Dormancy and Cancer Stem Cells: Implications for the Biology and Treatment of Breast Cancer Metastasis. *Breast Dis* **26**, 87–98
2. Céspedes, M. V., Casanova, I., Parreño, M. & Mangués, R. Mouse models in oncogenesis and cancer therapy. *Clinical and Translational Oncology* **8**, 318–329 (2006).
3. Barrett, J. W. *et al.* Assessing Immunotherapy Through Cellular and Molecular Imaging. *Experimental and Applied Immunotherapy* 389–408 (2011).
4. Hill, R. Models for Tumour Metastasis. *The Cancer Handbook, 2nd Edition* (2007).
5. Hudson, W., Li, Q., Le, C. & Kersey, J. Xenotransplantation of human lymphoid malignancies is optimized in mice with multiple immunologic defects. *Leukemia* **12**, 2029–2033 (1998).
6. Carreno, B. M. *et al.* Immunodeficient Mouse Strains Display Marked Variability in Growth of Human Melanoma Lung Metastases. *Clinical Cancer Research* **15**, 3277–3286 (2009).
7. Price, J. E. Metastasis from human breast cancer cell lines. *Breast Cancer Res Treat* **39**, 93–102 (1996).
8. Xie, X. *et al.* Comparative studies between nude and scid mice on the growth and metastatic behavior of xenografted human tumors. *Clin Exp Metastasis* **10**, 201–210 (1992).
9. Economopoulos, V., Noad, J. C., Krishnamoorthy, S., Rutt, B. K. & Foster, P. J. Comparing the MRI appearance of the lymph nodes and spleen in wild-type and immuno-deficient mouse strains. *PloS one* **6**, e27508 (2011).
10. Rosset, A., Spadola, L. & Ratib, O. OsiriX: an open-source software for navigating in multidimensional DICOM images. *J Digit Imaging* **17**, 205–16 (2004).

11. Elmore, S. a *Histopathology of the lymph nodes. Toxicologic Pathology* **34**, 425–54 (2006).
12. Price, J. E. & Zhang, R. D. Studies of human breast cancer metastasis using nude mice. *Cancer and Metastasis Reviews* **8**, 285–297 (1990).
13. Sellappan, S. *et al.* Lineage infidelity of MDA-MB-435 cells: expression of melanocyte proteins in a breast cancer cell line. *Cancer Res* **64**, 3479–85 (2004).
14. Garraway, L. *et al.* Integrative genomic analyses identify MITF as a lineage survival oncogene amplified in malignant melanoma. *Nature* **436**, 117–122 (2005).
15. Rae, J. M., Creighton, C. J., Meck, J. M., Haddad, B. R. & Johnson, M. D. MDA-MB-435 cells are derived from M14 Melanoma cells – a loss for breast cancer, but a boon for melanoma research. *Breast Cancer Res Treat* **104**, 13–19 (2007).
16. Chambers, A. MDA-MB-435 and M14 cell lines: Identical but not M14 melanoma? *Cancer Res* **69**, 5292–5293 (2009).
17. Nobukawa, B. *et al.* Breast Carcinoma Diverging to Aberrant Melanocytic Differentiation: A Case Report With Histopathologic and Loss of Heterozygosity Analyses. *Am J Surg Pathol* **23**, 1280–1287 (1999).
18. Clarke, R. Human breast cancer cell line xenografts as models of breast cancer. The immunobiologies of recipient mice and the characteristics of several tumorigenic cell lines. *Breast Cancer Res Treat* **39**, 69–86 (1996).
19. Croy, B., Linder, K. & Yager, J. Primer for Non-immunologists on Immune-Deficient Mice and Their Applications in Research. *Comparative Medicine* **51**, 300 (2001).
20. Dewan, M. Z. *et al.* Natural killer cells in breast cancer cell growth and metastasis in SCID mice. *Biomedicine & Pharmacotherapy* **59**, S375–S379 (2005).
21. Wood, K. J. & Goto, R. Mechanisms of rejection: current perspectives. *Transplantation* **93**, 1–10 (2012).

Chapter 4

4 MRI Detection of Nonproliferative Tumor Cells in Lymph Node Metastases Using Iron Oxide Particles in a Mouse Model of Breast Cancer*

4.1 Introduction

Magnetic resonance imaging (MRI) is a commonly used imaging method for tracking cells *in vivo* in preclinical models of disease. To accomplish this cells are labeled with a contrast agent prior to their injection or transplantation. Most cell tracking studies have used superparamagnetic iron oxide (SPIO) nanoparticles for cell labeling. SPIO particles disturb the static magnetic field, and this effect extends well beyond the volume of the cell, resulting in a dramatic reduction in the T2 and T2* of nearby water molecules. T2 and T2* based imaging methods depict SPIO labeled cells as pronounced local signal voids or hypointense regions¹. A variety of cell types have been studied using this approach. Examples include monitoring the fate of transplanted stem/progenitor cells in myocardial infarction^{2,3}, stroke⁴, spinal cord injury^{5,6} and multiple sclerosis⁷ and detecting the migration of dendritic cells used in cancer immunotherapy.⁸⁻¹⁰ While most studies focus on the visualization of relatively large numbers of cells even single iron-labeled cells can be detected *in vivo* by MRI.^{11,12}

Few groups have utilized iron nanoparticles and MRI to track cancer cells. This is primarily because the SPIO label is diluted over time in dividing cells leading to loss of signal and therefore loss of cell detection.¹³ However, we, and others have shown that the retention of iron particles in non-proliferative, or slowly cycling, cancer cells can be exploited to detect particular cancer cell populations.¹⁴⁻¹⁶ Heyn *et al.* demonstrated that a small percentage of brain metastatic human breast cancer cells arrest in the mouse brain and persist as distinct signal voids in a non-proliferative state, while another population of cancer cells proliferate

* This work has been previously published and is reprinted with permission from the publisher. The paper is Economopoulos, V., Chen, Y., McFadden, C., & Foster, P. J. (2013). MRI Detection of Nonproliferative Tumor Cells in Lymph Node Metastases Using Iron Oxide Particles in a Mouse Model of Breast Cancer. *Translational Oncology*, 6(3), 347-354.

and form brain metastases.¹⁴ Townson *et al.* injected iron labeled metastatic melanoma cells into the mouse liver and used MRI to show that cytotoxic chemotherapy with doxorubicin reduced liver tumor burden but did not affect the number of non-proliferative cancer cells.¹⁵ Iron-retaining cancer cells have also been observed by MRI in melanoma xenografts implanted subcutaneously in mice¹⁶; Magnitsky *et al.*, demonstrated that a small, distinct subpopulation of iron-retaining cells could be detected by flow cytometry after 20 days of *in vitro* proliferation.¹⁶ These papers all demonstrated the ability to use iron nanoparticles and MRI to image cells with a slow proliferation phenotype.

The cells these papers are targeting have been referred to as non-proliferative, quiescent, slowly cycling or dormant. Despite the diverse nomenclature the common goal of these studies has been to characterize a subpopulation of cancer cells that is believed to play a critical role in tumor progression and metastasis. Several experimental metastasis models, using a variety of cancer cell lines, show the presence of non-proliferative cancer cells, often coexisting in a metastatic site with actively growing metastases.¹⁷⁻¹⁹ In breast cancer, metastatic cancer cells can sometimes remain dormant for decades until some poorly understood trigger causes them to proliferate and progress to clinically relevant metastases.²⁰

In this paper we use this concept of label retention to examine this subpopulation of cancer cells in a murine model of breast cancer metastasis. We investigate the distribution of non-proliferative cancer cells within the primary tumor and the migration of these cells to distant lymph nodes.

4.2 Methods

4.2.1 Cell Culture and In Vitro Experiments

A green fluorescent protein (GFP) expressing transformant of the human breast cancer cell line MDA-MB-231 (231) was used. Cells were labeled with flash red fluorescent micron-sized superparamagnetic iron oxide (MPIO) particles (Excitation: 660 nm, Emission: 690 nm; Bangs Laboratories Inc., Fishers, IN). Briefly, 10⁶ cells were plated onto T75 flasks with normal complete media. After 24 hours, the media was replaced with a labeling media

containing MPIO particles at a concentration of 0.049 mg Fe/ml and cells were incubated for another 24 hours before being harvested.

To determine how MPIO particles diluted with proliferation, the cells were harvested on days 1, 2, 4, 7, 10, and 14 after addition of the labeling media (n = 3 flasks per time point). A cell sample was taken from each flask at all time points, centrifuged onto microscopy slides and stained for iron with Perls' Prussian Blue (PPB). The number of iron labeled cells and the total number of cells were counted in 5 different fields of view from each sample and the percentage of labeled cells was determined for each timepoint.

This experiment was repeated and analyzed using flow cytometry. We collected cell samples at days 1, 2, 4, 7, 10 and 14 (n = 3 flasks per time point). All analyses were performed using a LSR II flow cytometer (Becton Dickinson, Mississauga, ON). The fluorescence signal of the MPIO particles' flash red label was obtained by excitation with a 640 nm laser and detected using a filter with a 670 nm center and 30 nm band pass and 2×10^5 events were acquired. The iron content of cells at each timepoint was assessed by examining the amount of fluorescence of the MPIO particles in each sample. A sample of unlabeled 231 cells was also collected for use as a control.

4.2.2 Animal Model

5×10^5 unlabeled (n = 8) or MPIO labeled (n = 8) GFP positive 231 cells were injected into the right thoracic mammary fat pad of female CB-17 SCID (CB17/Icr-Prkdc^{scid}/IcrIcoCr1) mice aged 6-8 weeks (Charles River Canada). Animals were imaged using MRI on days 0, 7, 14, 21 and 28 after the cell injection. Mice were sacrificed either after the appearance of signal loss in MR images of either the ipsilateral axillary or brachial lymph nodes (5 of 8 mice in labeled group) or on day 28 after all imaging had been completed.

4.2.3 MRI Methods

All imaging sessions were conducted using a 1.5T CV/I MRI scanner (General Electric Medical Systems, Milwaukee, WI) along with a custom built gradient coil insert (inner diameter = 17.5 cm, maximum gradient strength = 500 mT/m, and peak slew rate = 3000 T/m/sec) and a custom built solenoid mouse body radio-frequency (RF) coil (4cm in length and 3cm in diameter). All images were acquired with a 3D balanced steady state free precession (bSSFP) pulse sequence. The bSSFP sequence was chosen because it provides very high signal to noise ratio efficiency, allowing for high-resolution image acquisitions of the whole mouse body in reasonable scan times, and because it produces very good soft tissue contrast, related to T2/T1. The scan parameters for bSSFP were as follows: repetition time = 6.7 ms, echo time = 3.3 ms, flip angle = 40°, bandwidth = +/- 31.25 kHz, matrix = 300x300, field of view (FOV) = 6 cm, 0.2 mm slice thickness, 200 micron isotropic spatial resolution, 4 signal averages (NEX), 4 RF phase cycles and scan time of 34 minutes.

4.2.4 Microscopy Methods

The left and right axillary and brachial lymph nodes and the primary tumors were removed from the animals at necropsy. The tissues were then placed in 3.75% formaldehyde in 0.1 M phosphate buffer overnight to fix the tissue. Some lymph nodes and tumors were then paraffin embedded for Perls' Prussian Blue (PPB) staining and others were placed in a sucrose gradient over the next 3 days, followed by embedding in optimal cutting temperature (OCT) compound for cryosectioning for fluorescence microscopy. Tissue samples were cut into 5- μ m sections for paraffin embedded samples and 16- μ m for frozen samples. For fluorescence microscopy, frozen lymph node sections were thawed and stained with DAPI for cell nuclei. PPB staining was performed on both frozen and paraffin embedded sections. All microscopy was performed on a Zeiss AXIO Imager (Carl Zeiss Canada Ltd.; Toronto, ON, Canada). Fluorescence images were taken using GFP, Texas Red and DAPI filters. Confocal fluorescence images were acquired on a Fluoview FV10i confocal microscope (Olympus Canada Inc., Richmond Hill, ON) using a 473-nm-wavelength laser for GFP and a 635-nm-wavelength laser for Cy5.5 excitation.

4.2.5 Image Analysis

The volume of the tumors and the left and right axillary and brachial lymph nodes were measured by manual segmentation using the OsiriX image analysis software.²¹ The axillary and brachial lymph nodes were chosen for analysis since these nodes are primarily responsible for draining the area of the mammary fat pad where the cells were injected. The OsiriX image analysis software²¹ was used to make all measurements from the images acquired in this study. Each tumor or lymph node was segmented individually on every image slice to create a series of regions of interest (ROI). The volume was then calculated by using the ROI volume calculation tool available within the software package.

Tumor maps were created that distinguished between low signal intensities generated from iron oxide particles (blue colored zone), intermediate signal intensities associated with tumor parenchyma (green colored zone) and high signal intensities related to fluid within the tumor (yellow colored zone). The image analysis program ImageJ²² was used to generate the cut off values for the low and high signal intensities.

Images of single PPB stained sections were compared with composite images of 6 individual images of PPB stained sections that were merged using the Adobe Photoshop Elements 8 software package (Adobe Systems Incorporated; San Jose, CA). Briefly, 6 images of consecutive PPB stained tissue sections were overlaid and aligned. Areas of positive staining were outlined in each section and a new image layer was created from the outlined areas, colored blue and made visible above one image of the PPB stained tissue sections.

All statistical analyses were done using the Graph Pad Prism software (GraphPad Software, Inc.; La Jolla, CA). Data were analyzed using the repeated measures Analysis of Variance (ANOVA) test, the student T-test and the non-parametric Mann-Whitney test. P-values were considered significant if they were less than 0.05.

4.3 Results

4.3.1 In Vitro Iron Dilution

231 cells were labeled *in vitro* with MPIO particles and their iron content was assessed at days 1, 2, 4, 7, 10, and 14 after labeling by counting PPB+ cells in stained cell samples or by measuring the amount of red fluorescence associated with the MPIO using flow cytometry. Cell viability after labeling (day 1 time point) was $99.2 \pm 0.6\%$. Figure 4.1 shows the PPB stained cell samples along with the quantification of the percentage of PPB-positive labeled cells detected at each time point. As the cells divided the numbers of cells that contained iron particles decreased. At days 1 and 2 after labeling $99.0 \pm 0.3\%$ and $86.0 \pm 1.4\%$ of cells were labeled. The number of labeled cells decreased to $43.1 \pm 1.6\%$ at day 4, $7.6 \pm 1.6\%$ at day 7, $1.0 \pm 0.3\%$ at day 10 and $0.8 \pm 0.3\%$ at day 14.

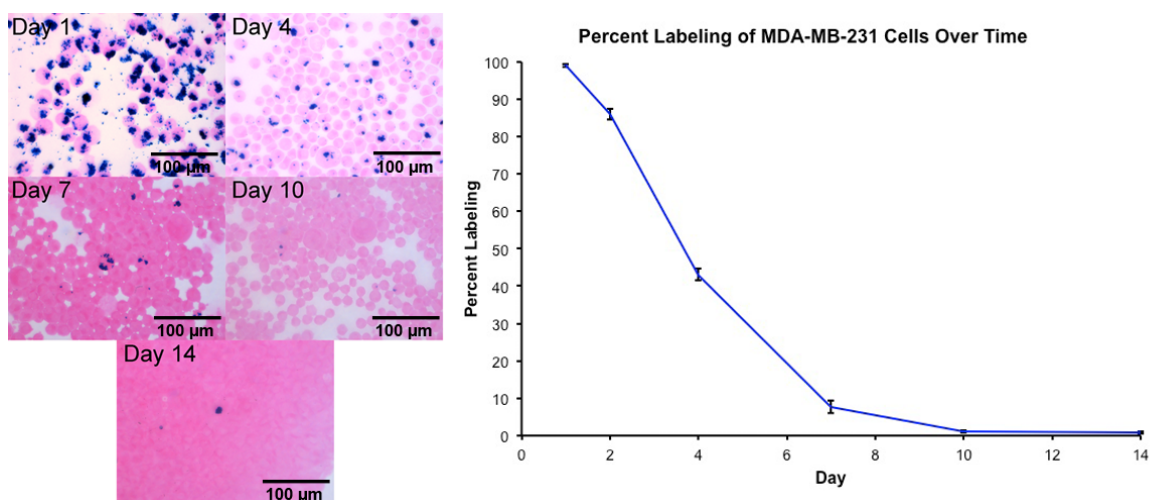


Figure 4.1 – Stained cell samples of MPIO labeled MDA-MB-231 cells at 1, 4, 7, 10, and 14 days after labeling. Graph of percentage of iron labeled MDA-MB-231 cells over time.

Similar results were observed when cells were analyzed using flow cytometry. Figure 4.2A shows the percentage of iron-labeled cells, based on the red fluorescence associated with MPIO, at each timepoint. At days 1 and 2 after labeling, $99.9 \pm 0.1 \%$ and $97.0 \pm 0.1 \%$ of cells were positive for the red fluorescent particles. The number of labeled cells decreased to $45.7 \pm 1.4 \%$ at day 4, $9.5 \pm 0.9 \%$ at day 7, $2.6 \pm 0.9\%$ at day 10 and $0.5 \pm 0.1 \%$ at day 14. Figure 4.2B shows representative dot-plots of the flow cytometry data collected for each time point. The plots display the fluorescence of the particles in the red channel on the x-axis and side scatter on the y-axis. Although the iron content diluted as cells proliferated, iron labeled cells could still be detected at 14 days after labeling.

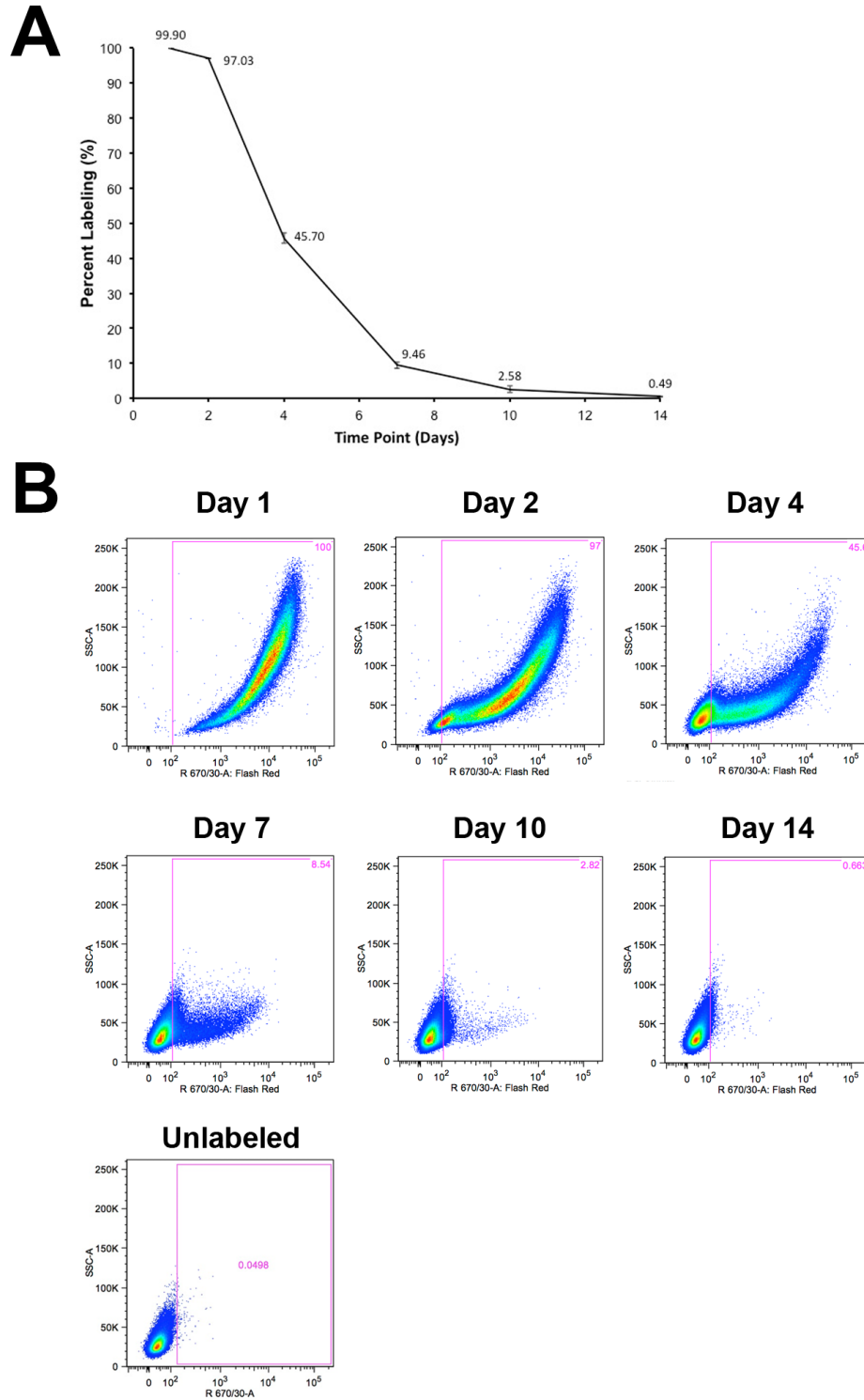


Figure 4.2 – *In vitro* dilution of MPIO particles in MDA-MB-231 cells measured by flow cytometry. (A) Graph of percentage of iron-labeled MDA-MB-231 cells over time. (B) Plots of Flash Red fluorescence intensity (x-axis) vs. side scatter (y-axis) at day 1, 2, 4, 7,

10 and 14 with gates shown for the labeled population (based on unlabeled control sample).

4.3.2 MRI of Primary Tumor

Images of iron labeled tumors (Figure 4.3A) had large, obvious areas of signal loss within the developing mass. At day 14 developing tumors appeared with mainly low signal intensity throughout. At day 21 the MRI of tumors showed regions of low signal along with regions of mixed, heterogeneous signal intensities. Images acquired on day 28 show that as the tumors became larger the regions of signal loss persisted and more of the tumor mass appeared with intermediate/high signal intensities. The images of tumors that developed from unlabeled 231 cells (Figure 4.3B) had a different MRI appearance. These tumors had a homogeneous, intermediate signal intensity at day 14 and became more heterogeneous in signal as the tumors grew in size. However, regions of hypointensity, such as observed in images of the iron-labeled tumors, were not observed in unlabeled tumors.

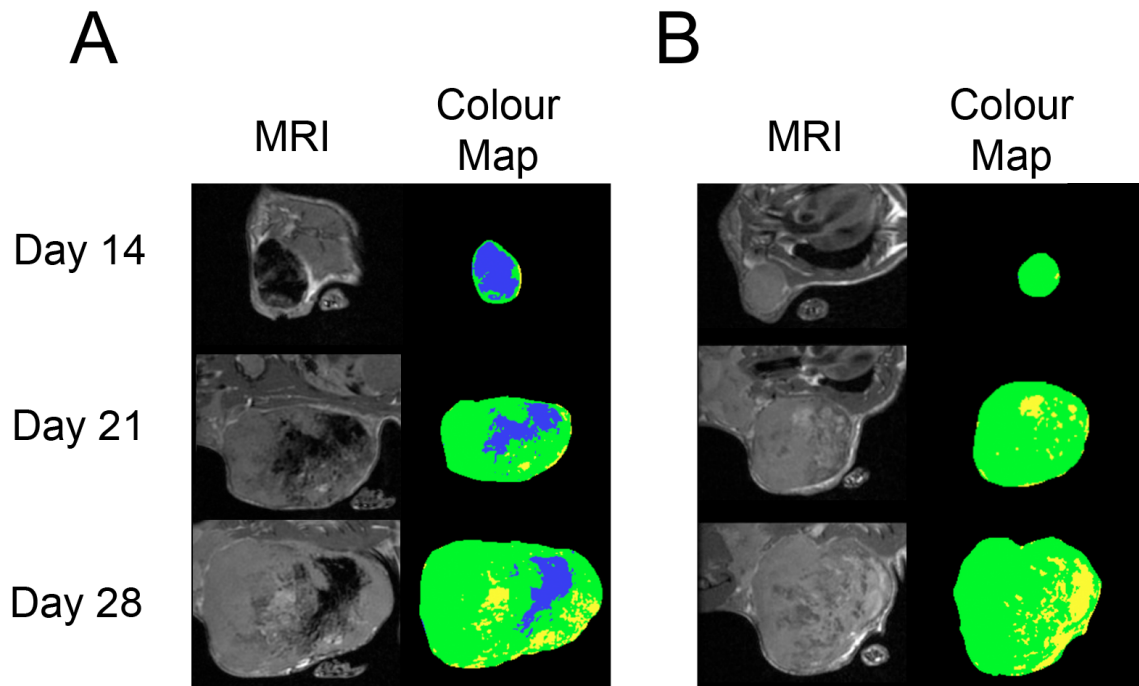


Figure 4.3 – Appearance of labeled and unlabeled tumors over time and corresponding tumor color maps. (A) The MR image and color map, respectively, of a labeled tumor

over time. (B) The MR image and color map, respectively, of an unlabeled tumor. For color maps, Blue – below low intensity cutoff (day 7 – 255, day 14 – 288, day 21 – 301, day 28 – 320), Green – between low intensity cutoff and high intensity cutoff (signal intensities of 700), Yellow – above high intensity cutoff.

Tumor color maps are shown together with the MRI to assist with visualization of the tumor borders and to highlight the three zones of signal intensities observed. The blue color represents the regions of signal hypointensity (due to iron particles), yellow represents regions of hyperintense signal (most likely due to fluid/necrosis) and the green color represents the intermediate signal intensities (the bulk of the tumor mass). There is a distinct difference in the color maps for labeled (Figure 4.3A) and unlabeled tumors (Figure 4.3B). The percentage of the total tumor volume within each of the three zones was measured for all tumors and is shown in Table 4.1. For iron-labeled tumors 91.4% of the tumor volume was composed of the low signal intensity zone (blue in color map) at the first imaging timepoint (day 7) and this decreased to 4.6% at the last imaging timepoint (day 28). In comparison, 1% or less of the volume of unlabeled tumors fell within this zone at any timepoint. The percent of the tumor volume within the low signal intensity zone was compared between labeled and unlabeled groups at each time point using a Mann-Whitney test. Significant differences were found at all times (day 7, $p = 0.004$; day 14, $p = 0.0007$; day 21, $p = 0.0095$; day 28, $p = 0.0238$). There was no significant difference in total tumor volume between the iron labeled and unlabeled tumors at any imaging time point.

Table 4.1 – Tumor volume and percent of tumor volume in tumor color map zones. Blue zone is below low intensity cutoff (signal intensity of 255), green zone is between low intensity cutoff and high intensity cutoff (signal intensity of 700), and yellow zone is above high intensity cutoff.

	Percentage in Blue Zone		Percentage in Green Zone		Percentage in Yellow Zone		Tumor Volume (mm ³)	
	Labeled Tumors	Unlabeled Tumors	Labeled Tumors	Unlabeled Tumors	Labeled Tumors	Unlabeled Tumors	Labeled Tumors	Unlabeled Tumors
Day 7	91.4 ± 15.0	0.5 ± 0.4	7.8 ± 13.1	98.2 ± 1.0	0.8 ± 1.9	1.3 ± 0.9	16.3 ± 7.3	10.2 ± 4.7
Day 14	81.4 ± 6.8	0.4 ± 0.5	17.5 ± 6.1	98.5 ± 0.6	1.2 ± 1.1	1.0 ± 0.8	169.9 ± 81.9	158.5 ± 90.4
Day 21	12.1 ± 6.1	0.1 ± 0.05	85.2 ± 6.6	88.7 ± 7.0	2.7 ± 0.8	11.4 ± 7.0	839.9 ± 496.2	1003.7 ± 443.5
Day 28	3.4 ± 2.4	0.1 ± 0.02	87.7 ± 7.5	85.2 ± 5.1	9.0 ± 5.1	14.8 ± 5.1	1994.5 ± 661.1	2574.7 ± 891.0

4.3.3 Histology of Primary Tumor

Tumors were sectioned and stained for iron with PPB. Figure 4.4 depicts a tumor generated from MPIO labeled 231 cells at day 14 after injection. Figure 4.4A, D and F show a single 16- μm PPB stained section of the tumor at increasing magnification. These sections show the presence of iron-labeled cells within the tumor. Figure 4.4B and E are merged images of 6 consecutive PPB stained sections showing the summed iron content of all 6 sections. The data is presented this way to illustrate the conundrum of comparing 16- μm stained tissue sections with 200 μm MRI slices. A total of 12 tissue sections like these would have to be merged perfectly for a true representation of the extent of iron-labeled cells contained in the image slice. Overall, all tumors contained iron-labeled cells distributed throughout the tumor mass.

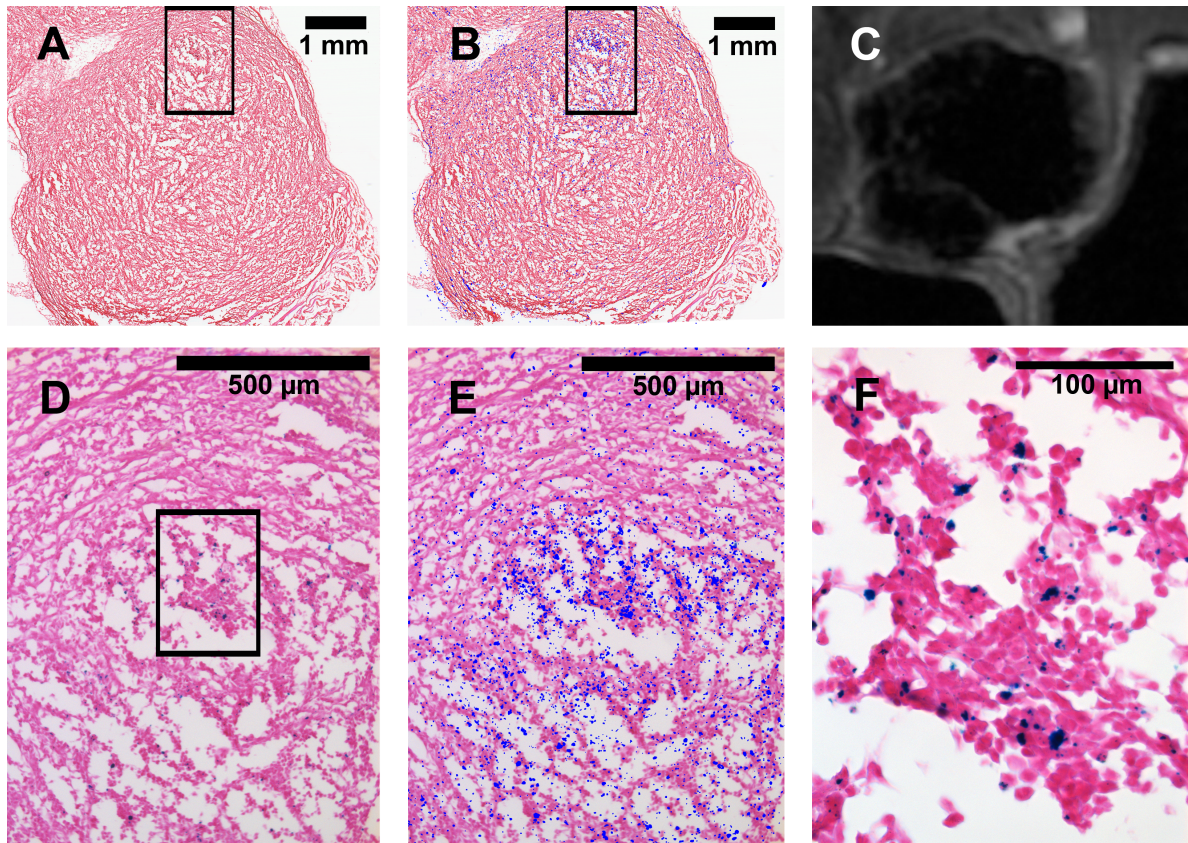


Figure 4.4 – PPB stained section of labeled tumor at day 14. (A) PPB stained section of tumor lobe. (B) PPB stained section showing the iron content from 6 consecutive sections (blue areas). (C) MR image of tumor. (D) PPB stained section of tumor from area outlined by box in (A). (E) PPB stained section showing the iron content from 6 consecutive sections (blue areas), from area outlined by box in (B). (F) PPB stained section of tumor from area outlined by box in (D).

4.3.4 Detection of Regions of Signal Loss in Lymph Nodes

Of particular interest was the observation of regions of signal loss in images of the draining lymph nodes, in 6/8 mice that received MPIO labeled 231 cells. Figure 4.5 shows a representative image of an ipsilateral axillary lymph node at day 14 with a focal region of signal loss (A, arrow) and the corresponding PPB stained sections (B,C). The MRI and histology showed good correspondence. In this example signal loss was observed on one side

of the node and the most intense PPB staining was located in the same location. Fluorescence microscopy was used to validate the presence of MPIO+ cancer cells within nodes.

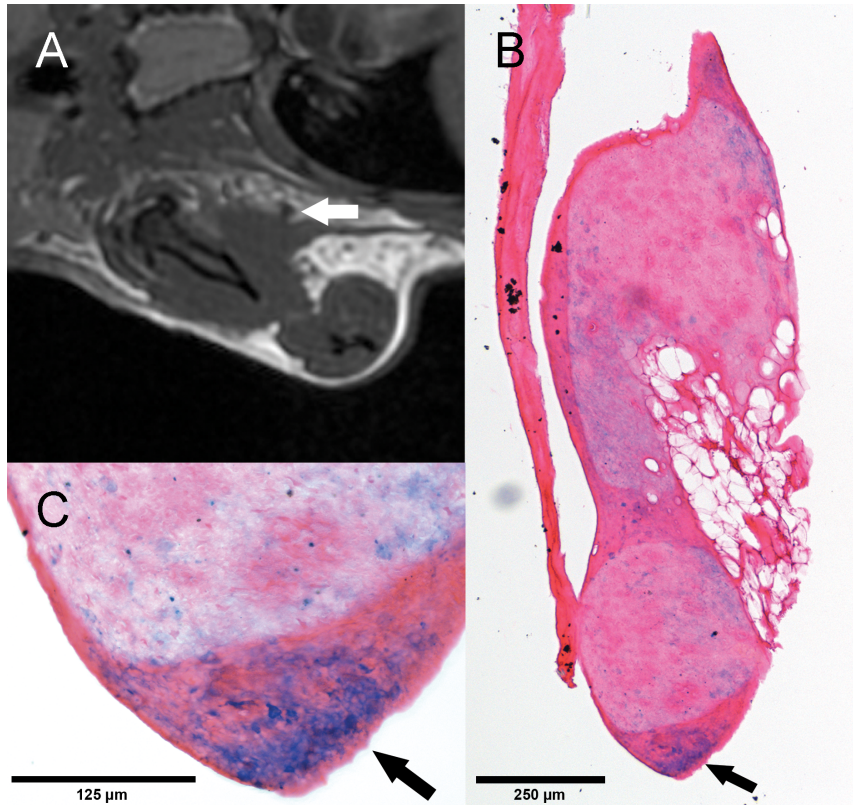


Figure 4.5 – MRI and iron staining of an ipsilateral axillary lymph node 14 days after iron-labeled breast cancer cells were implanted into the thoracic mammary fat pad in CB17 SCID mice. (A) Cropped bSSFP image of thorax region of mouse reveals a region of signal loss in the ipsilateral axillary node (arrow). (B) Section of lymph node stained with Perls' Prussian Blue for iron detection at x10 magnification shows iron positive cells in the area of the node corresponding to the signal loss in the MR image (arrow). (C) Iron positive area of the node at x40 magnification, where strong staining can be seen (arrow) suggesting that cancer cells have retained iron particles after migrating to the node.

In Figure 4.6 an ipsilateral axillary node which showed a region of signal loss at day 28 (A) was found to contain GFP+ cells (B) and regions of red fluorescence (C) that were co-localized (D), indicating the presence of iron-labeled cancer cells in the node. Confocal microscopy was also performed on some lymph nodes (Figure 4.7). Tissue sections were imaged with GFP and Cy5.5 fluorescence. Confocal image overlays of an ipsilateral axillary lymph node at 28 days after the 231 cell injection clearly show the presence of a number of GFP+ cells, which contain red fluorescent particles, located in the node. This data also indicates that the cancer cells have retained the MPIO label after migrating from the tumor to the node.

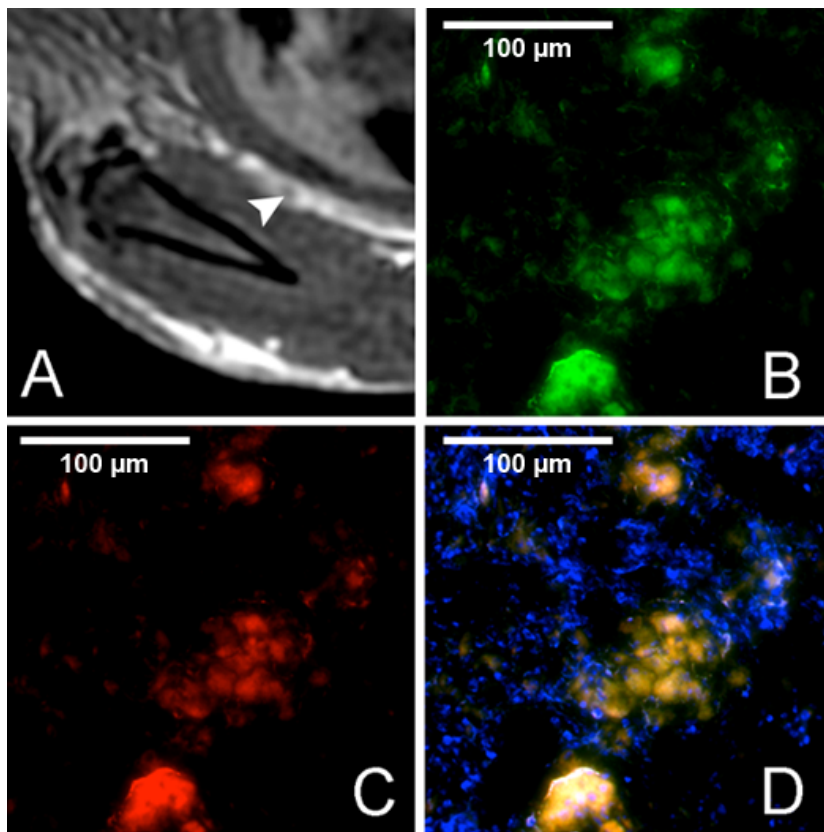


Figure 4.6 – MRI and Fluorescence microscopy of a representative SCID mouse ipsilateral axillary lymph node 28 days after tumor cell implantation. CB17 SCID mice were injected with GFP positive MDA-MB-231 cells labeled with red fluorescent iron oxide particles. (A) Cropped bSSFP MRI image of the ipsilateral axillary lymph node

shows a region of signal loss within the node (arrowhead). (B) GFP positive cancer cells found within node correspond with (C) red fluorescent MPIO particles. (D) Overlay of GFP fluorescent cells, red fluorescent MPIO and DAPI stain for cell nuclei. Cells that are positive for both GFP and contain red fluorescent particles can be found within the node, confirming the presence of iron labeled cancer cells.

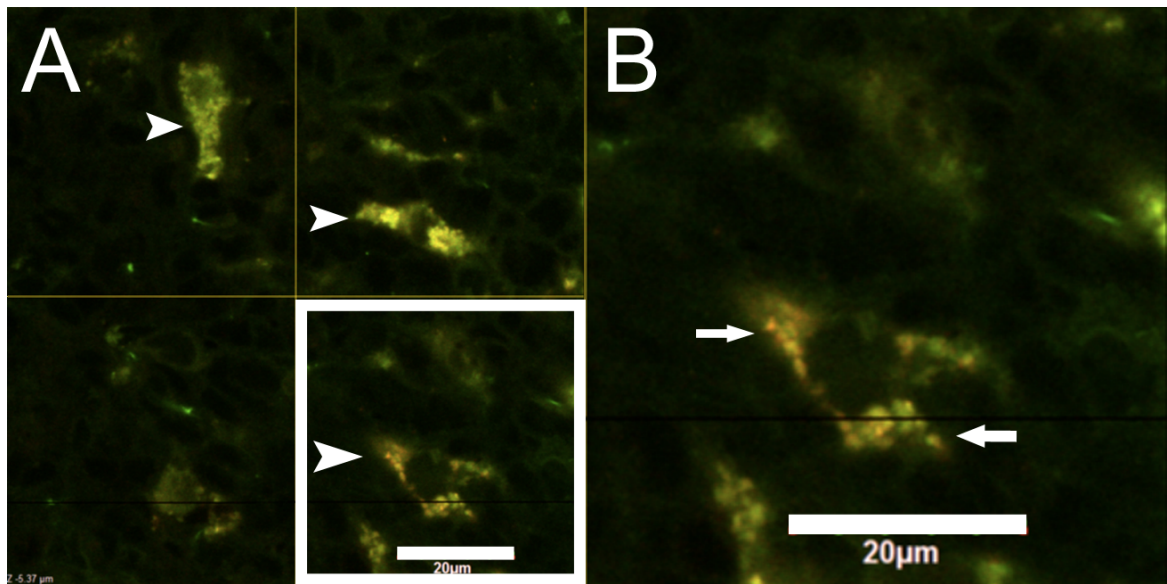


Figure 4.7 – Confocal microscopy image of MPIO labeled MDA-MB-231 cells in an ipsilateral axillary lymph node 28 days after tumor cell implantation. (A) Image at 60x magnification. Area in white box has been enlarged (B) to show the localization of MPIO particles (red) in the cells (green).

Fluorescence microscopy images of the lymph node sections also revealed that areas of green and red fluorescence did not always overlap. Occasionally, red fluorescent areas were found that correlated with DAPI staining for cell nuclei but not with areas of green fluorescence (data not shown). This suggests that the red fluorescent iron particles can be found in other cell types within the lymph node and may represent bystander cell uptake of iron associated with dead tumor cells.

Tables 4.2 and 4.3 summarize the analysis of axillary (Table 4.) and brachial (Table 4.) lymph nodes that were examined with both MRI and microscopy. The time point that each node was examined at is also included in these tables. Table 4. shows that 5/6 axillary lymph nodes were positive for signal loss in MR images and that the presence of iron-labeled cells was confirmed for all 5 nodes, with either PPB staining or fluorescence microscopy. One axillary node did not have signal loss within it in (was MRI negative), however, fluorescence microscopy revealed cells in the node that were both GFP and red-MPIO positive. The sensitivity of detection of signal loss by MRI due to iron-labeled cells in the axillary nodes was therefore 83%.

Table 4.2 – Analysis of axillary lymph nodes examined with both MRI and either PPB staining or fluorescence microscopy (PPB = Perl’s Prussian Blue, FL = Fluorescence Microscopy)

Axillary Lymph Node	Signal Loss in MR Images	Positive in Microscopy (Positive PPB Staining or GFP and Red-MPIO Positive Cells)	Time Point Removed
1	Yes	Yes – PPB	Day 14
2	Yes	Yes – PPB	Day 14
3	Yes	Yes – FL	Day 14
4	Yes	Yes – FL	Day 21
5	No	Yes – FL	Day 14
6	Yes	Yes – FL	Day 28

Table 4. shows that 2 of 5 brachial lymph nodes were positive for signal loss on MRI; iron-labeled cells were detected by PPB staining in both of these nodes. For 3 brachial lymph nodes no signal loss was detected by MRI even though the fluorescence microscopy for all 3 of these nodes showed cells that were both GFP and red-MPIO positive. The sensitivity of detection of signal loss by MRI due to iron-labeled cells in the brachial lymph node was only 40%.

Table 4.3 – Analysis of brachial lymph nodes examined with both MRI and either PPB staining or fluorescence microscopy (PPB = Perl’s Prussian Blue, FL = Fluorescence Microscopy)

Brachial Lymph Node	Signal Loss in MR Images	Positive in Microscopy (Positive PPB Staining or GFP and Red-MPIO Positive Cells)	Time Removed	Point
1	Yes	Yes – PPB	Day 14	
2	Yes	Yes – PPB	Day 14	
3	No	Yes – FL	Day 14	
4	No	Yes – FL	Day 21	
5	No	Yes – FL	Day 28	

4.4 Discussion

The goal of this study was to investigate the potential for tracking metastatic cancer cells using iron oxide nanoparticles and MRI. We have demonstrated that the retention of iron particles in some cancer cells allows for their long-term tracking *in vivo*. Previously we studied the fate of iron-labeled cancer cells in a model of breast cancer metastasis to the brain¹⁴ and in a model of melanoma metastasis in the liver.¹⁵ In those models cancer cells were delivered to the organ of interest (brain or liver) by systemic injection (intracardiac left ventricle or intrahepatic vein) to mimic the hematogenous spread of metastatic cancer cells. In the current study we have used an orthotopic model of breast cancer and have examined the draining lymph nodes for metastasis.

Cell tracking with MRI and magnetic nanoparticles has not been widely applied to study cancer cells because the iron label is diluted during cell division. Since the detection of iron-labeled cells by MRI relies on the total iron content, this means that eventually the cancer cells will not contain enough iron to be detected as signal voids in MR images. Early *in vitro* studies by Arbab *et al.* showed that mesenchymal stem cells, which are slowly dividing cells in culture, retained SPIO particles for up to 7 weeks post cell labeling while iron-labeled cancer cells (HeLa) lost their iron label by 2-3 weeks post cell labeling.²³ We have previously reported the dilution of SPIO in fast growing mouse melanoma (B16F10) cancer cells to below MR detectable levels in only 4-5 days post cell labeling.²⁴ In the current study both the analysis of PPB stained cells in stained cell samples and the flow cytometric analysis showed that *in vitro* by day 4 post cell labeling the number of MPIO labeled 231 cells was under 50%, and that this declined to less than 5% at day 10 post labeling. Still, at 14 days (~ 14 cell divisions) post labeling a very small proportion of the cancer cells retained the iron label. This finding is in agreement with a study by Magnitsky *et al.* who detected a small population of MPIO-retaining human melanoma cells (~1%) at day 20 post cell labeling (~ 17 cell divisions). They also used demonstrated a correlation between iron-retaining cells and expression of JARID1B, a biological marker of slow cycling cells.¹⁶

Our *in vivo* MRI data also shows that not all cancer cells lose the iron label over time; indicating that not all cancer cells undergo extensive proliferation. This is perhaps expected

since solid tumors are known to have pronounced heterogeneity; with different subpopulations of cancer cells (and normal stromal cells) co-existing. The list of characteristics by which these subpopulations differ is extensive but includes cellular morphology, receptors, enzymes, growth rates and gene expression, to name a few.²⁵ Marked differences in the proliferation behavior of tumor cells within a single cancer are typical.²⁵ Some cells are nonproliferative and others are cycling but this can occur at various rates and, at any given time, cycling cells within the tumor will be at different stages of the cell cycle.

MRI of the primary mammary fat pad tumors showed that the iron-labeled cells (blue zone) encompass the whole tumor in the first two weeks and then, as the tumor volume increases, makeup less of the tumor mass and appear to remain located together in one region of the tumor. Since sister cells have been shown to remain contiguous in solid tumors, sublines tend to be localized regionally or zoned.²⁶⁻²⁸ Therefore, the zone of iron-retaining cells within these tumors may reflect the presence of a specific subpopulation.

The ability to detect iron-labeled 231 cells in the ipsilateral axillary and brachial lymph nodes after implantation of these cells in the mammary fat pad is intriguing. Since we rarely observed GFP+ cancer cells in the nodes that were not also red fluorescent our data suggests that there may be a relationship between the iron-retaining cell population and an invasive or metastatic phenotype. This is the first paper to demonstrate the migration of iron-labeled cancer cells from a primary tumor using MRI. The sensitivity of detecting signal loss by MRI due to the presence of iron-labeled cancer cells was found to be 83% for the axillary node and 40% for the brachial node. This is likely because the axillary nodes in the mouse are easier to visualize in the MR images than the brachial nodes because the axillary node sits in a more prominent fat pad, which generates very good image contrast in bSSFP images (fat is bright, node tissue is intermediate).

Our data suggests that non-proliferative, or slowly-cycling, cancer cells can be detected by *in vivo* MRI. Non-proliferative cancer cells, sometimes referred to as dormant cells, are believed to contribute to tumor recurrence. Clinical dormancy is reflected by relapses at distant sites after the original primary cancer diagnosis. In some tumors, for example breast cancer, melanoma and renal cancer, these recurrences are common and can occur many years after diagnosis.²⁹ Dormant cancer cells also present a substantial therapeutic problem; since

they are quiescent they are non-responsive to current therapies which target proliferating cells.¹⁶⁻¹⁸ Discerning the mechanisms that either maintain prolonged cellular dormancy or activate dormant tumor cells to a proliferative state has been a recognized goal of scientists worldwide. Still, relatively little is known about dormant cancer cells and studying these cells is challenging since at the present time there are no suitable *in vivo* assays. It is exciting to consider that advanced *in vivo* cellular imaging techniques, as described in this paper, may be used to study the fate of distinct subpopulations of metastatic breast cancer cells within the whole tumor in the intact mouse body.

4.5 References

1. Modo, M., Hoehn, M. & Bulte, J. W. M. Cellular MR Imaging. *Mol Imaging* **04**, 143–164 (2005).
2. Yang, K. *et al.* Magnetic resonance evaluation of transplanted mesenchymal stem cells after myocardial infarction in swine. *Can J Cardiol* **27**, 818–25 (2011).
3. Yao, Y. *et al.* In vivo magnetic resonance imaging of injected endothelial progenitor cells after myocardial infarction in rats. *Mol Imaging Biol* **13**, 303–13 (2011).
4. Daadi, M. M. *et al.* Molecular and magnetic resonance imaging of human embryonic stem cell-derived neural stem cell grafts in ischemic rat brain. *Mol Ther* **17**, 1282–91 (2009).
5. Jendelová, P. *et al.* Magnetic resonance tracking of transplanted bone marrow and embryonic stem cells labeled by iron oxide nanoparticles in rat brain and spinal cord. *J Neurosci Res* **76**, 232–43 (2004).
6. Gonzalez-Lara, L. E. *et al.* The use of cellular magnetic resonance imaging to track the fate of iron-labeled multipotent stromal cells after direct transplantation in a mouse model of spinal cord injury. *Mol Imaging Biol* **13**, 702–11 (2011).
7. Kim, H., Walczak, P., Muja, N., Campanelli, J. T. & Bulte, J. W. M. ICV-transplanted human glial precursor cells are short-lived yet exert immunomodulatory effects in mice with EAE. *Glia* **60**, 1117–29 (2012).
8. Dekaban, G. A. *et al.* Semiquantitation of Mouse Dendritic Cell Migration In Vivo Using Cellular MRI. *J Immunother* **32**, 240–251 (2009).
9. Zhang, X. *et al.* Cellular magnetic resonance imaging of monocyte-derived dendritic cell migration from healthy donors and cancer patients as assessed in a scid mouse model. *Cytotherapy* **13**, 1234–1248 (2011).

10. De Vries, I. *et al.* Magnetic resonance tracking of dendritic cells in melanoma patients for monitoring of cellular therapy. *Nat Biotechnol* **23**, 1407–1413 (2005).
11. Heyn, C. *et al.* In vivo magnetic resonance imaging of single cells in mouse brain with optical validation. *Magn Reson Med* **55**, 23–9 (2006).
12. Shapiro, E. M., Sharer, K., Skrtic, S. & Koretsky, A. P. In vivo detection of single cells by MRI. *Magn Reson Med* **55**, 242–9 (2006).
13. Walczak, P., Kedziorek, D. a, Gilad, a a, Barnett, B. P. & Bulte, J. W. M. Applicability and limitations of MR tracking of neural stem cells with asymmetric cell division and rapid turnover: the case of the shiverer dysmyelinated mouse brain. *Magn Reson Med* **58**, 261–9 (2007).
14. Heyn, C. *et al.* In vivo MRI of cancer cell fate at the single-cell level in a mouse model of breast cancer metastasis to the brain. *Magn Reson Med* **56**, 1001–10 (2006).
15. Townson, J. L. *et al.* Three-dimensional imaging and quantification of both solitary cells and metastases in whole mouse liver by magnetic resonance imaging. *Cancer Res* **69**, 8326–31 (2009).
16. Magnitsky, S., Roesch, A., Herlyn, M. & Glickson, J. D. In vivo and ex vivo MR imaging of slowly cycling melanoma cells. *Magn Reson Med* **66**, 1362-1373 (2011).
17. Naumov, G. N. *et al.* Persistence of Solitary Mammary Carcinoma Cells in a Secondary Site: A Possible Contributor to Dormancy. *Cancer Res* **62**, 2162–2168 (2002).
18. Luzzi, K. J. *et al.* Multistep nature of metastatic inefficiency: dormancy of solitary cells after successful extravasation and limited survival of early micrometastases. *Am J Pathol* **153**, 865–73 (1998).
19. Cameron, M. D. *et al.* Temporal Progression of Metastasis in Lung: Cell Survival, Dormancy, and Location Dependence of Metastatic Inefficiency. *Cancer Res* **60**, 2541–2546 (2000).

20. Goss, P. E. & Chambers, A. F. Does tumour dormancy offer a therapeutic target? *Nat Rev Cancer* **10**, 871–7 (2010).
21. Rosset, A., Spadola, L. & Ratib, O. OsiriX: an open-source software for navigating in multidimensional DICOM images. *J Digit Imaging* **17**, 205–16 (2004).
22. Abràmoff, M. D., Magalhães, P. & Ram, S. J. Image Processing with ImageJ. *Biophotonics International* **11**, 36–42 (2004).
23. Arbab, A. S. *et al.* Characterization of biophysical and metabolic properties of cells labeled with superparamagnetic iron oxide nanoparticles and transfection agent for cellular MR imaging. *Radiology* **229**, 838–46 (2003).
24. Foster, P., Dunn, E., Karl, K., Snir, J. & CM Cellular magnetic resonance imaging: in vivo imaging of melanoma cells in lymph nodes of mice. *Neoplasia* **10**, 207–216 (2008).
25. Heppner, G. H. Tumor heterogeneity. *Cancer Res* **44**, 2259–65 (1984).
26. Fidler, I. J. & Hart, I. R. Biological and experimental consequences of the zonal composition of solid tumors. *Cancer Res* **41**, 3266–7 (1981).
27. Hakansson, L. & Trope, C. On the presence within tumours of clones that differ in sensitivity to cytostatic drugs. *Acta Pathol Microbiol Scand Suppl Sect A* **82**, 35–40 (1974).
28. Prehn, R. T. Analysis of Antigenic Heterogeneity Within Individual 3-Methylcholanthrene-Induced Mouse Sarcomas. *J Natl Cancer Inst* **45**, 1039–1045 (1970).
29. Uhr, J. W. & Pantel, K. Controversies in clinical cancer dormancy. *Proc Natl Acad Sci U S A* **108**, 12396–12400 (2011).

Chapter 5

5 Conclusions and Future Work

5.1 Conclusions

Breast cancer is a devastating disease that causes the second highest number of cancer patient deaths in Canada.¹ Many different models of breast cancer exist with new methods being applied to the study of these models in order to gain greater insight to the progression of tumors and the development of metastases. Advances in MRI imaging allow high-resolution images of the entire mouse body to be acquired in a reasonable amount of time with excellent contrast, making this modality well suited for studying breast cancer progression in vivo. With the application of MRI to the study of breast tumor progression, the effect of the model itself on the ability to use MRI for monitoring tumor and metastasis development needs to be evaluated. Lymphatic metastases are an indicator of the amount of dissemination that may have already occurred in a patient.² There is however disagreement on the specific details of what would be considered a metastatic lesion. Some believe that the presence of single cancer cells in the lymph node is not a significant finding, while others argue that this is highly significant.² More work is needed to gain a better understanding of lymphatic metastases and the role that they play in disease progression and overall metastatic dissemination. The work presented in this thesis hopes to provide a platform for further metastasis research and begin to define the functional phenotype of the metastatic cell. The following sections summarize the work completed and propose future directions that this work can follow.

5.1.1 Chapter 2

Immunodeficient mice are commonly used as recipients of human cancer cells in xenograft models of tumor progression and metastasis. MRI is becoming a widely used tool for noninvasively monitoring tumor growth in vivo in these preclinical investigations. In this paper, we performed the first study of the normal MRI appearance and size of the lymph nodes and spleen in healthy, immune-compromised (nude, SCID and NOD/SCID IL-2R null)

and wild type (C57Bl/6) mice and examined how residual innate immunity influences the appearance of these lymphoid organs. Our main findings were:

1. Lymph nodes in nude and less frequently in SCID mice contained a hyperintense region visible on MRI images.
2. There were no lymph nodes that could be detected in NOD/SCID IL-2R null mice using high-resolution MRI.
3. The MRI appearance and size of nodes in nude mice were highly variable.
4. Nodes in SCID mice were smaller than in nude or C57Bl/6 mice.
5. Over time, and with repeated MRI, the lymph node volumes changed slightly in all strains.

Overall, the MRI appearance of the normal lymph nodes and spleen varies considerably in the mouse strains examined in this study. This is important to recognize in order to avoid misinterpreting MRI findings as abnormal when these strains are used in MRI studies.

5.1.2 Chapter 3

In this chapter, we compared the ability of two different tumor cell lines, MDA-MB-231 and MDA-MB-435, to grow and metastasize to the regional lymph nodes in both nude and SCID mice using high resolution MRI. The major findings in this study were:

1. Tumors generated from MDA-MB-231 cells were significantly larger than those from the MDA-MB-435 cells, regardless of the strain.
2. The overall incidence of metastases was the same between both nude and SCID mice injected with MDA-MB-231 cells; some of the SCID mice developed metastases in more than one lymph node.
3. The high variability of nude mouse lymph nodes impact the classification of nodes as metastatic or non-metastatic when based on volume measurements.
4. Lymph node volumes obtained from MRI data can be predictive of metastases, with the greatest accuracy in SCID mice injected with MDA-MB-231 cells.

In general, the strain of mouse that is used can impact the detection of lymph node metastases when using MRI. From this study, we found that SCID mice bearing MDA-MB-231 tumors would provide the best model for studying for spontaneous lymph node metastases using MRI.

5.1.3 Chapter 4

Cell tracking with MRI and iron nanoparticles is commonly used to monitor the fate of implanted cells in preclinical disease models. Few studies, however, have employed these methods to study cancer cells because proliferative iron-labeled cancer cells will lose the label as they divide. In this chapter, we evaluated the potential for retention of the iron nanoparticle label, and resulting MRI signal, to serve as a marker for slowly dividing cancer cells. Green fluorescent protein–transfected MDA-MB-231 breast cancer cells were labeled with red fluorescent MPIO particles. Cells were examined *in vitro* at multiple time points after labeling by staining for iron-labeled cells and by flow cytometric detection of the fluorescent MPIO. SCID mice were implanted with MPIO-labeled or unlabeled cells in the mammary fat pad and MRI was performed weekly until 28 days after injection.

The main findings were:

1. MPIO retaining 231 breast cancer cells can be detected both *in vitro* and *in vivo*.
2. MPIO retaining 231 cancer cells were detected in the primary tumor for up to 28 days with MRI.
3. MPIO retaining cells were detected in the draining lymph nodes by MRI as early as 14 days and up to 28 days post cell implantation.

Our data suggest an interesting role for cell tracking with iron particles since label retention leads to persistent signal void, allowing proliferative status to be determined. The data also suggests that the MPIO retaining phenotype may play a role in metastatic dissemination and survival. The most exciting finding from this study was that a specific subpopulation of cancer cells, non-proliferative cancer cells, could be monitored *in vivo* over time.

The work presented in the first two chapters of this thesis demonstrate the influence of strain differences on lymphoid organ structure and that these differences impact growth and metastasis in xenograft tumor models. The SCID mouse and MDA-MB-231 tumor model from chapter 3 laid the foundation for the work in chapter 4 which demonstrated that MPIO retaining, or slowly cycling cancer cells could be detected in vivo using cellular MRI and were found within the draining lymph nodes of tumor bearing animals. We believe that the model and technique described in this thesis can be used to further grow our understanding of lymphatic metastases and the role that slowly cycling tumor cells may play in the progression of cancer, dormancy and disease recurrence.

5.2 Future Work

The work presented in this thesis has provided answers to some questions, but has also brought about new research questions and the opportunity to build upon what this work has already demonstrated. The following sections describe future work that can be conducted to further optimize the techniques described, gain a greater understanding of the properties and behavior of the cancer cell populations and examine how the mouse strain would affect metastasis to other organs.

5.2.1 Optimizing the Detection of MPIO Retaining Tumor Cells in MRI

Several things could be done to improve the detection of the MPIO retaining tumor cells, as demonstrated in Chapter 4. First, it may be possible to further increase the iron content of the implanted cancer cells by modifying the labeling techniques. This could be accomplished by changing the concentration of the MPIO particles in culture, the duration of the labeling phase or by using a transfection agent to increase the uptake. It would be important to not have cells contain so much iron that it would impact the cell viability or functionality.

Another option would be to investigate MPIO particles with different coatings to see if the coating has an effect on the uptake of the particles and their retention long term. Several studies have also used SPIO particles to detect label retaining colorectal carcinoma and

melanoma cells^{3,4}, however these particles may not be as effective for tracking metastases as they may be degraded by the cells over time,⁵ typically have lower iron loading per cell⁶ and usually have a lower R2 value.⁵

Imaging parameters could also be further optimized. Phantoms containing MPIO labeled cells that have been allowed to dilute prior to the construction of the phantoms could be used to determine the concentration of iron per cell needed for detection or the amount of cell division that can occur before a cell would be undetectable. These phantoms could also be used to optimize the pulse sequence parameters to increase the sequence's sensitivity. The bSSFP pulse sequence that was used in this study is highly sensitive to iron. However, the signal loss produced by iron in low concentrations can be difficult to detect. Using a different pulse sequence that would either provide positive contrast, such as an ultrashort TE sequence, or using other techniques that would increase the sensitivity such as T2 or T2* maps may improve the detection of the MPIO retaining cells. Also, conducting this experiment using a higher field strength would increase the sensitivity to the MPIO retaining cells as well as allowing for improved image quality and potentially shorter acquisition times.

5.2.2 Demonstrating Metastasis formation from Disseminated MPIO Labeled Cells

The work presented in chapter 4 only examined the tumor growth up to 28 days following cell injection and animals were sacrificed after the appearance of signal loss in the lymph nodes. The study design did not allow for development of macroscopic metastases in lymph nodes. It would be interesting to determine if MPIO retaining cancer cells detected within lymph nodes can go on to proliferate and form macrometastases. It would also be interesting to compare the number of MPIO retaining cancer cells that generate metastases in the spontaneous model to the number of cancer cells that form metastases in an experimental model to determine if the models are consistent or if there are differences between these types of models.

This type of study would require that the primary tumor be removed to allow the mice to survive longer. Alternatively a different cell line could be used if it was known to have a slower growth rate and to form frequent metastases.

5.2.3 Correlating MPIO Retention With Standard Label Retention Techniques and Determining Phenotype of MPIO Retaining Tumor Cells

Many studies of stem cells and tumor initiating cells use standard label retention assays to examine the functional properties of these cells, including BrdU, EdU and CFSE.⁷⁻¹¹ The retention of these compounds is considered a hallmark of cells with stem-like properties.¹¹

Examining the way these compounds are retained and comparing them directly to MPIO retention will allow us to determine if MPIO retention is in fact a good indicator of cells possessing a stem-like phenotype. This can be achieved by co-labeling cells with MPIO and one of the other compounds and comparing the dilution of both labels over time using flow cytometry. This initial *in vitro* work could then be transferred to an *in vivo* model using the same model described in chapter 4 to determine if the behavior of the cells remains the same or changes in some way.

Previous studies have shown that tumor cells that retain labels, such as BrdU or EdU and CFSE, are therapy resistant, utilize asymmetric cell division to maintain the slowly cycling population, and are able to initiate tumors and form metastases.⁹ The MPIO retaining cancer cells that we have tracked in this thesis may possess the same characteristics. These cells could be examined *in vitro* to determine their phenotype.

In vitro video microscopy could be used to track the division of MPIO and BrdU labeled cells to determine if asymmetric cell division is occurring and if it correlates with MPIO retention.

A tumorsphere assay could also be conducted where tumor cells are sorted into MPIO retaining and non-retaining samples using flow cytometry and then grown in serum free conditions that promote spheroid formation.¹¹⁻¹³ If the MPIO retaining population is able to

consistently form spheroids, this would indicate that these cells possess stem-like characteristics. Flow cytometry could also be used to determine if there is a particular surface marker phenotype that would differentiate the MPIO retaining cells from the non-retaining cells¹³, potentially allowing mechanisms for this population's behavior to be discovered.

In vivo tumorigenicity assays would allow us to determine if the MPIO retaining phenotype is tumorigenic. Limiting dilutions of the MPIO retaining and non-retaining cells would allow the extent of the tumor forming capacity of the MPIO retaining population to be determined.

5.2.4 Effect of Treatment and Modified Gene Expression on MPIO Retaining Cells

The MPIO retaining cancer cells that were detected in Chapter 4 in the primary tumor have been shown by others to be resistant to chemotherapy in experimental metastasis models.¹⁴ Other studies have shown that slowly cycling cells detected by CFSE are also chemotherapy resistant.⁸

The efficacy of a treatment could be evaluated in our model, allowing the treatment's effect on MPIO retaining cells within the primary tumor to be determined. It would be important to determine if treatment caused only tumor debulking with retention of MPIO, depicted as a signal void volume, that slowly declined over time due to continued cell division, or if a greater percentage of cells will be triggered to retain MPIO by cycling much slower, creating a signal void volume that may remain constant for the duration of the treatment. It would also be interesting to determine if treatment would impact metastatic dissemination in our model. Previous studies have shown resistance to therapy^{8,14}, but have not shown if there is an impact, whether positive or negative, on this population's ability to disseminate to distant sites.

5.2.5 Examine Effect of Strain on Metastases to Other Organs and In Different Tumor Types

In chapter 3, the focus was on the effect of the differing immune deficits of the two strains on the ability of breast tumors to grow and metastasize to regional lymph nodes. This model could be expanded to examine other organs such as the liver, lungs, bone and brain, which are common sites of metastasis in breast cancer.¹⁵ We believe that mice with greater immune deficits will exhibit higher rates of metastasis and will also have a higher occurrence of multiple metastatic lesions in more distant organs. Xie et al. have examined the effect of immune deficit on distant organ metastases in different tumor types and have found that this relationship does exist.¹⁶ There are other factors in the animals' genetic background that may also play a role in the development of the primary tumor and metastases. Kubota et al. compared the doubling times of different tumor cell lines in both nude and SCID mice, finding that the doubling time on average is faster in the SCID mice, but some cell lines had slower growth in this strain compared to the nude mice.¹⁷

However, some technical challenges do exist in trying to use our particular model with our current system, as the volume of tumors generated from the 231 cell line becomes extremely large by the final imaging time point and are almost too large to fit within the MR coil used for imaging. This model would need to be modified to allow the development of metastases in other organs without having the tumor reach a size that would impede imaging.

This could be done by either using a different cell line that has a slower growth rate or by using a treatment model where the tumor would be resected at 4 weeks post injection to allow for further development of organ metastases at later time points. Studies have reported monitoring animals from 5 weeks up to 12 weeks post tumor cell injection for evidence of metastases.^{16,18} By using a model that allows more long term tracking of metastasis formation, we can gain a better understanding of the effects of the immune system on the development of these metastases.

5.3 References

1. Canadian Cancer Society, Statistics Canada, Provincial/Territorial Cancer Registries & Public Health Agency of Canada *Canadian Cancer Statistics 2012*. (2012).
2. Jafferbhoy, S. & McWilliams, B. Clinical significance and management of sentinel node micrometastasis in invasive breast cancer. *Clinical Breast Cancer* **12**, 308–12 (2012).
3. Liu, T. *et al.* Tracking Tumor Cells in Lymphatics in a Mice Xenograft. *Mol Imaging* **11**, 451–460 (2012).
4. Magnitsky, S., Roesch, A., Herlyn, M. & Glickson, J. D. In vivo and ex vivo MR imaging of slowly cycling melanoma cells. *Magn Reson Med* **66**, 1362-1373 (2011).
5. Modo, M., Hoehn, M. & Bulte, J. W. M. Cellular MR Imaging. *Mol Imaging* **04**, 143–164 (2005).
6. Hsiao, J. K. *et al.* Comparison of micrometer and nanometer sized magnetic particles for cell labeling. *IEEE Transactions on Magnetics* **43**, 2421–2423 (2007).
7. Takizawa, H., Regoes, R. R., Boddupalli, C. S., Bonhoeffer, S. & Manz, M. G. Dynamic variation in cycling of hematopoietic stem cells in steady state and inflammation. *The Journal of Experimental Medicine* **208**, 273–84 (2011).
8. Moore, N., Houghton, J. & Lyle, S. Slow-cycling therapy-resistant cancer cells. *Stem Cells and Development* **21**, 1822–30 (2012).
9. Deleyrolle, L. P. *et al.* Evidence for label-retaining tumour-initiating cells in human glioblastoma. *Brain* **134**, 1331–43 (2011).
10. Fillmore, C. M. & Kuperwasser, C. Human breast cancer cell lines contain stem-like cells that self-renew, give rise to phenotypically diverse progeny and survive chemotherapy. *Breast Cancer Res* **10**, R25 (2008).

11. Rajasekhar, V. K. V. Analytical methods for cancer stem cells. *Methods in Molecular Biology* **407**, 83–95 (2007).
12. Cariati, M. *et al.* Alpha-6 integrin is necessary for the tumourigenicity of a stem cell-like subpopulation within the MCF7 breast cancer cell line. *Int J Cancer* **122**, 298–304 (2008).
13. Charafe-Jauffret, E., Ginestier, C. & Birnbaum, D. Breast cancer stem cells: tools and models to rely on. *BMC Cancer* **9**, 202 (2009).
14. Townson, J. L. *et al.* Three-dimensional imaging and quantification of both solitary cells and metastases in whole mouse liver by magnetic resonance imaging. *Cancer Res* **69**, 8326–31 (2009).
15. Gu, X.-L. *et al.* Expression of CXCL14 and its anticancer role in breast cancer. *Breast Cancer Res Treat* **135**, 725–35 (2012).
16. Xie, X. *et al.* Comparative studies between nude and scid mice on the growth and metastatic behavior of xenografted human tumors. *Clin Exp Metastasis* **10**, 201–210 (1992).
17. Kubota, T., Yamaguchi, H., Watanabe, M., Yamamoto, T. & T Growth of Human Tumor Xenografts in Nude Mice and Mice with Severe Combined Immunodeficiency (SCID). *Jpn J Surg* **23**, 375–377 (1993).
18. Price, J. E., Polyzos, A., Zhang, R. D. & Daniels, L. M. Tumorigenicity and Metastasis of Human Breast Carcinoma Cell Lines in Nude Mice. *Cancer Research* **50**, 717–721 (1990).

Appendices

Appendix A: Permission To Reproduce Published Material

19 June, 2013 11:54 AM

Re: Permission to Reproduce Published Material in Thesis

Dear Vasiliki,

Neoplasia Press, the publisher of *Translational Oncology*, is happy to give permission for the use of your article in preparation of your thesis. It is important that the article be cited correctly and that figures used from this paper also be cited correctly in the figure legend.

Edassist

On Wed, Jun 19, 2013 at 11:34 AM, Vasiliki Economopoulos [REDACTED]
To Whom it May Concern,

I'm currently in the process of writing my thesis and I have recently published a manuscript in your journal. Would it be possible to have permission to reproduce this manuscript within my thesis? I have attached the citation for the manuscript below.

Thank you,

Vasiliki Economopoulos
Ph.D. Candidate
Imaging Research Labs
Robarts Research Institute
[REDACTED]

(Economopoulos, V., et al. (2013). MRI Detection of Nonproliferative Tumor Cells in Lymph Node Metastases Using Iron Oxide Particles in a Mouse Model of Breast Cancer. *Translational Oncology*, 6(3), 347–354)

Appendix B: Animal Use Protocol Approval Letter



March 31, 2010

This is the Original Approval for this protocol
 A Full Protocol submission will be required in 2014

Dear Dr. Foster:

Your Animal Use Protocol form entitled:
 MRI of Cancer Cell Metastasis to the Mouse Lymph Nodes
 Funding Agency Ontario Cancer Research Institute - UWO ROLA # [REDACTED]; National Cancer Institute of Canada
 - UWO ROLA # [REDACTED]

has been approved by the University Council on Animal Care. This approval is valid from **March 31, 2010 to March 31, 2011**. The protocol number for this project is **2010-210 which replace 2006-013 which has expired.**

1. This number must be indicated when ordering animals for this project.
2. Animals for other projects may not be ordered under this number.
3. If no number appears please contact this office when grant approval is received.
 If the application for funding is not successful and you wish to proceed with the project, request that an internal scientific peer review be performed by the Animal Use Subcommittee office.
4. Purchases of animals other than through this system must be cleared through the ACVS office. Health certificates will be required.

ANIMALS APPROVED FOR 4 Years

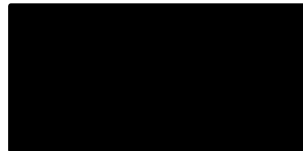
Species	4 Year Total Numbers Estimated as Required	List All Strain(s)	Age / Weight
Mouse	168	120 NuNu Foxn1(088) mice and 48 CB-17 SCID	18-22g

REQUIREMENTS/COMMENTS

Please ensure that individual(s) performing procedures on live animals, as described in this protocol, are familiar with the contents of this document.

The holder of this Animal Use Protocol is responsible to ensure that all associated safety components (biosafety, radiation safety, general laboratory safety) comply with institutional safety standards and have received all necessary approvals. Please consult directly with your institutional safety officers.

c.c. Approval - P. Foster, W. Lagerwerf



The University of Western Ontario
 Animal Use Subcommittee / University Council on Animal Care
 Health Sciences Centre, • London, Ontario • CANADA – N6A 5C1
 PH: [REDACTED] • FL [REDACTED] • www.uwo.ca / animal

Appendix C: Volumes of Individual Lymph Nodes Over Time From C57Bl/6, Nude and SCID mice

All volumes are in mm³ for all tables shown below.

Black 6

	Day 7	Axillary	Brachial	Inguinal	Popliteal
Left	m1	2.2178	2.1696	2.3296	0.398
	m2	2.504	2.4582	2.2203	0.5922
	m3	2.8377	2.4982	2.1123	0.7515
	m4	1.8571	2.4449	2.6699	0.5892
Right	m1	2.1432	3.1479	2.3742	0.5605
	m2	2.0794	3.3665	1.9985	0.8479
	m3	2.3092	3.0513	2.607	0.6024
	m4	1.629	2.6968	1.9624	0.5655
	Day 14	Axillary	Brachial	Inguinal	Popliteal
Left	m1	2.2024	2.674	1.6074	0.3561
	m2	2.6162	2.3107	1.9087	0.3933
	m3	2.0261	2.902	1.4923	0.6163
	m4	2.0099	2.934	2.4697	0.5436
Right	m1	1.6587	1.823	2.328	0.5735
	m2	2.11	4.5307	1.9664	0.6793
	m3	2.1451	2.995	2.0374	0.5758
	m4	1.5238	2.8896	1.8967	0.6226
	Day 28	Axillary	Brachial	Inguinal	Popliteal
Left	m1	2.5822	2.9707	2.1843	0.6163
	m2	2.4314	3.2678	2.3607	0.3762
	m3	1.8073	2.9884	1.7481	0.8179
	m4	1.8434	2.75	1.749	0.5288
Right	m1	1.6963	2.7449	2.3287	0.8182
	m2	2.0634	3.62	1.7651	0.5846
	m3	2.2002	3.5129	1.9439	0.434
	m4	1.7266	2.9513	1.0312	0.5553

Nude

	Day 7	Axillary	Brachial	Inguinal	Popliteal
Left	m1	5.0568	4.0007	2.2279	0.3213
	m2	6.2774	8.3018	2.1077	0.2269
	m3	7.8572	5.1213	3.7823	0.4679
	m4	2.5525	3.5292	2.2826	0.3198
Right	m1	3.7715	3.1851	2.3061	0.4893
	m2	1.0092	6.355	1.9095	0.2401
	m3	6.2044	7.2901	2.2046	0.5874
	m4	1.7595	6.7266	2.091	0.0068852

	Day 14	Axillary	Brachial	Inguinal	Popliteal
Left	m1	5.0319	4.873	3.1424	0.3851
	m2	6.162	5.3792	2.6008	0.6077
	m3	8.6318	8.7089	3.7039	0.5405
	m4	2.6233	3.473	3.6813	0.4544
Right	m1	7.2069	4.7863	2.3177	0.6355
	m2	5.8348	4.9423	2.5914	0.6664
	m3	8.4451	7.6162	3.0065	0.957
	m4	4.7712	4.95	3.8109	0.5157

	Day 28	Axillary	Brachial	Inguinal	Popliteal
Left	m1	4.4632	3.1495	2.6073	0.2808
	m2	8.1793	8.0795	2.6108	0.4631
	m3	12.5	9.866	5.6701	0.5078
	m4	6.6692	5.7047	3.1452	0.8192
Right	m1	6.0697	2.9627	1.8072	0.4352
	m2	6.1943	7.5757	2.3278	0.5148
	m3	5.9178	8.2959	4.0341	0.835
	m4	8.7017	6.7211	3.913	0.5685

SCID

	Day 7	Axillary	Brachial	Inguinal	Popliteal
Left	m1	0.4284	0.6212	0.4446	0.0832
	m2	0.7287	0.7642	0.5297	0.1375
	m3	0.3265	0.3527	0.4678	0.1308
	m4	0.3858	0.5158	0.2591	0.1008
Right	m1	0.5456	0.5379	0.4224	0.1525
	m2	0.7052	0.6278	0.7746	0.2973
	m3	0.4278	0.3905	0.3145	0.1494
	m4	0.4206	0.5116	0.4208	0.1024

	Day 14	Axillary	Brachial	Inguinal	Popliteal
Left	m1	0.4172	0.3635	0.3493	0.1168
	m2	0.5497	0.5674	0.392	0.1338
	m3	0.4759	0.2838	0.2665	0.1309
	m4	0.4877	0.2641	0.2213	0.0802
Right	m1	0.4235	0.4749	0.3471	0.1733
	m2	0.5185	0.65	0.6007	0.207
	m3	0.3121	0.356	0.1922	0.132
	m4	0.544	0.359	0.3247	0.1017

	Day 28	Axillary	Brachial	Inguinal	Popliteal
Left	m1	0.5314	0.5794	0.5784	0.1134
	m2	0.6994	0.4456	0.3348	0.0854
	m3	0.4543	0.2835	0.292	0.0865
	m4	0.5441	0.5005	0.1702	0.108
Right	m1	1.1452	0.4635	0.4826	0.1315
	m2	0.4262	0.5489	0.4422	0.1519
	m3	0.4779	0.3013	0.1447	0.0947
	m4	0.5308	0.4241	0.3553	0.1824

Curriculum Vitae

Name: Vasiliki Economopoulos

Post-secondary Education and Degrees: University of Western Ontario
London, Ontario, Canada
2003-2008 B.E.Sc.

The University of Western Ontario
London, Ontario, Canada
2008-2013 Ph.D.

Honours and Awards: Western Graduate Research Scholarship Award
2009 - 2013

Collaborative Program in Molecular Imaging Travel Award
September 2009

Collaborative Program in Molecular Imaging Entrance Award
October 2009

Collaborative Program in Molecular Imaging Travel Award
September 2011

World Molecular Imaging Congress Travel Stipend
September 2011

Canadian Breast Cancer Foundation – Ontario Region
Doctoral Fellowship
July 2011 – June 2013

Related Work Experience Summer Student, Imaging Research Labs,
Robarts Research Institute, University of Western Ontario
July – August 2008

Lab Assistant, Imaging Research Labs,
Robarts Research Institute, University of Western Ontario
May – August 2004

Publications:

Journal Articles:

MRI Detection of Nonproliferative Tumor Cells in Lymph Node Metastases Using Iron Oxide Particles in a Mouse Model of Breast Cancer. **Economopoulos V**, Chen Y, McFadden C, Foster PJ. (2013) Translational Oncology; 6(3): 347-354.

Polymer cross-linking: a nanogel approach to enhancing the relaxivity of MRI contrast agents. Soleimani A, Martínez F, **Economopoulos V**, Foster PJ, Scholl TJ, Gillies ER. (2013) Journal of Materials Chemistry B; 1(7): 1027-1034.

Comparing the MRI Appearance of the Lymph Nodes and Spleen in Wild-type and Immunodeficient Mouse Strains. **Economopoulos V**, Noad JC, Krishnamoorthy S, Rutt BK, Foster PJ. (2011) PLoS One; 6(11): e27508

Cellular magnetic resonance imaging of monocyte-derived dendritic cell migration from healthy donors and cancer patients as assessed in a scid mouse model. Zhang X, de Chickera SN, Willert C, **Economopoulos V**, Noad J, Rohani R, Wang AY, Levings MK, Scheid E, Foley R, Foster PJ, Dekaban GA. (2011) Cytotherapy; 13(10): 1234-1248.

Conference Proceedings:

Comparing Tumor Growth and Lymph Node Metastases in Xenograft Cancer Models Using MRI. **Economopoulos V**, Chen Y, Foster PJ. Accepted by 2013 *University of Western Ontario Oncology Research and Education Day* for poster presentation.

MRI Detection of Nonproliferative Tumor Cells in Lymph Node Metastases Using Iron Oxide Particles in a Mouse Model of Breast Cancer. **Economopoulos V**, Chen Y, McFadden C, Foster PJ. Accepted by 2011 *Canadian Cancer Research Conference* for **oral presentation**, also highest ranked abstract in category.

MRI Detection of Nonproliferative Tumor Cells in Lymph Node Metastases Using Iron Oxide Particles in a Mouse Model of Breast Cancer. **Economopoulos V**, Chen Y, McFadden C, Foster PJ. Accepted by 2012 *Imaging Network Ontario Symposium* for **oral presentation**.

MRI Detection of Nonproliferative Tumor Cells in Lymph Node Metastases Using Iron Oxide Particles in a Mouse Model of Breast Cancer. **Economopoulos V**, Chen Y, McFadden C, Foster PJ. Accepted by 2012 *Oncology Research and Education Day* for **oral presentation**.

MRI Detection of Nonproliferative Tumor Cells in Lymph Node Metastases Using Iron Oxide Particles in a Mouse Model of Breast Cancer. **Economopoulos V**, Chen Y, McFadden C, Foster PJ. Accepted by 2011 *World Molecular Imaging Congress* for **oral presentation**.

Non-Invasive Monitoring of Human Dendritic Cell Migration in the CB17 SCID Mouse by Cellular MRI. Dekaban GA, Zhang X, **Economopoulos V**, Noad J, Rohani R, Wang A, Levings M, Foley R, Foster PJ. Accepted by *2010 ISMRM* meeting for **oral presentation**.

Comparing the MR Appearance of Lymph Nodes in Various Strains of Mice Used for Cancer Research. **Economopoulos V**, Noad JC, Snir JA, Foster PJ. Accepted by *2010 Imaging Network Ontario Symposium* for poster presentation.

Comparing the MR Appearance of Lymph Nodes in Various Strains of Mice Used for Cancer Research. **Economopoulos V**, Noad JC, Snir JA, Foster PJ. Accepted by *University of Western Ontario Oncology Research and Education Day 2010* for poster presentation.

Comparing the MR Appearance of the Mouse Lymphatic System in Different Strains Used for Cancer Research. **Economopoulos V**, Noad JC, Snir JA, Foster PJ. Accepted by the *2009 World Molecular Imaging Congress* for **oral presentation**.

Book Chapters:

Barrett, J., Au, B., Buensuceso, R., de Chickera, S.N., **Economopoulos, V.**, Foster, P.J., Dekaban, G.A. Imaging immunotherapy in Experimental and Applied Immunotherapy, Eds. Fowler, D. and Medin, J., Springs Science/Human Press, 2010.